Theses and Dissertations   Graduate School

2011

Investigations on the Effect of Manufacturing on the Contact Resistance Behavior of Metallic Bipolar Plates for Polymer Electrolyte Membrane Fuel Cells

Cabir Turan
Virginia Commonwealth University

www.manaraa.com

Investigations on the Effect of Manufacturing on the Contact Resistance Behavior of Metallic Bipolar Plates for Polymer Electrolyte Membrane Fuel Cells

A dissertation submitted in partial fulfillment of the requirements for the degree of Doctor of Philosophy, at Virginia Commonwealth University.

by

Cabir Turan

Bachelor of Science in Mechanical Engineering, Istanbul University, Istanbul, TURKEY, 1996

Director: **Ramana M. Pidaparti,**

Professor, Department of Mechanical Engineering

Virginia Commonwealth University

Richmond, Virginia

December, 2011

Acknowledgements

Table of Contents

List of Tables

xi

List of Figures

xiii

xv

List of Abbreviations

AFC	Alkaline fuel cell
ANOVA	Analysis of variance
ASR	Area specific contact resistance
BEV	Electric vehicles
BPP	Bipolar plate
CFD	Computational fluid dynamics
CPF	Center for Precision Forming
CtF	Coated-then-formed
CVD	Chemical vapor deposition
DLC	Diamond-like carbon
DMFC	Direct methanol fuel cell
DOE	Department of Energy
ECE-EUDC	Urban driving cycle – Extra urban driving cycle (European)
FCEV	Fuel cell electric vehicles
FEA	Finite element analysis
FEM	Finite element model
FtC	Formed-then-coated
GDL	Gas diffusion layer
HEV	Hybrid electric vehicles
HF	Hydroforming;
ICE	Internal combustion engine

ICR	Interfacial electrical contact resistance
IEA	International energy agency
MAE	Membrane electrode assembly
MCFC	Molten carbonate fuel cell
NASA	National Aeronautics and Space Administration
NSF	National Science Foundation
PAFC	Phosphoric acid fuel cell
PD	Potentiodynamic
PEMFC	Polymer electrolyte (or proton exchange) membrane fuel cells
PS	Potentiostatic
PVD	Physical vapor deposition
SEM	Scanning electron microscopy
SOFC	Solid oxide fuel cell
SS	Stainless steel
St	Stamping
WTW	Well-to-wheel

Abstract:

INVESTIGATIONS ON THE EFFECT OF MANUFACTURING ON THE CONTACT
RESISTANCE BEHAVIOR OF METALLIC BIPOLAR PLATES FOR POLYMER
ELECTROLYTE MEMBRANE FUEL CELLS

By **Cabir Turan**, Ph.D.

A dissertation submitted in partial fulfillment of the requirements for the degree of Doctor of
Philosophy, at Virginia Commonwealth University.

Virginia Commonwealth University, 2011

Major Director: **Ramana M. Pidaparti,** Professor, Department of Mechanical Engineering

Polymer electrolyte membrane fuel cells (PEMFCs) have emerged as a strong and promising candidate to replace internal combustion engines (ICE) due their high efficiency, high power density and near-zero hazardous emissions. However, their commercialization waits for solutions to bring about significant cost-reductions and significant durability for given power densities. Bipolar plate (BPP) with its multi-faceted functions is one of the essential components of the PEMFC stacks. Stainless steel alloys are considered promising materials of choice for bipolar plate (BPP) applications in polymer electrolyte membrane fuel cells (PEMFC) due to their relatively low cost and commercial availability in thin sheets.

Stainless steel materials build a protective passive metal oxide layer on their surface against corrosion attack. This passive layer does not demonstrate good electrical conductivity and increases interfacial electric contact resistance (ICR) between BPP and gas diffusion layer GDL in PEMFC. Lower ICR values are desired to reduce parasitic power losses and increase current density in order to improve efficiency and power density of PEMFC.

This study aimed to bring about a broader understanding of manufacturing effects on the BPP contact resistance. In first stage, BPP samples manufactured with stamping and

hydroforming under different process conditions were tested for their electrical contact resistance characteristics to reveal the effect of manufacturing type and conditions. As a general conclusion, stamped BPPs showed higher contact conductivity than the hydroformed BPPs. Moreover, pressure in hydroforming and geometry had significant effects on the contact resistance behavior of BPPs. Short term corrosion exposure was found to decrease the contact resistance of bipolar plates. Results also indicated that contact resistance values of uncoated stainless steel BPPs are significantly higher than the respective target set by U.S. Department of Energy. Proper coating or surface treatments were found to be necessary to satisfy the requirements.

In the second stage, physical vapor deposition technique was used to coat bipolar plates with CrN, TiN and ZrN coatings at 0.1, 0.5 and 1 μm coating thicknesses. Effects of different coatings and coating thickness parameters were studied as manufactured BPPs. Interfacial contact resistance tests indicated that CrN coating increased the contact resistance of the samples. 1 µm TiN coated samples showed the best performance in terms of low ICR; however, ICR increased dramatically after short term exposure to corrosion under PEMFC working conditions. ZrN coating also improved conductivity of the SS316L BPP samples. It was found that the effect of coating material and coating thickness was significant whereas the manufacturing method and BPP channel size slightly affected the ICR of the metallic BPP samples.

Finally, effect of process sequence on coated BPPs was investigated. In terms of ICR, BPP samples which were coated prior to forming exhibited similar or even better performance than coated after forming samples. Thus, continuous coating of unformed stripes, then, applying forming process seemed to be favorable and worth further investigation in the quest of making cost effective BPPs for mass production of PEMFC.

xxi

CHAPTER 1: Introduction

1.1. Research Motivation and Background

In a quest for sustainable mobility, improved fuel efficiency and significantly reduced tail-pipe emissions impose the replacement of conventional energy conversion systems with environmentally-friendly renewable and green energy technologies along with light weighting solutions in transportation vehicles. Fuel cell technology has been pursued as one of the promising avenues to realize the clean and high efficiency energy conversion system for transportation vehicles. Polymer Electrolyte Membrane Fuel Cells (PEMFC), in particular, have emerged as a strong and promising candidate to replace internal combustion engines due their advantageous features such as: minimal noise during operations, relatively compact size, high power density, quick start up capability, low temperature operation, and most importantly near-zero hazardous emissions. In spite of these benefits, high cost and low durability of PEMFC stacks postpone their widespread commercialization [1].

Bipolar plate (BPP) with its multi-faceted functions is one of the essential components of the PEMFC stacks. These functions include carrying fuel and air to the respective electrodes, removing excess produced water away from the membrane, conducting electric current between the cells, making complete separation of air and fuel, providing mechanical support and strength for the rest of the stack, handling transmission of sealing stress and helping to moderate the stack temperature [2-4]. In order to perform such vital functions properly and simultaneously, BBPs need to have high electrical and thermal conductivity, low gas permeability, good mechanical strength, very high corrosion resistance, and suitable surface properties to enable good contact,

1

sealing and water removal. For transportation applications, additional features such as low volume, low weight and certain degree of flexibility are needed. Currently, among all other components of PEMFC stack, BPPs stand as high-weight, high-volume and high-cost components [5,6].

Early BPPs were fabricated from machined graphite because of its corrosion resistance and satisfactory electrical conductivity in fuel cell operating environment. However, its high material and manufacturing costs curtail competitiveness of the PEM fuel cells. Hence, alternative BPP materials such as carbon-carbon and carbon-polymer composites were developed. Their main disadvantages can be listed as relatively low electrical and thermal conductivity, limited operating temperature range and still moderately high material and manufacturing costs. Metallic BPPs, particularly different grades of stainless steels, have been increasingly considered and investigated because of their relatively low cost, relatively good corrosion resistance, sufficient stiffness and excellent flexibility in thin forms, and easy manufacturability [2,3,7].

The major concerns with the use of stainless steel alloys as BPPs are their lower corrosion resistance and high interfacial electrical resistance in challenging fuel cell environment under long operation [2,3,8-14,14-24]. Stainless steel materials build a passive metal oxide layer on their surface, and this layer is beneficial to slow further corrosion attack to material. This passive layer is typically has a semi-conductor characteristic, and does not demonstrate the good electrical conductivity levels needed by bipolar plate [22]. Contact resistance, as closely correlated with corrosion, plays an important role in fuel cell performance. When the bipolar plate surface is passivated by corrosion, ohmic losses and current resistance generally increase in long run. Metal ion dissolution by corrosion also can degrade the performance of PEMFC

2

through membrane electrode assembly (MEA) contamination [9,12,25-28]. In a regular PEMFC, multiple fuel cells are stacked together to provide sufficient power and voltage via bipolar plates which electrically connect adjacent cells. This arrangement multiplies the ohmic power losses resulting from contact resistance between each gas diffusion layer (GDL) and BPP. Thus, contact resistance characteristics of BPP have significant effect on the overall PEMFC stack efficiency. Therefore, the desired performance level of the PEMFC significantly depends on low contact resistance between BPP and GDL. In a way, contact resistance in fuel cells is like the friction in the internal combustion engines (ICEs) wasting the generated energy and leading to low efficiencies. US Department of Energy (DOE) set the contact resistance goal for PEMFC applications as lower than $10m\Omega\text{-}cm^2$ at 140 N/cm^2 compaction pressure for year 2015 [29]. Researchers all over the world have been conducting investigations to overcome contact resistance issues by understanding the underlying mechanisms and bringing alternative solutions to the interactive effects of surface conditions, coatings, substrate materials, manufacturing and assembly on the electrical contact resistance and its consequences on the overall fuel cell performance and durability [2-7,22,27,30].

From these earlier investigations, it is clearly understood that there is a direct interaction between bipolar plate surface condition and the interfacial contact resistance (ICR). In addition, the manufacturing of BPPs is considered to be an important factor as it dictates the surface conditions of BPPs. Manufacturing process imposes the contact geometry which is effective on contact pressure, contact area and contact uniformity.

Several production methods such as machining, stamping, die casting, investment casting, powder metal forging, electroforming, stretch forming, and hydroforming were proposed and investigated for fabrication of the metallic bipolar plates. Among these, stamping and

3

hydroforming are believed to be the most suitable approaches for mass production of BPPs [3,8,31]. The outstanding advantages of the stamping method are its faster production rate and cost competitiveness, while hydroforming offers good and consistent surface topology, uniform thickness distribution and tight dimensional tolerances [32]. This study was focused on these two manufacturing methods: stamping and hydroforming.

1.2. Research Objectives

There are numerous publications discussing the corrosion and contact mechanics of various BPP materials [3,21-23,33-35]; however, as far as the reviewed literature is considered so far, there is no study dedicated to the effect of manufacturing processes on the electrical contact resistance of metallic bipolar plates. Thus, this study aimed to bring about a broader understanding of manufacturing effects (process, material, coating type, coating thickness, coating and manufacturing process sequence) on the BPP contact resistance. This understanding is expected to help having a complete picture of the performance of the stainless steel bipolar plates manufactured through stamping and hydroforming.

Specific objectives of this project can be summarized as follows:

Understanding the effect of material, manufacturing process (stamping and hydroforming) and process parameters (die geometry, stamping force and punch speed in stamping; and pressure, and pressure rate in hydroforming) on the contact resistance of metallic BPPs.

Understanding the effect of coating and its interactions with manufacturing conditions on the contact resistance behavior of metallic BPPs.

Understanding the effect of process sequence on contact resistance of coated metallic BPPs.

4

1.3.Dissertation Organization

This dissertation is organized in accordance with research objectives given above. Each objective was studied in a separate chapter through the dissertation. Hence, dissertation organization is in following form:

Chapter 1: Introduction.

Chapter 2: Literature review and background.

Chapter 3: Effect of manufacturing process on contact resistance of uncoated metallic BPPs.

Chapter 4: Effect of material and manufacturing process on contact resistance of coated metallic BPPs.

Chapter 5: Effect of process sequence on contact resistance of coated metallic BPPs.

Chapter 6: Summary and conclusions.

CHAPTER 2: Literature Review and Background

2.1.Energy

2.1.1. Energy Revolution

Recent history of human civilization can be characterized by technological revolutions. Invention of the steam engine started the industrial revolution, and exploitation of steam engine allowed utilization of coal and revolutionized the manufacturing with a great effect on economy and social systems. The electricity revolution made energy accessible to large populations. It made possible the development of many electrical devices and gadgets which made profound changes in our daily life today. Industrialization enabled mass manufacturing of cars and initiated automobile revolution. Automobiles changed the way of living and city layout in modern times. Fast and inexpensive mass transportation means led to increased mobility and interactions between countries, continents and cultures. Similarly, invention of computers triggered the information revolution. Although computers were originally developed for computing purposes only at the beginning, they became essential parts of our life in today's world.

Each revolution above started with a technological invention that it impacted our lives, thinking and perceptions substantially. Then, it enabled development of new ideas, products and services. Many scientists consider that the fuel cell is one of such powerful technologies that could start the energy revolution. They expect that fuel cell will change global energy systems in many aspects including greater utilization of renewable sources, promoting rational use of

6

energy, decentralizing power generation, allowing power generation it various scales, stopping or harming the environment [36]. It may eventually reduce the dependence of countries on each other, and may lead to changes in their interactions. This, in turn, may change how individuals think, live and interact.

2.1.2. History of Energy

The main fuels were wood and other traditional forms of energy in pre-industrial ages. Discovery of abundant coal and its utilization stimulated industrial revolution, and coal was the main fuel type for more than a century. After World War I, oil exploration and its use increased. Expanding industry and increasing prosperity soared use of oil after World War II. Natural gas was brought to the industrial use and to national economies as an alternative fuel and has recently surpassed the coal and oil in consumption.

An important proportion of coal and gas production is used to generate electricity that is a premium form of energy due to its flexibility and ease of distribution. Global electricity demand, on the other hand, is incessantly growing, driven by widening of consumer electronics, increasing industrial and consumer activity especially in the developing countries.

2.1.3. World Energy Consumption

Present global energy consumption is mainly depended on utilization of fossil fuels. According to International Energy Agency (IEA) Key World Statistics 2010, coal, oil, and gas contribute more than 80% of total primary energy of the World as shown in Figure 2-1 [37]. Nevertheless, there are several problems with large scale fossil fuel utilization: (1) fossil fuels would be depleted in a foreseeable future, and (2) fossil fuels, their by-products and activities to

7

extract them results in harmful environmental impacts, (3) unevenly distribution of the fossil fuel

reserves emerges as a crucial energy security concern [36,38,39].
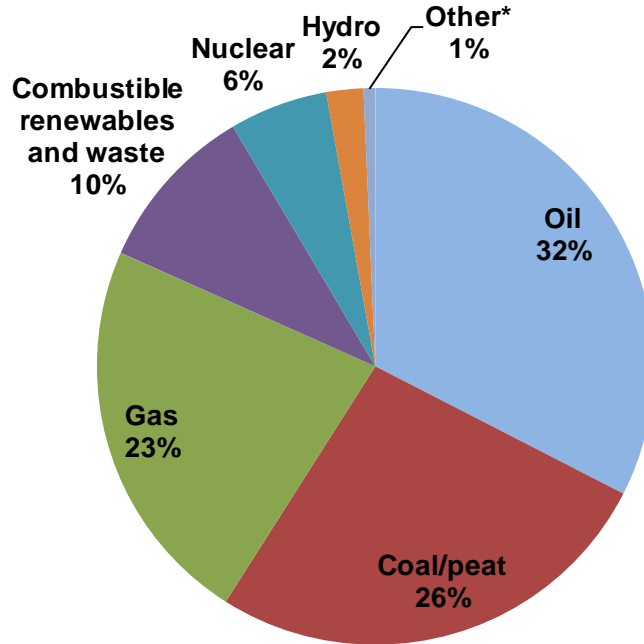
*Figure 2-1 World total primary energy supply shares by fuel for the year 2008. (*Other includes geothermal, solar, wind, heat, etc.)(Data is taken from* [37]*).*

2.1.4. Finite Resources

Although it is difficult to determine precise reserves for fossil fuels, it is assessed that

current oil reserves can meet the present demand for next 30 years. Natural gas reserves, on the

other hand, are expected to provide the current demands as long as 60 years. Also it is

considered that natural gas is far less explored than oil so there is probably more to be found. In

addition, there are unconventional hydrocarbon sources such as heavy oil and bitumen, oil shale,

shale gas and coal bed methane, whose global reserves have been assessed roughly to be three

times the size of conventional oil and gas resources. These are more expensive to extract but

8

might be feasible when the price of conventional fossil fuels increases by depletion. Coal is more abundant than oil and gas and it is expected to lasts for hundreds of years. From nuclear energy perspective, fuel for nuclear fission is not unlimited. The life time of uranium reserves for conventional fission, at current usage, have been estimated about 50 years.

A heated international debate is currently focused on oil peak level since it signals that the demand will most likely not be fully met, with significantly rising prices. Peak oil level can be defined that when the oil and gas extraction rate starts to fall and occurs well before resources run out. Low quality hydrocarbon resources would be preferred with increasing oil prices and this may elevate air pollution and carbon dioxide emission. Although there is no precise agreement on estimation of global peak oil, many scientists believe that it is not far and its consequences will be significant [40-42].

2.1.5. Energy Security

Energy security is defined as the" *interrupted physical availability of energy products on the market at a price which is affordable for all consumers (private and industrial)*" by European Commission in its Green Paper [43]. Energy security is a major concern about energy use. The uneven distribution of the energy sources among the countries increases vulnerability of the energy supply. Main threats to energy security are politic instability, manipulation of energy supply, the competition over energy sources, attacks on supply infrastructure, accidents and natural disasters.

Use of renewable technologies increases the diversity of electricity sources. Local generation contributes flexibility of the system and helps the system to avoid central shocks.

9

Fuel cell technologies helps utilization of the renewable energy sources, thus, may contribute to alleviate of energy security issues.

2.1.6. Environmental Impact of the Energy Use

Use of fossil fuel and producing of electricity have significant negative impact on environment. Combustion of fuels produces carbon dioxide and some harmful emissions such as nitrogen oxides and sulfur oxides. Many researchers suggest that there is a strong correlation between atmospheric carbon dioxide level and global temperature. Global warming is considered as one of the most serious problems for the planet. In addition, nitrogen sulfur oxides are the main contributors to the air pollution and acid rains. Also, extraction of the fossil fuels immensely damages the environment. Radioactive disposal, radioactive emissions and final decommissioning are some environmental concerns with nuclear power generation. Furthermore, environmental damage from uranium mining is another issue related with nuclear cycle. Global reserves of fossil fuels and mineral ores are not infinite and exploitation of coal, oil, gas and uranium are not sustainable in long term. Fortunately, renewable energy almost inexhaustible and has not long term significant harmful effect on environment [36,44,45].

2.1.7. Renewable Energy

Renewable energy seems to be a remedy for the problems of present energy system. Although renewable resources are sufficient to provide current and future energy demand in theory, there are some challenges to be solved before their widespread utilization. One of the most important difficulties with some of the renewable energy sources such as wind and solar

10

power is their intermittent character so that new energy storage methods and energy carriers are required to overcome this difficulty. Hydrogen has been suggested as an energy carrier and energy storage option for future [39,46].

2.1.8. Hydrogen and Fuel Cells

Hydrogen is considered as one of the promising candidate of some current energy problems. Hydrogen is a nontoxic fuel and its combustion products do not create any pollution or greenhouse gases. Its electrochemical conversion in fuel cells is a very efficient way of using hydrogen to provide useful energy, so hydrogen does not have to be combusted.

Hydrogen can be produced from several energy sources, including fossil fuels, nuclear energy, and renewable energy. Use of hydrogen is possible as fuel in almost any application where fossil fuels are used today—particularly in transportation, where it would offer immediate benefits in terms of reduced pollution and cleaner environment. Fuel cells have vital function in hydrogen economy especially in mobile applications. Figure 2-2 illustrates the role of hydrogen and fuel cells in whole energy system. Fuel cell is a shortcut between chemical energy to electrical energy by skipping combustion and mechanical conversion.

11
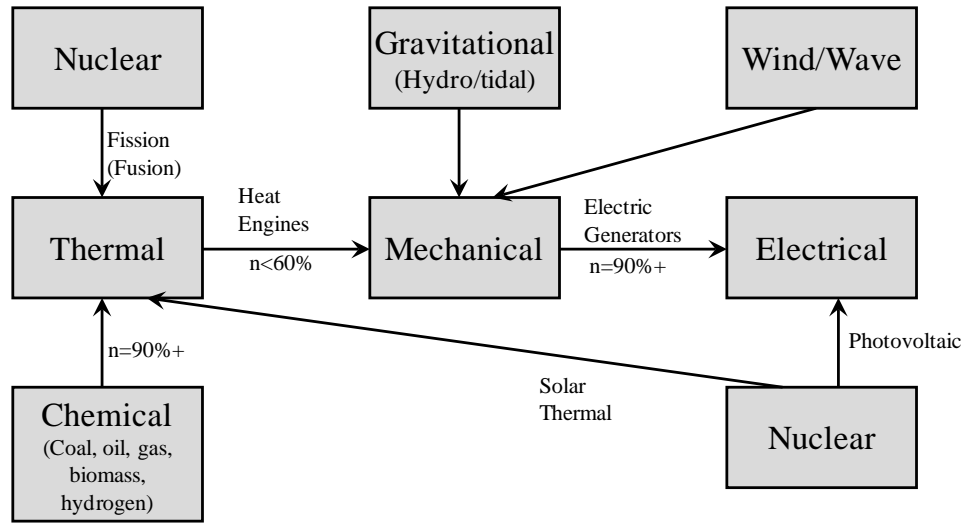
Figure 2-2 Conversion from a variety of energy forms into electricity (adapted from [36]*).*

2.2.Fuel Cell

A fuel cell is an electrochemical device that converts chemical energy into electrical energy directly. Different from a battery, it can produce electrical energy as long as fuel supplied, and without need for recharging. Typical reactants of fuel cells are hydrogen and oxygen, while it is possible to use of alcohols, hydrocarbons and their derivatives in respective fuel cell types as fuels. Pure oxygen or oxygen in air mixture can be used as oxidant.   When hydrogen and oxygen are used as reactants, only water and heat will be by-products [46,47].

2.2.1. History of Fuel Cell

It is widely known that Sir William Grove [48] discovered and explained operating principle of the first fuel cell in 1839 although a Swiss scientist Christian F. Schönbein [49] independently discovered very same effect at about same time.   Any practical applications were not developed for near a century after the first attempts. Francis T. Bacon made 6 kW fuel cell by the end of

12

the 1950s. The first practical applications of the fuel cells were used in U. S. space programs. General Electric developed the first PEMFC for NASA in the 1960s. Fuel cells successfully used almost only for NASA space programs until 1990s. At that time fuel research started to get more attention for many applications, and variety of successful fuel cell applications have been demonstrated. Today, fuel cells are among the important research subjects at many universities, institutes and companies all over the world [46].

2.2.2. Operating principle of fuel cells

In general, a fuel cell consists of two electrodes and an electrolyte between them (Figure 2-3). Hydrogen is fed in the anode side and oxygen fed in the cathode side. Hydrogen splits into its electron and proton (ion). Positively charged hydrogen ions pass through electrolyte from anode side to cathode side when negatively charged electrons go from anode side to cathode side via external circuit. This external electron circulation creates the useful electrical power of the fuel cell.
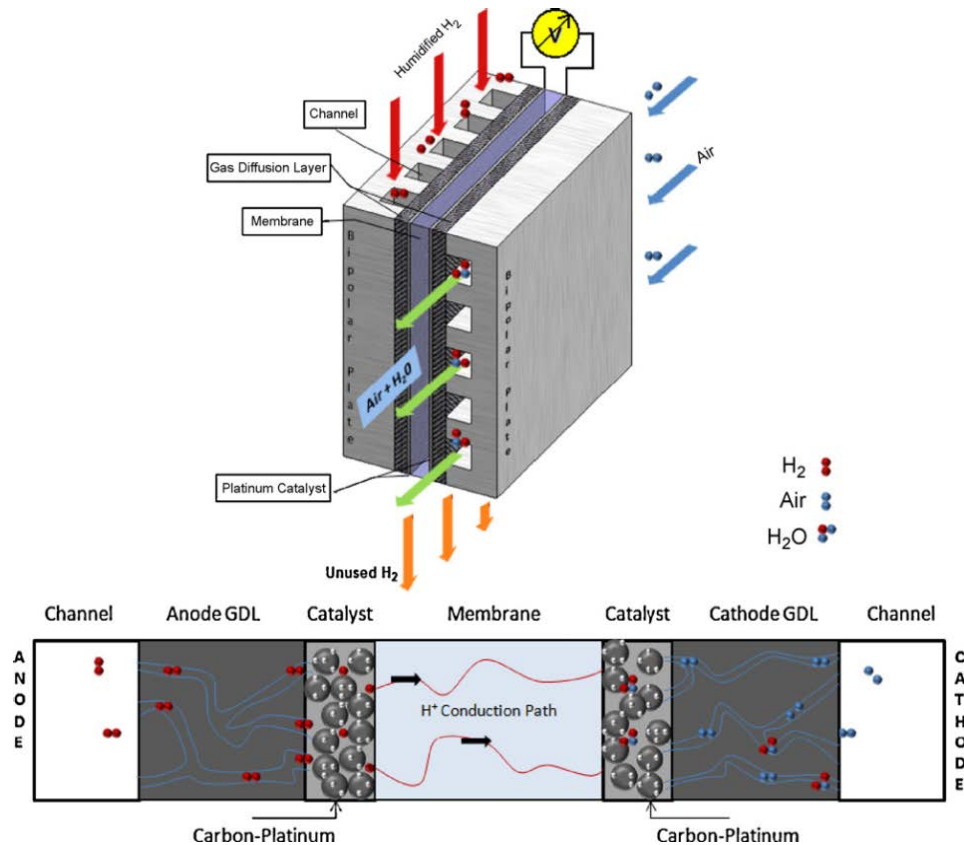
Figure 2-3 Basic schematic of a typical single fuel cell [50].

2.2.3. Advantages of the Fuel Cells

The main advantages of the fuel cells can be summarized as follows:

Efficiency: Fuel cells are more efficient than internal combustion engines. Fuel cells are not heat machines, so Carnot's efficiency does not limit efficiency of the fuel cells. This advantage makes fuel cells promising alternatives for automobile application. Also, fuel cells are more efficient steam and gas turbines, and therefore fuel cells may be used for distributed power generation.

14

Low or zero emission: Because hydrogen fuel cells generate only water, heat and unused air as by-products, they may conveniently be used indoor applications and submarines. However, hydrogen is not a readily available fuel; process of hydrogen production of fuel processing should be considered for comparison to conventional technologies. In this case emissions are lower than conventional energy conversion technologies.

Simplicity and modularity: Their simplicity makes fuel cell promising for both low cost and long life applications. Since they are made in layers of repetitive components, they have the potential to be mass produced at a low cost. Besides, fuel cells do not have any moving parts so that they have a potential for long life. Current fuel cell applications may reach automotive demand in life span (3000-5000 hours) but they must reach 40,000-80,000 hours durability to be cost competitive with current power generation technologies.

2.2.4. Types of the Fuel Cells

Type of the electrolyte used in a fuel cell determines the type of the fuel cell. Positively or negatively charged ion specie depends on type of fuel cell type and this determines the site of water production and removal. Most common types of fuel cells are summarized in Table 2.1. Although each type of fuel cells has its own advantages and disadvantages, polymer electrolyte membrane (also known as "proton exchange membrane") fuel cells (PEMFC) take most attention because of its potential compatibility for automobile application.

15

Table 2-1 Comparison of Fuel Cell Technologies [51] .

Fuel cell	Temperature (°C)	Efficiency (%)	Application	Advantages	Disadvantages
Alkaline fuel cell (AFC)	50–90	50–70	Space application	High efficiency	Intolerant to CO_2 in impure H_2 and air, corrosion, expensive
Phosphoric acid fuel cell (PAFC)	175–220	40–45	Stand-alone & combined heat & power	Tolerant to impure H_2, commercial	Low power density, corrosion & sulfur poisoning
Molten carbonate fuel cell (MCFC)	600–650	50–60	Central, stand-alone & combined heat & power	High efficiency, near commercial	Electrolyte instability, corrosion & sulfur poisoning
Solid oxide fuel cell (SOFC)	800–1000	50–60	Central, stand-alone & combined heat & power	High efficiency & direct fossil fuel	High temperature, thermal stress failure, coking & sulfur poisoning
Polymer electrolyte membrane fuel cell (PEMFC)	60–100	40–50	Vehicle & portable	High power density, low temperature	Intolerant to CO in impure H_2 and expensive
Direct methanol fuel cell (DMFC)	50–120	25–40	Vehicle & small portable	No reforming, high power density & low temperature	Low efficiency, methanol crossover & poisonous byproduct

16

2.3.PEMFC

Among various fuel cell types, PEMFC are preferential in wide range of application. Their advantageous features such as: minimal noise during operations, relatively compact size, high power density, quick start up capability, low temperature operation, and most importantly near-zero hazardous emissions make them a prominent candidate to replace internal combustion engines in automobiles. Besides, PEMFC is a prominent concept as mobile device power supply due to similar requirements from these type devices. A typical single PEMFC mainly consists of a membrane-electrode assembly (MAE), two current collectors with flow channels and seals. However, cells are stacked together via bipolar plates to obtain sufficient level of voltage (Figure 2-4).
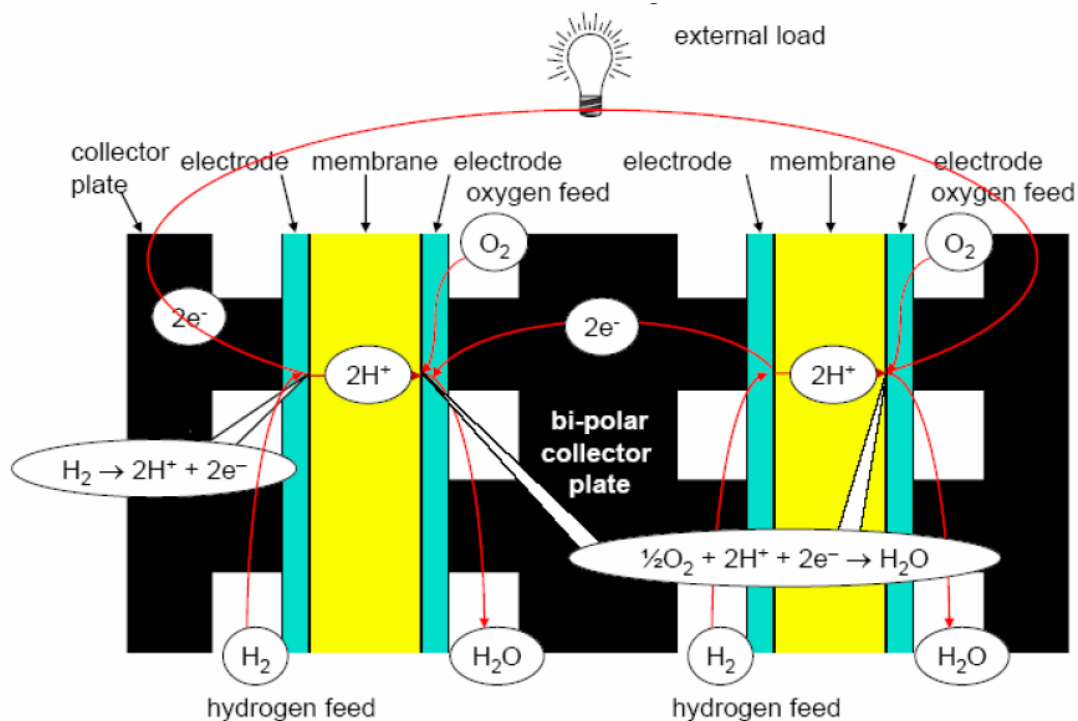
Figure 2-4 A bipolar plate between two cells [46].

2.3.1. Applications of PEMFC

Wang et al. recently reviewed technology, applications and fundamental research needs for PEMFC.   Applications of PEMFC are mainly categorized as transportation, stationary and portable power generation.   The most important application of PEM fuel cells focuses on transportation primarily because of their potential impact on the environment. Transportation is one of the sectors the most energy-burning processes. The current widespread technology is based on reciprocating internal combustion engines (ICE) which primarily depend on hydrocarbon fuels. Several concerns such as air pollution, climate change and fuel sustainability are closely associated with this wide spread and fast-growing dependence of fossil fuels. Number of solutions based on electric drives proposed by car manufacturers. Some of them are prototypes for medium and long term experimentation while the others are in market already. These proposed solutions can be categorized into three general groups: pure battery electric vehicles (BEV), fuel cell electric vehicles (FCEV) and hybrid electric vehicles (HEV). Most major automobile manufacturers work on PEM fuel cells due to their high power density and excellent dynamic characteristics as compared with other types of fuel cells. Various companies have developed and demonstrated their own fuel-cell vehicles (FCV), such as GM Hydrogen 1, Ford Demo IIa (Focus), DaimlerChrysler NeCar4a, Honda FCX-V3, Toyota FCHV, Nissan XTERRA FCV, VW Bora HyMotion, and Hyundai Santa Fe FCV [52]. Comprehensive and up-to-date list may be found at [53].

Campanari et al. investigated energy and environmental balances for BEV or FCEV, by using well to wheel (WTW) analysis method, based on ECE-EUDC driving cycle simulations [54].   They assumed use of Li-ion batteries in BEV and PEMFC in FCEV also considered

18

different scenarios for primary energy feedstock (renewable energy, coal, natural gas) and for the energy conversion chain, which in case of FCEV may rely on gaseous or liquid hydrogen generated in central power station and later stored onboard, or make use of onboard fuel processors fed with gasoline, natural gas or liquid biofuels (Figure 2-5 and Figure 2-6). Their calculation is a function of the required vehicle driving range, which affects the vehicle weight through the onboard energy storage capacity and powertrain size. Also, they took into account maximum speed requirements and possible aggressive driving cycles. They found significantly different results from those of a simpler nominal load WTW calculation [54]. Authors pointed out conclusions as follows:

- The BEV was the most efficient option when using 100% renewable energy sources to generate electricity. For this this case, zero emissions was also resulted.

- When the electricity was generated from an average primary source mix, 100% coal or natural gas, the performance of the BEV much lower, and FCEV options become much more favorable both by the point of view of efficiency and CO_2 emissions. Increasing driving range made this difference more significant.

- Use of liquid H_2 generated through the natural gas pathway or by renewable sources was found the most efficient and low CO2 emissions solution among FCEV options.

They concluded that pure BEV vehicles should hardly compete with FCEV in presence of medium to long driving range requirements. Authors also emphasized intermediate solutions by combining the strength of both technologies such as plug-in FCEV hybrids with relevant battery storage, although increasing complexity to the system.

19
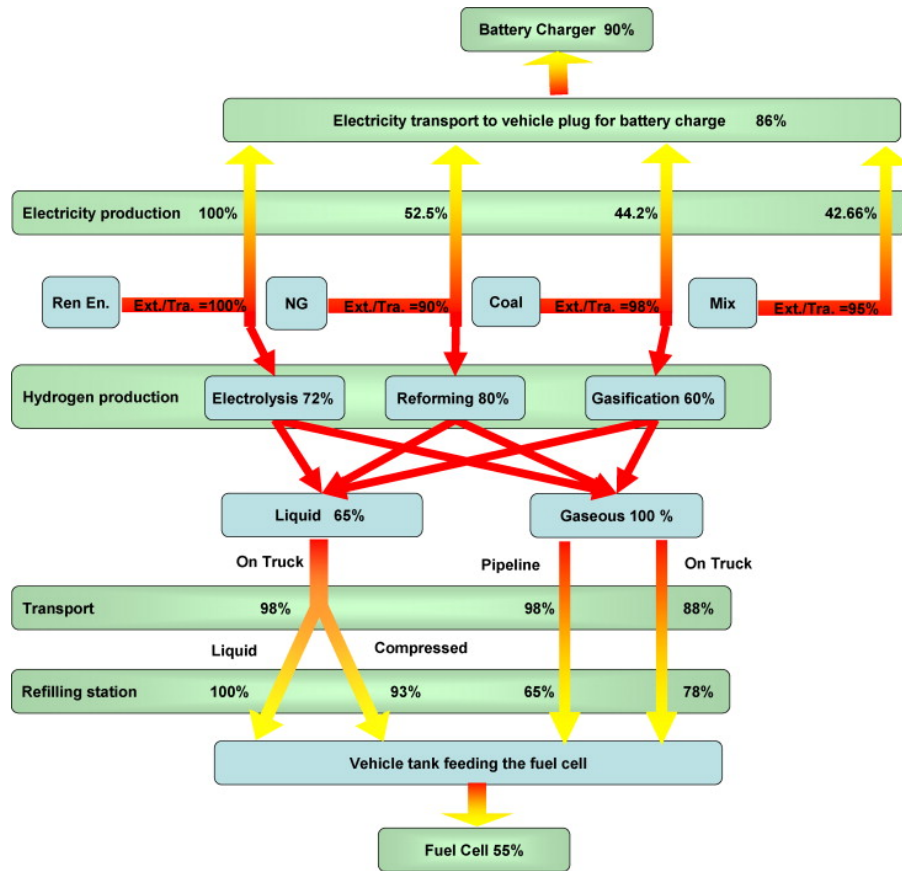
Figure 2-5   Conversion chain from primary sources to the vehicle (well-to-tank pathways) and related efficiencies [54].
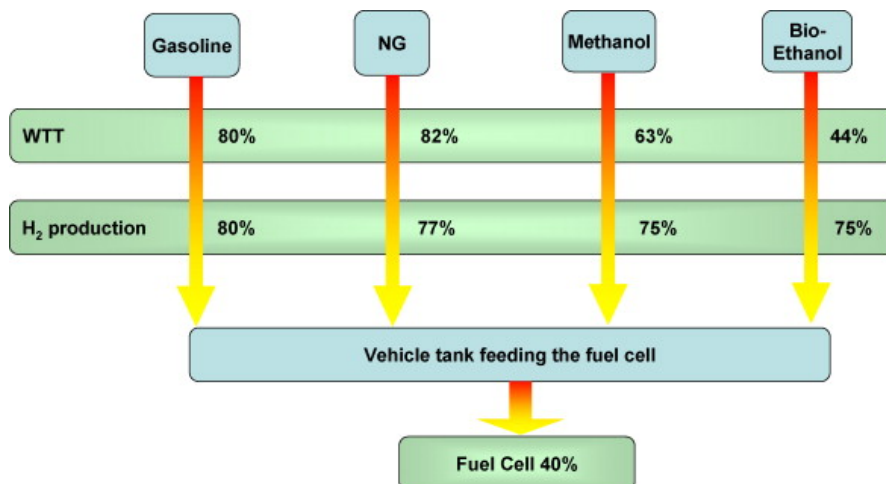
Figure 2-6   Conversion chain for different fuels used for vehicles with onboard hydrogen generation [54].

20
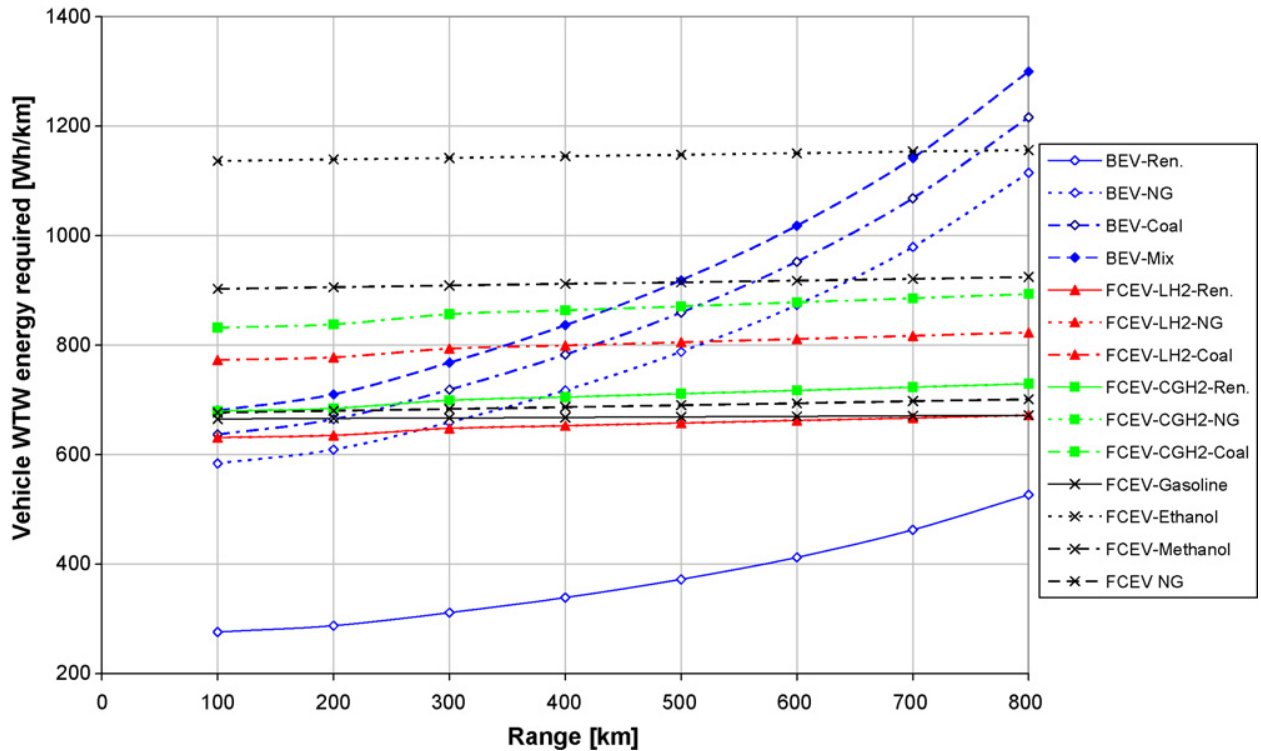
Figure 2-7 Total energy required for various well to wheel pathways applied to ECE-EUDC cycle as a function of the driving range [54].

Fuel cell buses take attention of governments to improve urban air quality. Beside number of local programs, the US and European Union announced their government-funded procurement plans, National Fuel Cell Bus Program and Fuel Cell and Hydrogen Technology Initiative respectively [52]. China has also developed a fuel cell bus program and demonstrated their fleet by serving during 2008 Olympic Games [55].

PEMFC systems has been applied electric powered bicycles, material handling vehicles, and auxiliary power units including leisure, trucking, marine and unmanned aerial vehicles. A fuel cell based air independent propulsion system has developed and applied to submarines by Siemens.

21

Fuel cell applications in utility and material handling vehicles are especially attractive because the power requirement is smaller, so the fuel cell can be manufactured more cheaply. Another advantages of these vehicles for fuel cell technology is that they refuel at a central fueling station, eliminating the need for a set hydrogen infrastructure right away. Fuel cell forklifts are considered that they may help to establish a proving ground for hydrogen fueling technology that will promote the future adoption of fuel cells in other applications, such as cars, and help drive the use of fuel cell technology. Research and development of material handling applications would help commercialize the larger markets such as automobiles by providing real time data that can be used to improve the technology and manufacturing capability. It also may help build the supply chain to develop, manufacture, distribute, and service the fuel cells and associated components at a quicker pace [56]. Gaines et al. reported advantages of fuel cell compared to battery system in forklifts as less greenhouse gas emissions, longer run time, short refueling time and eliminating battery storage and changing space [57].

2.4. Bipolar Plates

Bipolar plates (BPPs) (also known as "flow fields" and "separators") with their multi-faceted functions are one of the essential components of the PEMFC stacks. These functions include carrying fuel and air to the respective electrodes, removing excess produced water away from the membrane, conducting electric current between the cells, making complete separation of air and fuel, providing mechanical support and strength for the rest of the stack, handling transmission of sealing stress and helping to moderate the stack temperature [2-4]. In order to perform such vital functions properly and simultaneously, BBPs need to have high electrical and thermal conductivity, low gas permeability, good mechanical strength, very high corrosion resistance, and suitable surface properties to enable good contact, sealing and water removal.

22

For transportation applications, additional features such as low volume, low weight and certain degree of flexibility are needed. Currently, among all other components of PEMFC stack, BPPs stand as high-weight, high-volume and high-cost components. Tsuchiya et al. estimated that BPPs constitute 60-80% of the stack weight and 30-40% of PEMFC stack cost [5]. In a recent study, Sinha et al. predicted that BPPs represent 13-28 % of total stack cost [6].

2.4.1. Material and Manufacturing options of BPPs

Variety of materials has been proposed, however; no material meets all of the requirements concurrently so far [32,58-63]. Early BPPs were fabricated from machined graphite because its corrosion resistance in fuel cell operating environment and satisfactory electrical conductivity. However, their high material and manufacturing costs curtail competitiveness of the PEM fuel cells. Hence, alternative BPP materials such as carbon-carbon and carbon-polymer composites were developed. Their main disadvantages can be listed as relatively low electrical and thermal conductivity, limited operating temperature range and still moderately high material and manufacturing costs.

Because of good electrical conductivity, low material cost, well-established manufacturing processes and superior mechanical properties, metallic BPPs have been considered as promising materials. Various grades of stainless steels put forward as BPP material candidates due to their higher formability and corrosion resistance than that of other metallic candidates. However, corrosive environment of harsh PEMFC working conditions and high interfacial contact resistance (ICR) are the main concerns about SS BPPs [2,3,7-14,14-24].

23

2.4.2. Problems with Metallic BPPs

The major concerns with the use of stainless steel alloys as BPPs are their lower corrosion resistance than the desired values and high interfacial electrical resistance in challenging fuel cell environment under long operation conditions [2,3,8-14,14-24]. Stainless steel materials build a passive metal oxide layer on their surface, and this layer is beneficial to slow further corrosion attack to material. This passive layer is typically has a semi-conductor characteristic, and does not demonstrate the good electrical conductivity levels that a bipolar plate has to [22]. Contact resistance, as closely correlated with corrosion, plays an important role in fuel cell performance. When the bipolar plate surface is passivated by corrosion, ohmic loses and current resistance generally increase in long run. Metal ion dissolution by corrosion also can degrade performance of PEMFC via membrane electrode assembly (MEA) contamination [9,12,25-28]. In a regular PEMFC, multiple fuel cells are stacked together to provide sufficient power and voltage via bipolar plates which electrically connect adjacent cells. This arrangement multiplies the ohmic power losses resulting from contact resistance between each gas diffusion layer (GDL) and BPP. Thus, contact resistance characteristics of BPP have significant effect on the overall PEMFC stack efficiency. Makkus et al. reported that per additional $25m\Omega$-cm^2 contact resistance results in a power loss in the order of 2-5% [27]. Carlson at al. estimated that the price of PEMFC would be three times higher if the stack resistance increases from 0.05Ω-cm^2 to 0.2Ω-cm^2 [30]. Therefore, the desired performance level of the PEMFC significantly depends on low contact resistance between BPP and GDL. In a way, contact resistance in fuel cells is like the friction in the internal combustion engines (ICEs) wasting the generated energy and leading to low efficiencies. US Department of Energy (DOE) set the contact resistance goal for PEMFC applications as lower than $10m\Omega$-cm^2 at 140 N/cm^2 compaction pressure for year 2015 [29].

24

Researchers all over the world have been conducting investigations to overcome contact resistance issues by understanding the underlying mechanisms and bringing alternative solutions to the interactive effects of surface conditions, coatings, substrate materials, manufacturing and assembly on the electrical contact resistance and its consequences on the overall fuel cell performance and durability [2-7,22,27,30].

2.4.3. Studies on Bare Stainless Steel BPPs

Metallic bipolar plates have been attracting attention because of their advantages over graphite and composite BPPs such as excellent bulk conductivity, high strength, high chemical stability, wide range of choice, ability for mass production and low cost. Various grades of stainless steels put forward as BPP material candidates due to their higher formability and corrosion resistance than that of other metallic candidates.

Hornung and Kappelt conducted one of the early studies on metallic BPP by investigating possible use of Fe based material as BPP in PEMFC [64]. Davies et al. investigated various stainless steels in terms of their contact resistance and corrosion resistance characteristics [65]. They reported that stainless steel 316, 310 and 904L had satisfactory corrosion resistance as BPP materials. Wang et al. tested corrosion resistance of different austenitic stainless in simulated fuel cell environment and compared their contact resistance behavior [14]. They found that increasing Cr content reduces ICR of stainless steels. Kim et al. studied the effect of alloying element in various stainless steel families. They reported the importance of Mo content beside Cr content in point of view ICR. Kraytsberg et al. investigated effect of surface structure of SS 316L on ICR [66]. They registered that high increasing roughness is beneficial to lower ICR between stainless steel BPP and GDL, unlikely conventional metal-metal electrical contacts. In

25

another attempt by Andre et al., effects of roughness, bulk composition of the alloy, composition and structure of passive films, surface treatments and aging conditions on ICR were studied for 316L and 904L stainless steel grades by Andre et al. [22]. In accordance with Kraytsberg et al. study, Andre et al. registered lower ICR with higher roughness on SS 316L and 904L. Bulk composition of alloy was found to have slight impact on ICR but passivation pre-treatment can deeply modify passive film and has a strong effect on ICR value. Andre et al. noted that uncoated SS with proper low-cost chemical passivation can noticeably reduce ICR and become a moderate solution in between use of as-received SS material and precious coating. It was also revealed that strain is destructive for the passive film integrity, so that BPP plates should be formed before any sort of surface treatment.

2.4.4. Studies on Coated Stainless steel BPPs

In order to exploit the stainless steel BPPs with sufficient corrosion resistance and contact conductivity at reasonable cost levels, metallic plates with protective coatings have been extensively studied. [2,15,16,28,67-71]. Coatings for metallic bipolar plates can be categorized into two groups as carbon-based and metal-based coatings. The carbon-based coatings include diamond-like carbon (DLC), conductive polymers and organic self-assembled monopolymers. Noble metals, metal nitrides and metal carbides are part of the metal-based coatings [2-4,24,34].

Several coating methods such as physical vapor deposition (PVD) [72-76], chemical vapor deposition (CVD) [67,77], plasma coating [78], and surface nitriding [35,74,76,79-81] have been investigated to improve surface properties of the thin sheets of stainless steel alloys. PVD coating of the metal nitrides have been widely preferred in literature to increase corrosion resistance and decrease contact resistance of the metallic BPPs [72-76]. Several studies reported

26

performance evaluation of different coatings such as TiN [28,69-71,82-84], CrN [74,76,79,80,85-89] and ZrN [90,91] on stainless steel substrate materials. Most of the literatures reported testing of bulk or unformed sheet materials instead of actual formed BPP samples.

2.4.5. Relationship Between Manufacturing Process and Electrical Contact Behavior

It is well known as reported in the literature that there is a direct interaction between bipolar plate surface condition and the ICR [66,92]. Hence, the manufacturing of BPPs is considered as an important factor since type and process parameters of manufacturing influence the surface conditions of BPPs. Manufacturing process imposes the contact geometry which is effective on contact pressure, contact area and contact uniformity. Matsuura et al. experimentally and numerically investigated the effect of compression of stamped BPP on GDL structure. They concluded that sufficient amount of contact was obtained between BPP and neighboring parts [93]. Also, they showed that excessive compression may lead serious damages on GDL. Liu et al., on the other hand conducted a robust design analysis on fuel cell stack in order to investigate the effect of assembly parameters on the MEA pressure distribution [94]. Liu et al. used FEA and statistical simulation to investigate random dimensional error of BPP on GDL pressure distribution [95].

Several production methods such as machining, stamping, die casting, investment casting, powder metal forging, electroforming, stretch forming, and hydroforming were proposed and investigated for fabrication of the metallic bipolar plates. Among these, stamping and hydroforming are believed to be the most suitable approaches for mass production [3,8,9,31,32,96-104]. The outstanding advantages of the stamping method are its faster

27

production rate and cost competitiveness, while hydroforming has the ability of delivering good and consistent surface topology, uniform thickness distribution and tight dimensional tolerances [32]. Therefore, this study was focused on these two manufacturing methods.

2.5. Introduction to Contact Resistance

2.5.1. Electrical Resistance

Ohm's Law relates the potential difference, V (in volts), with the electrical resistance, R (in ohms i.e.), and the electrical current, I (in amps) as follows.

$$V = RI \qquad (2\text{-}1)$$

The resistance of a conductor can be calculated from its physical dimensions by

$$R = L\,\frac{\rho}{A} \qquad (2\text{-}2)$$

where L is the length of the conductor, A is its cross-sectional area, and ρ is the specific resistance, or resistivity (Ω-cm). The resistivity is independent of specimen geometry. Sometimes, electrical conductivity is used to state the electrical character of a material. It is simply the reciprocal of the resistivity with unit of Siemens (S).

$$\sigma = \frac{1}{\rho} \qquad (2\text{-}3)$$

2.5.2. Resistivity of materials

Range of electrical resistivity in solid material extends 27 orders of magnitude [105]. This is the widest variation for any physical property. According to their resistivity materials are classified as conductors, semiconductors and insulators.

28
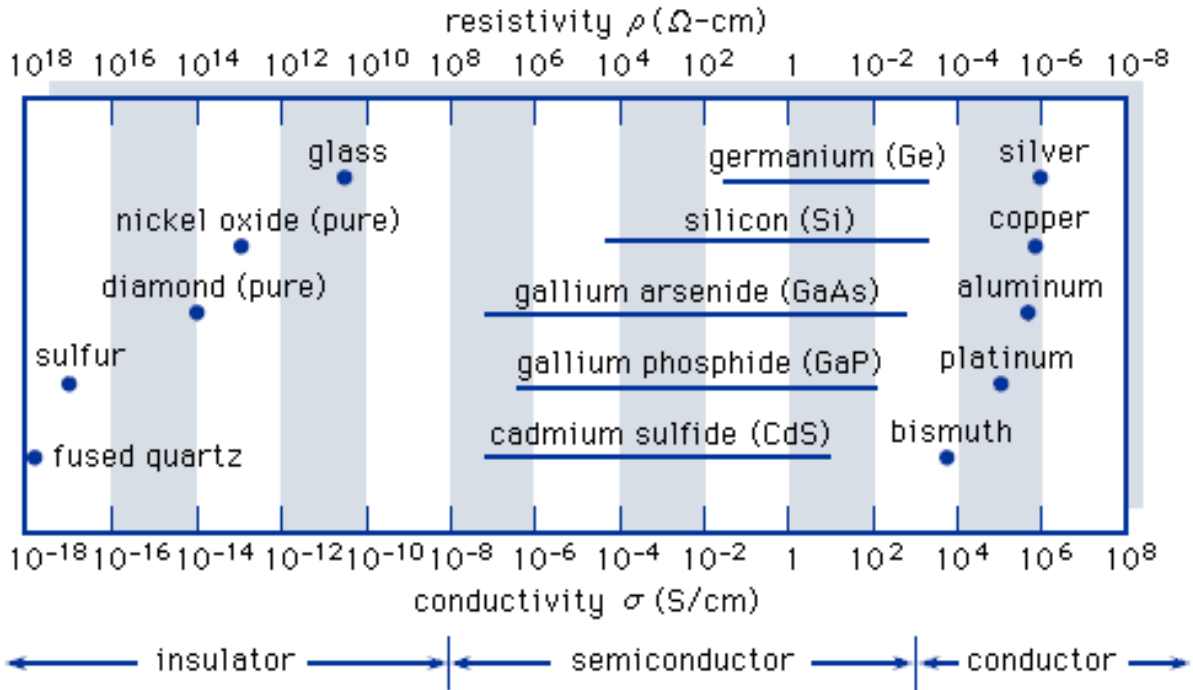
Figure 2-8 Resistivity of materials [britannica.com].

2.5.3. Theory of Electrical Conduction in Solid State Physics

Electric current is a flow of electrically charged particles in reaction to forces from an electric field. A current consists from the flow of electrons, which is called electronic conduction, within most solid. A motion of charged ions in an electrolyte, or both ions and electrons in a plasma can cause an electric current. This type of current is called ionic conduction.

Only electronic conduction exists in all conductors, semiconductors, and many insulator materials. The magnitude of the electrical conductivity is mainly dependent on the number of electrons available to participate in the conduction process. Nevertheless, not all the electrons in every atom are involves the conduction. The arrangement of electron states are occupied by electron determines the number of electrons available for electrical conduction in a particular material and the conductivity of solid materials is explained with band structure of the electron in

29

quantum mechanics [106]. Since a thorough exploration of the topic is beyond this study, simple explanation of the topic was presented below.

Band structure of a solid material is the arrangement of the outermost electron bands and the manner they are filled with electrons. Four different types of band structures are possible at temperature of absolute zero as depicted in Figure. Electrons in valence band do not involve electrical conduction. Electrons in conduction band can be accelerated by external electric field and cause current. There are two possible band structures for conductor: valance and conduction bands overlap each other or electrons exist in conduction band. However, in insulators, conduction and valance bands are separated by a large band gap. This band gap is narrow for semiconductor and valance electrons can pass to conduction band with an external excitation like temperature.
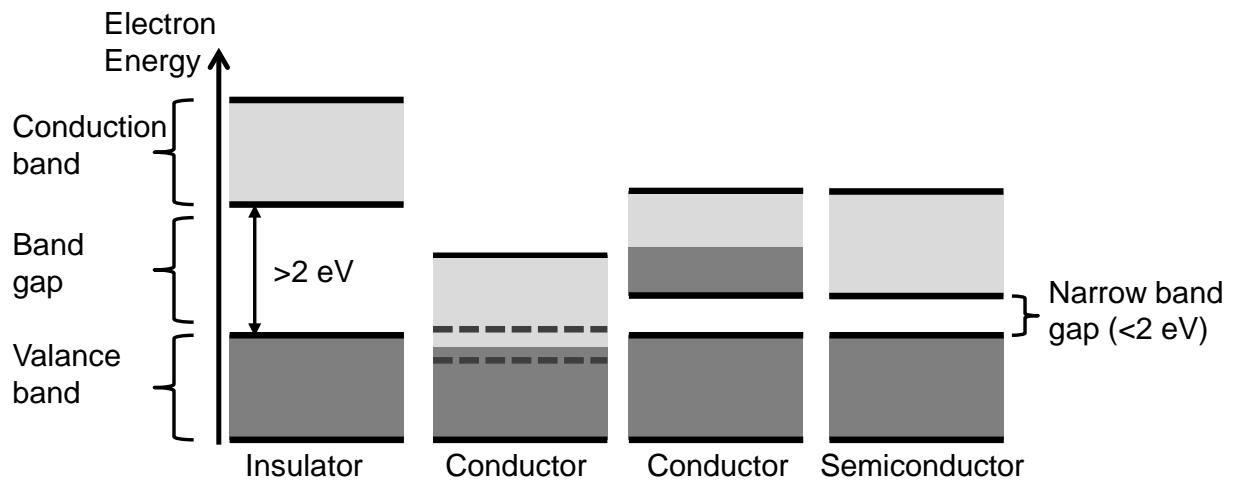
Figure 2-9 Schematic representation of band structure of electrons.

2.5.4. Factors effecting resistivity

There is no interaction between a moving electron and atoms in a perfect crystal lattice according to quantum mechanics. However, imperfections in the crystal lattice, including

30

impurity atoms, vacancies, interstitial atoms, dislocations and even the thermal vibrations of the atoms themselves cause scattering of electrons [107,108]. These scattering events act like frictional forces and originate the resistivity. Increasing number of crystalline defects raises the resistivity. The intensity of these imperfections depends on temperature, composition, and the amount of cold work of a metal.

Matthiessen's rule represents the individual thermal, impurity and deformation resistivity contributions, respectively. The influence of each variable on the resistivity is depicted in Figure 2-10.

$$\rho_{total} = \rho_t + \rho_i + \rho_d \qquad (2\text{-}4)$$

The resistivity for the pure metal and all the copper-nickel alloys rises linearly with temperature above about -200C due to increase in thermal vibrations and other lattice irregularities (e.g., vacancies), which acts as electron scattering centers. The temperature coefficient of resistivity, α, is an important material property as defined by the equation

$$\rho_T = \rho_0(1 + \alpha\Delta T). \qquad (2\text{-}5)$$

Where ρ_0 is the resistivity at 20°C and ΔT is the temperature difference relative to 20°C. At cryogenic temperatures the resistivity is nonlinear and varies as $\sim T^5$ whereas at elevated temperatures α is constant.

Alloying elements always increase the resistivity of the metal to which they are added. However, semiconductors and insulators become better conductor when alloyed. The change in resistivity of copper with some elements is shown in Figure 2-12 [109].

According to Fuchs-Sonderheimer theory scattering of the electrons with the surfaces of thin films leads to increase of resistivity [110,111]. Mayadas and Shatzkes showed that a reduction of the grain size in thin films causes a substantial resistivity increase due to scattering with grain boundaries [112]. Two types of size effects in polycrystalline films, film thickness and grain size, affect the electrical resistivity. Due to surface scattering of the conduction electrons, resistivity increases as the layer thickness decreases. Grain boundary scattering is another contributor to the film resistivity and smaller grain size films show higher resistivity than larger grain size films. Dependence of the grain size to film thickness makes the size effect very complex. The size effect becomes more important when the film thickness, t, is comparable with the electron mean free path, l_0. Resistivity of thick films, where $l0<t$, is cited as

$$\rho = \rho_0 \left(1 + \frac{3}{8} \frac{l_0}{t} \right) \qquad (2\text{-}6)$$

where ρ_0 is the resistivity of single crystal [113].In a recent study Sun et al. compared the significance of the film thickness and grain size on resistivity for various nanometric Cu films at temperature of 4.7 K and they concluded that grain size is more dominant than film thickness on resistivity [114]. Density and stress are also known as properties which affect the electrical properties of films [113,115].
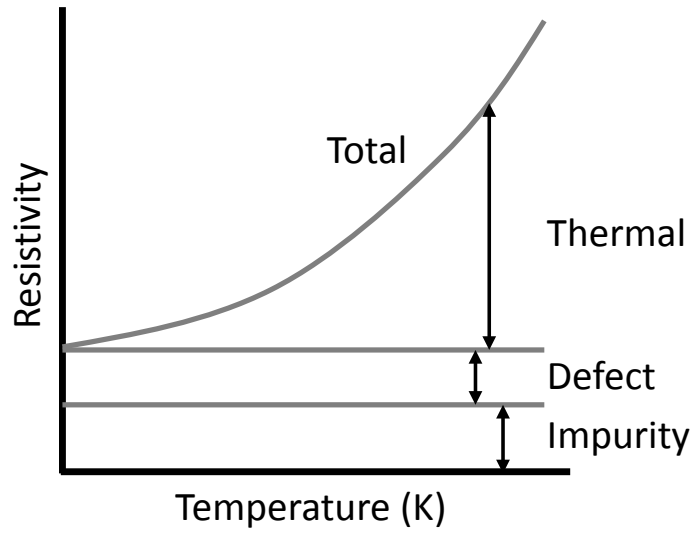
Figure 2-10 Contributors of resistivity in metals.
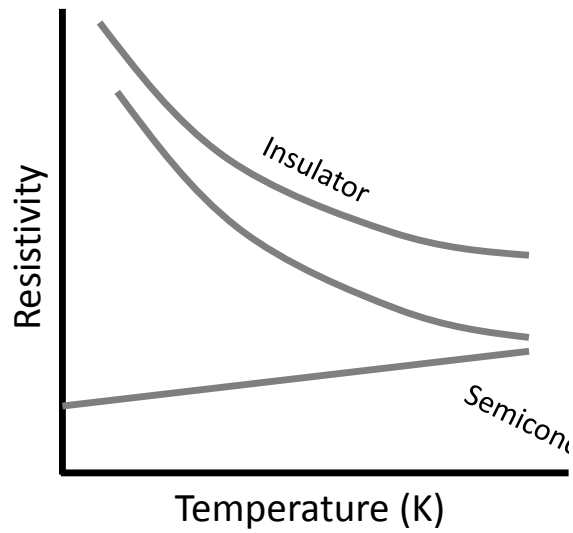
Figure 2-11 Effect of temperature on resistivity.
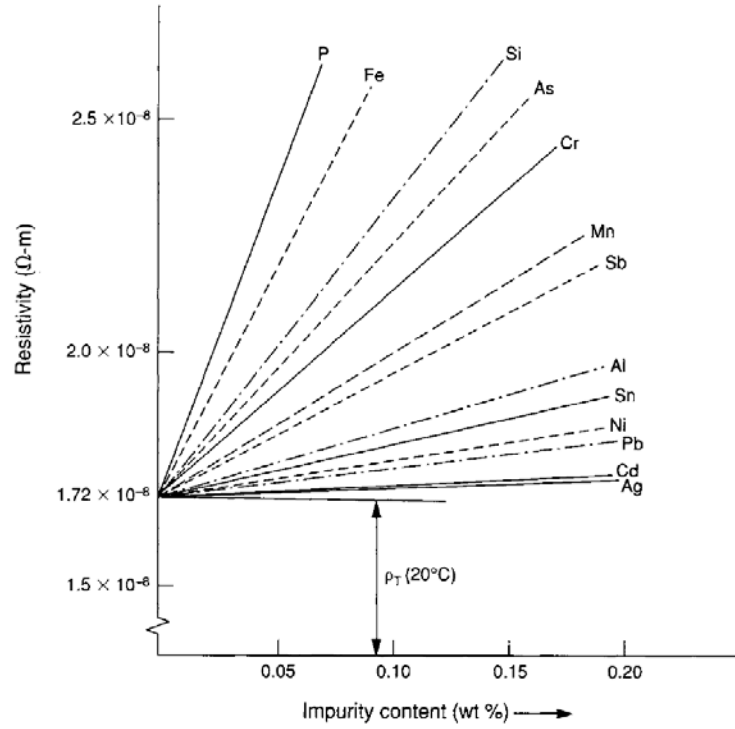
Figure 2-12 Effect of alloying element and content on resistivity of copper [109].
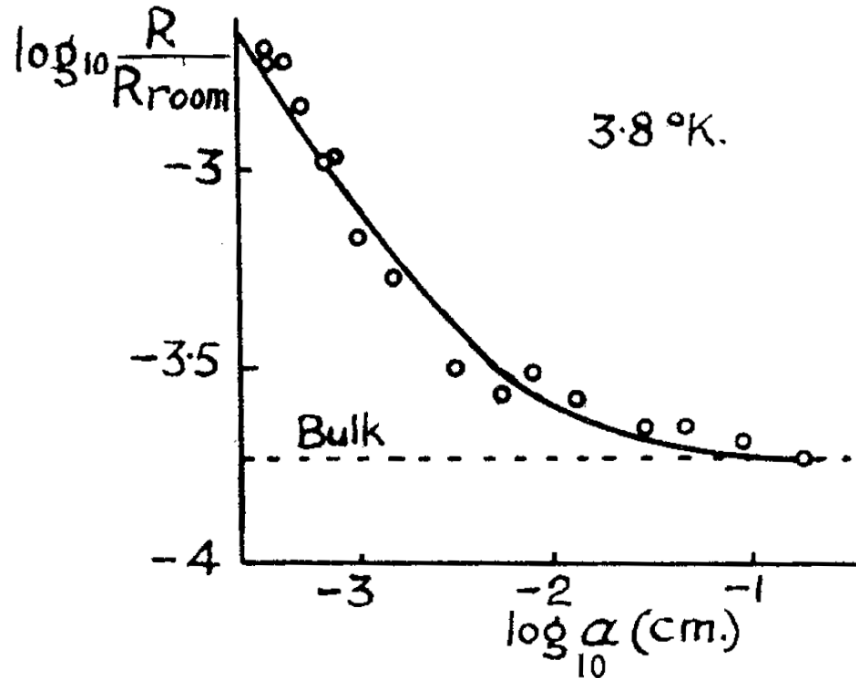
Figure 2-13 Experimental results on the resistivity of tin foils at 3.8 ° K [111].

34

www.manaraa.com

2.5.5. Theory of Contact Resistance

Theory of contact resistance between two solid bodies is well established. It is well known that all solid surfaces are rough in micro scale. Contact between two bodies occurs at discrete asperities on the two surfaces. True contact area is a small fraction of nominal area, which is leading to a voltage drop across the interface, for wide range of clamping force.

When a contact size is much larger than the mean free path of electrons, contact resistance is expressed by Holm equation (2-7) [116]:

$$R_H = \frac{\rho}{2r} \qquad (2\text{-}7)$$

Here ρ is the bulk resistance and r is the contact radius for a circular contact. When contacting bodies are two different materials, the equation becomes in equation (2-8):

$$R_H = \frac{\rho_1 + \rho_2}{4r} \qquad (2\text{-}8)$$

In this case ρ_1 and ρ_2 are bulk resistances of contacting bodies.

Sharvin resistance, as expressed (2-9), is valid when the contact size is much smaller than the mean free path of electrons in material Sharvin [117].

$$R_{Sh} = \frac{4\rho l_e}{3\pi r^2} \qquad (2\text{-}9)$$

Here l_e is the mean free path of electrons in material. It is intuitively clear and experimentally supported that if contacting bodies are compressed to each other, the contact resistance decreases as pressure increases [118].

35
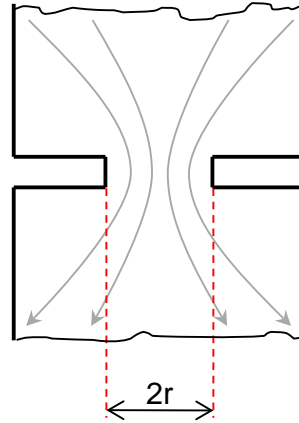
Figure 2-14 Schematic of constriction resistance.

Significant amount of literature exist on the modeling of electrical contacting bodies and they are quite useful in understanding the electrical resistance between two contacting solid bodies. On the other, in fuel cell, contact resistance generally occurs between solid and porous media. Recently, several microstructure based models have been proposed to explain the contact resistance between BPP and GDL [119,120]. While all these complex models are material and surface topography depended, a power function based on experimental data is quite useful to define relationship between compaction force and ICR [121]:

$$R = a \cdot (P)^b \qquad (2\text{-}10)$$

where, a and b are fitting parameters based on experiments and P is clamping pressure. Zhou et al. presented some fitting values based on experimental works in literature [121].

36

Table 2-2 Power function fitting coefficients of the contact electrical resistivity [121].

Contact interfaces	a	b	Average error	References
GDL (10BA CP)/BPP (Graphite)	3.23	-0.484	4.7%	[122]
GDL (10BB CP)/BPP (Graphite)	3.61	-0.699	4.29%	[122]
GDL (10BB CP)/BPP (Graphite)	18.4	-1.08	5.13%	[123]
GDL (CP)/BPP (Carbon composite)	36.9	-0.148	2.78%	[124]
GDL/BPP (316L Bright annealed)	220	-1.01	0.26%	[22]
GDL (Toray CP)/BPP (316L)	222	-1.05	4.03%	[14]

CHAPTER 3: Effect of Manufacturing Processes on Contact Resistance Characteristics of Metallic Bipolar Plates in PEM Fuel Cells[1]

In this section, metallic bipolar plate (BPP) samples manufactured with stamping and hydroforming under different process conditions were tested for their electrical contact resistance (ICR) characteristics to reveal the effect of manufacturing type and conditions. Punch speed and force in stamping, and pressure and pressure rate in hydroforming were selected as variable process parameters. In addition, two different channel sizes were tested to expose the effect of BPP micro-channel geometry and its consequences on the contact resistance. As a general conclusion, stamped BPPs showed higher contact conductivity than the hydroformed BPPs. Moreover, pressure in hydroforming and geometry had significant effects on the contact resistance behavior of BPPs. Short term corrosion exposure was found to decrease the contact resistance of bipolar plates. Results also indicated that contact resistance values of uncoated stainless steel BPPs are significantly higher than the respective target set by U.S. Department of Energy. Conforming to literature, proper coating or surface treatments are necessary to satisfy the requirements.

Keywords: Contact resistance, metallic bipolar plates, PEMFC, stamping, hydroforming, micro-channel

---

3.1.Introduction

Quite a few studies are available in the literature discussing the corrosion and contact mechanics of various BPP materials [3,21,23,33-35]. The effect of manufacturing process on the corrosion resistance of metallic BPPs were investigated previously [58,59]. Nonetheless, as far as the literature review made by authors is considered, there has not been any study dedicated to the effect of manufacturing processes on the electrical contact resistance of metallic bipolar plates. Thus, this study aims to bring about a broader understanding of manufacturing effects (process, material, coating type, coating thickness, coating and manufacturing process sequence) on the BPP contact resistance. This understanding is expected to help having a complete picture of the performance of the stainless steel bipolar plates manufactured through stamping and hydroforming. The next section describes the experimental methodology and conditions followed to test the contact resistance characteristics of various metallic alloys manufactured under different process conditions. In the third section, results of experiments are presented and discussed, and it is followed by the fourth section where conclusions are withdrawn.

3.2. Experimental Methodology and Conditions

3.2.1. Manufacturing of Bipolar Plate Samples

In this study, SS304 and SS316L bipolar plates with micro-channels on them were manufactured using stamping and hydroforming methods. Alloy compositions of materials presented in Table 2-1. Two different die geometry designs with parallel channels were employed to manufacture bipolar plate samples in both stamping and hydroforming. Each die insert set (male and female inserts) was placed in the insert holders. Both die inserts were used in stamping, while only female insert was needed in hydroforming. The height of the micro-channels on the die inserts were 750µm and 250µm for large and small inserts, respectively, as can be seen in Figure 3-1 along with the corresponding bipolar plates formed with these dies.

An Instron Satec 5596-400HVL (Instron Corp., Norwood, MA, USA) mechanical testing system (MTS) was used to apply stamping force and maintain the punch speed in stamping while it was used to provide the clamping force during the hydroforming process. The system along with hydroforming and stamping setups was depicted in Figure 3-2. The pair of die inserts with 750 µm channel and die holders set is also shown in Figure 3-3.

Several manufacturing process parameters of interest, such as manufacturing method; punch speed and force in stamping; pressure and pressure rate in hydroforming; geometry, and BPP material, were tested to disclose their effects on the ICR. Furthermore, BPPs that were initially exposed corrosion tests were subjected to ICR tests to investigate effect of short term corrosion on the ICR.

40

Table 3-1 Chemical composition of SS316L and SS304 (wt. %).

	C	Mn	P	S	Si	Cr	Ni	Mo	Cu	N	Fe
SS 304	0.067	1.09	0.026	-	0.58	18.47	8.44	0.05	0.09	0.026	Bal.
SS 316L	0.021	1.48	0.033	0.001	0.43	16.20	10.03	2.06	0.43	0.04	Bal.

Supplier's Data (Browns Metals Co., Rancho Cucamonga, CA, USA)
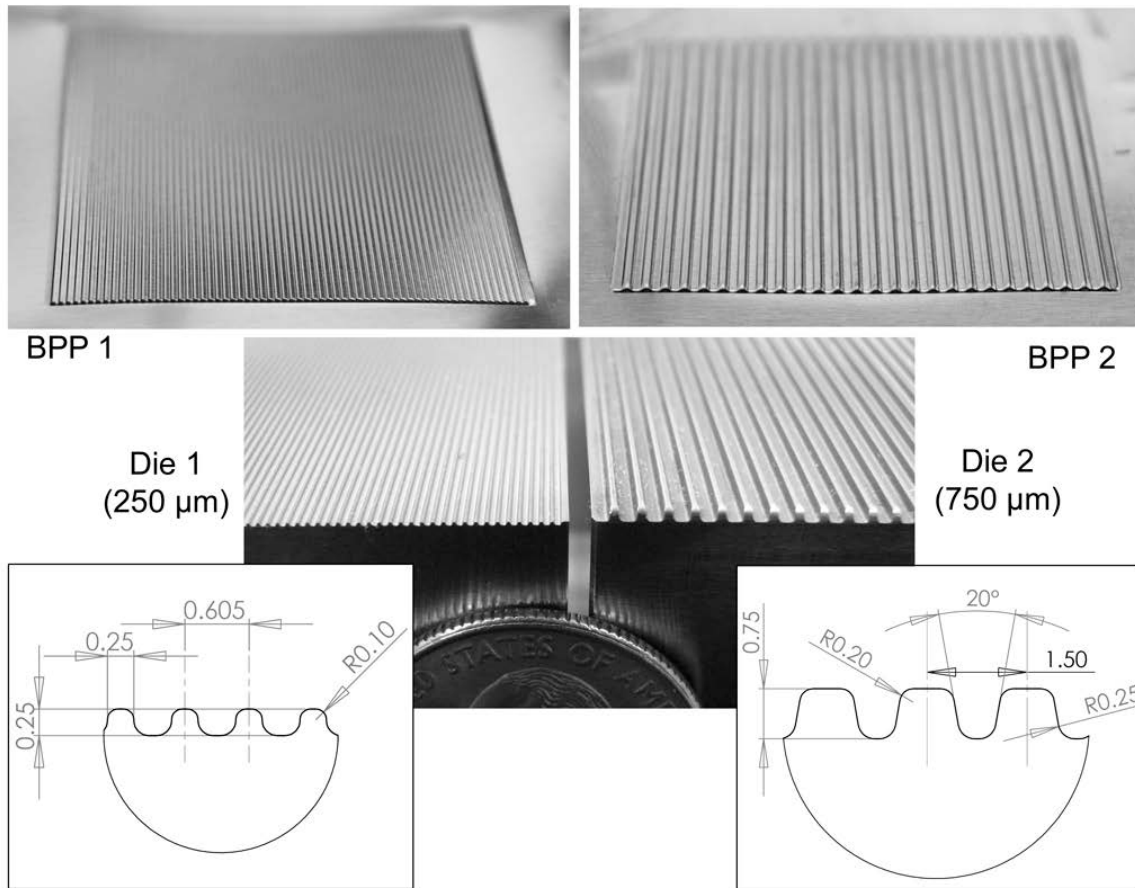
Figure 3-1 Photographs and sketches of two different bipolar plates and dies (BPP and its die with 250μm channel height are on the left side while same of that 750μm micro-channel height are given on the right side).
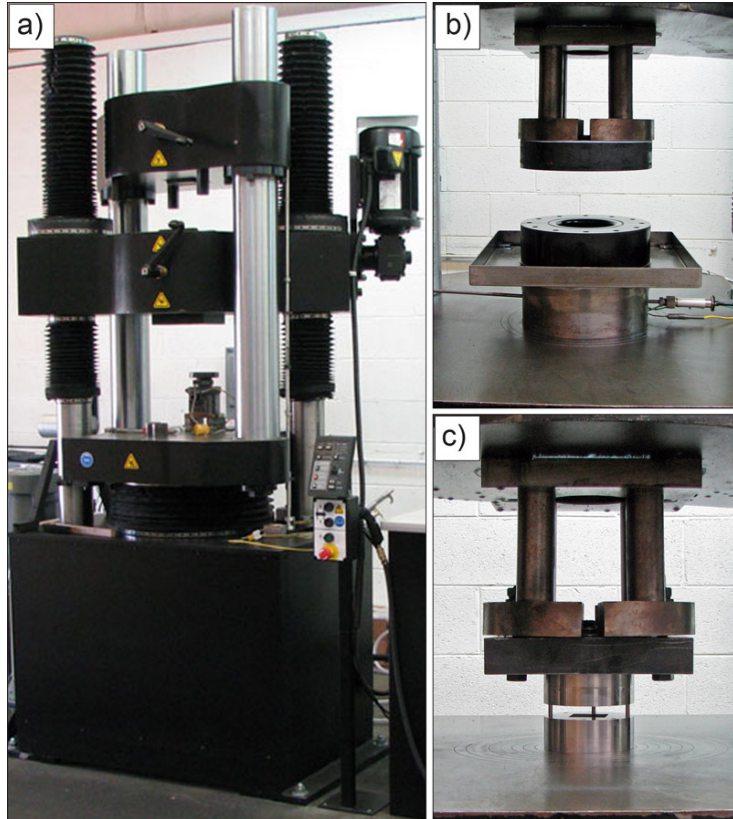
Figure 3-2 Equipment that used to form BPP samples. a) Instron Satec 5596-400HVL mechanical testing system, b) hydroforming and c) stamping setup.
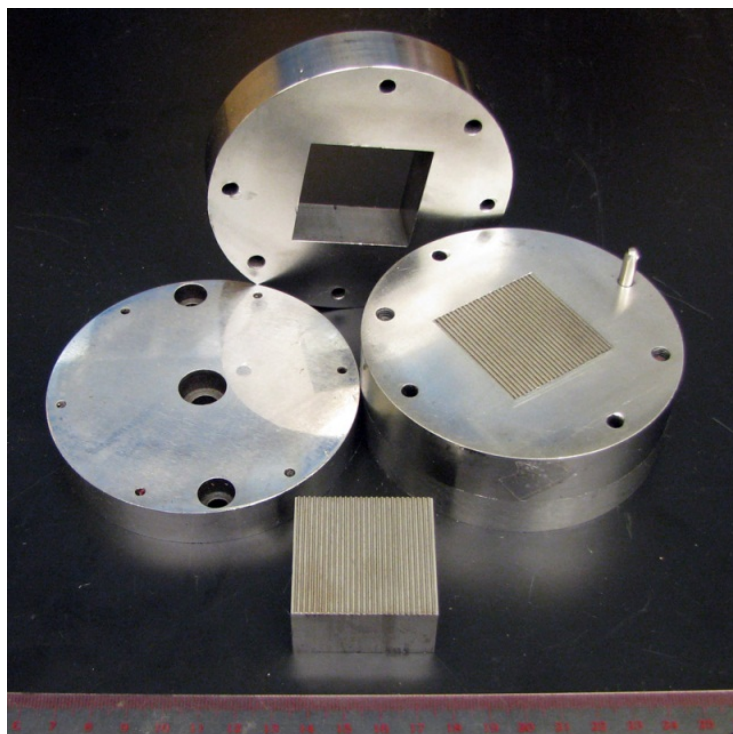
Figure 3-3 The pair of die inserts with 750 µm channel and die holders set.

42
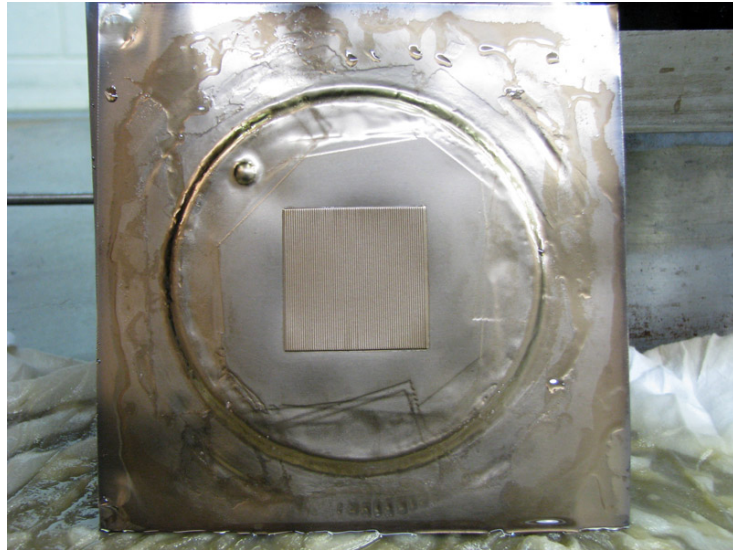
Figure 3-4 A formed BPP sample right after the hydroforming process.
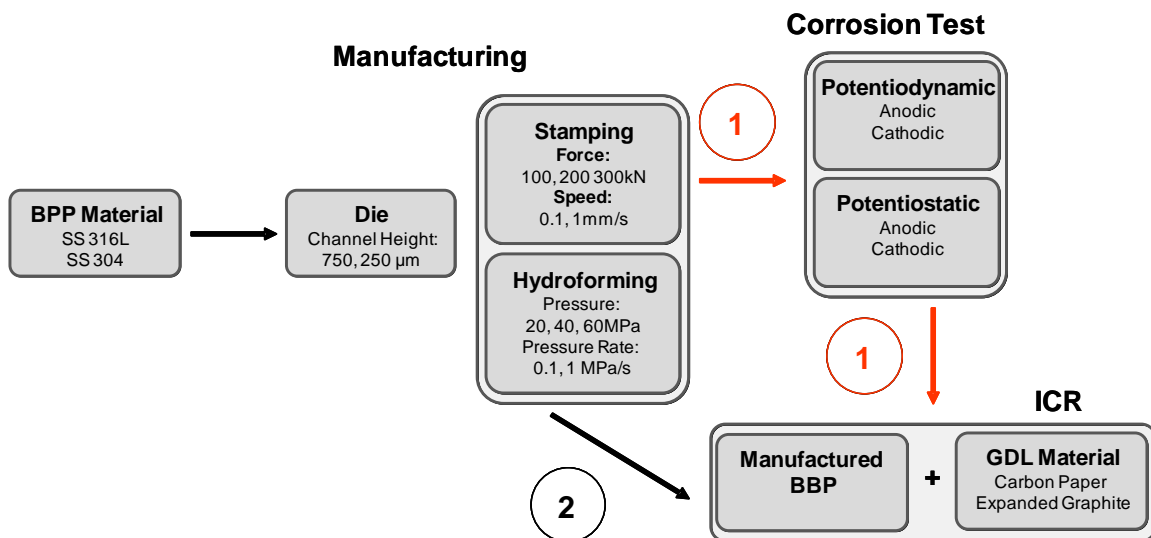
Figure 3-5 Experimental variables and two different test sequences followed.

3.2.2. Dimensional Measurements

Dimensional measurements on the manufactured BPP samples were performed by using laser displacement sensor and stylus profiler. Keyence LK-G37 (Keyence Corp. of America, Itasca, IL) laser displacement sensor with 0.05 µm vertical resolution combined with a motorized

43

stage (MM-4M-EX-140, National Aperture, Salem, NH, USA) was employed to measure channel heights on the BPP samples (Figure 3-6). Ambios XP-1 stylus profiler was also used to reveal detailed channel profile of the BPP samples (Figure 3-7). Results of the measurements were summarized and related to ICR at next sections.
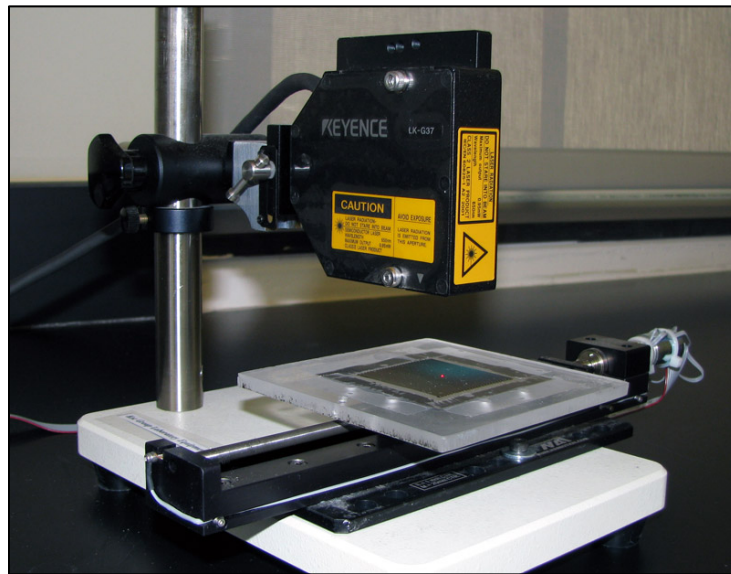
Figure 3-6 Laser displacement sensor (Keyence G37) with motorized stage (National Aperture MM-4M-EX-140).

Figure 3-7 Stylus profiler (Ambios XP1).

44

3.2.3. Surface Characterizations

BPP surfaces were investigated with HIROX KH-7700 (HIROX-USA, NJ, USA) confocal optical microscope. Surface roughness was also determined quantitatively by using Wyko NT1100 optical profiler (Veeco Instruments Inc., Tucson, AZ, USA). Roughness data were taken from channel tips by scanning of 450.6µm x 600.8µm areas. JOEL JSM-5610 scanning electron microscope (SEM) and µSURF EXPLORER non-contact 3D surface measurement system were employed to examine GDL structure. Surface characterization results with obtained images were presented in Section 3.3.2.

3.2.4. Contact Area Measurements with Pressure Sensitive Film

Contact areas of formed BPP samples were measured by using pressure sensitive film (Pressurex Super Low, Sensor Products, NJ, NJ, USA) to be able to calculate area specific contact resistance (ASR) which is commonly used in literature to compare BPP material for contact resistance performance. Films were placed between BPP and GDL at both sides of BPP. Contact areas were imprinted on films during compression test in which compression forces used similar to use in ICR test. In BPPs with 750 µm channel height, hydroformed and stamped samples resulted similar contact areas (Figure 3-8). However, contact areas cannot be measured on BPPs with 250 µm-channel due to very close features (Figure 3-9). For 750 µm channel case, after compression test imprinted films were photographed by digital camera and scaled pictures, as shown in Figure 3-8, were analyzed by using Image J software to calculate contact areas on films based on ratio between imprinted and untouched areas [125]. This procedure was repeated for all compaction forces used ICR test and contact areas by compaction force were obtained as depicted in Figure 3-23 (Section 3.3.3.). Area measurement procedure was confirmed by FEA

45

analysis with a good agreement between two methods. Due to assumption of even pressure distribution on imprinted area and limited precision of pressure sensitive film and calculation procedure, this evaluation was considered as an approximation. Therefore, ICR values of formed BPP samples were presented and compared in terms of total contact resistance (mΩ), independent from area, throughout the study, in general.
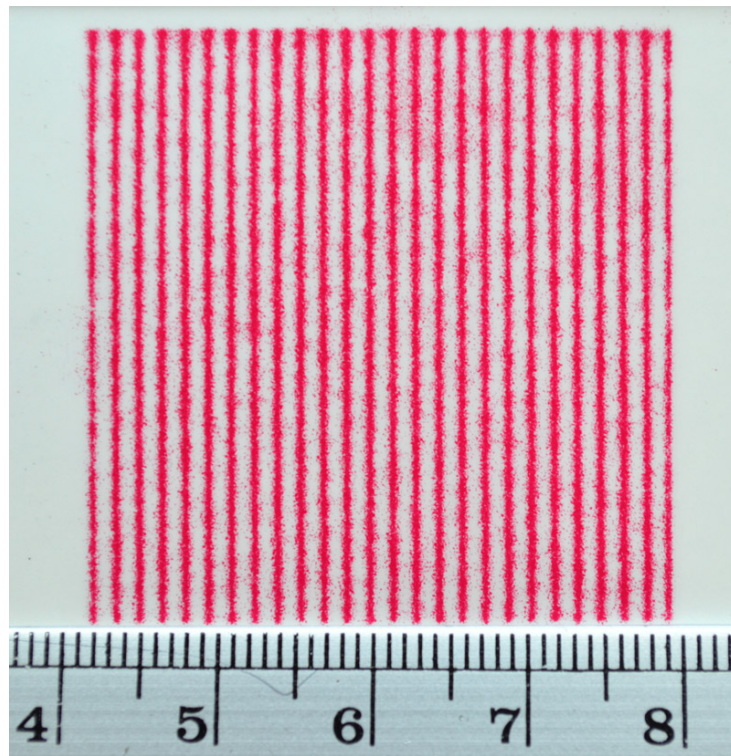
Figure 3-8 Pressure sensitive films showing contact area on BPP formed with 750 µm channel height dies in ICR test.
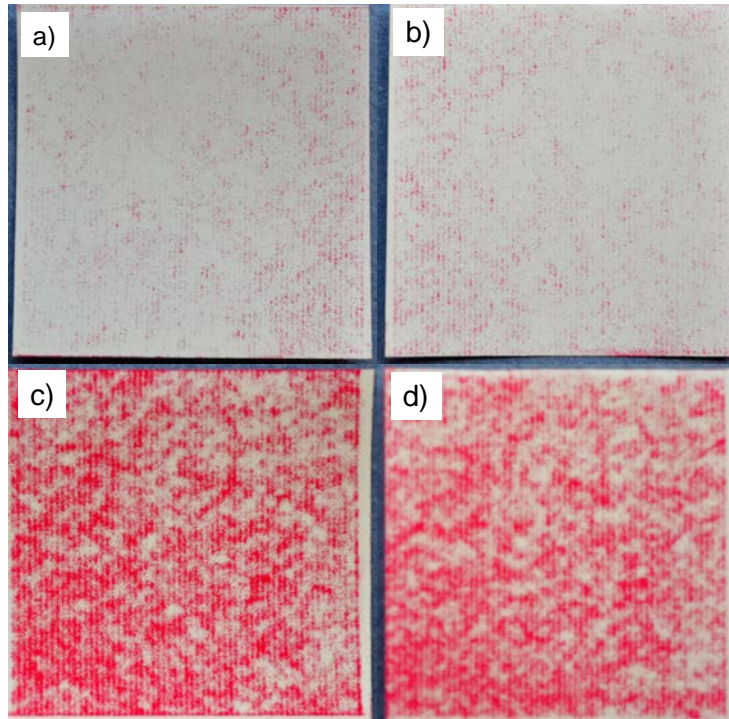
Figure 3-9 Pressure sensitive films showing contact area on BPP formed with 250 µm channel height dies in ICR test. a) Front side b) backside of stamped BPP (with "low" grade film), c) front side and d) backside of Hydroformed (60 MPa) BPP (with "very low" grade film).
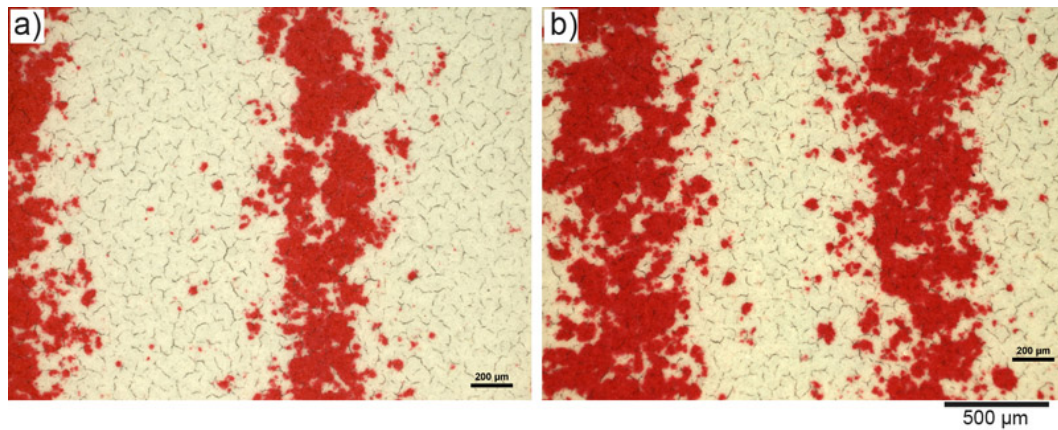
Figure 3-10 Microscopy images of pressure sensitive films indicating contact area between BPPs formed with 750 µm-die and GDLs. a) Upper side and b) backside of BPP.

47
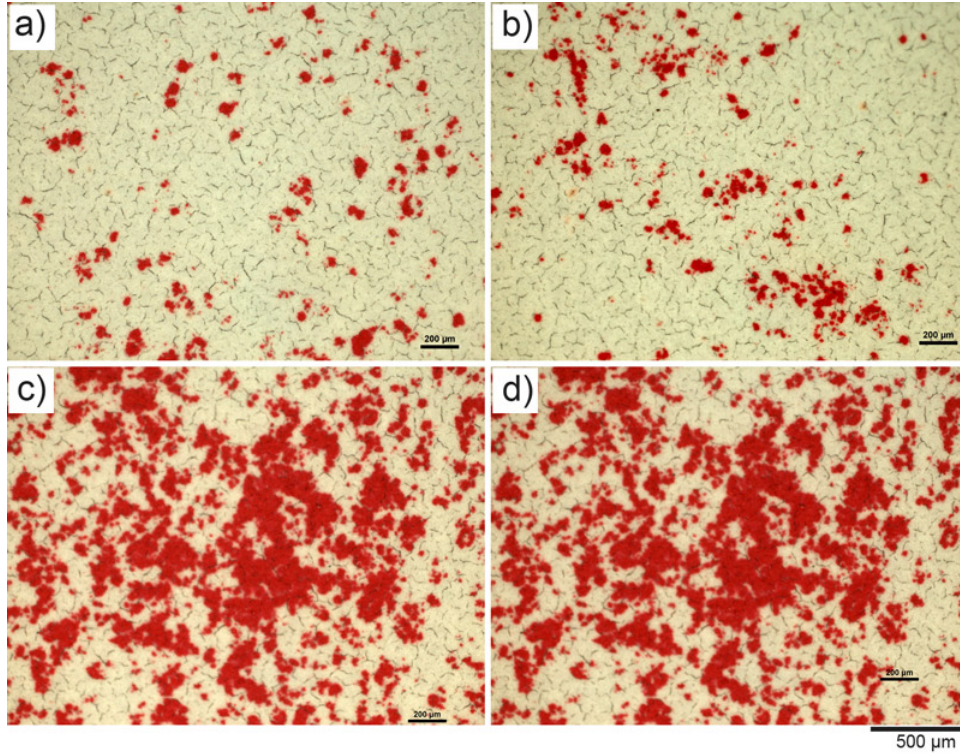
Figure 3-11 Microscopy images of pressure sensitive films intended to measure contact area between BPPs formed with 250 µm-die and GDLs.

3.2.5. Contact Area Calculations with FEA

Finite element analysis was used to simulate ICR test, and to obtain contact areas between BBPs and GDLs. Because channel length is much larger compared to channel cross-section, plain strain condition was assumed and 2-d modeling with one channel was established based on measured channel profile geometries. BPPs and GDLs were modeled with 4-node quadrilateral, 2-d solid plain-strain elements while current collectors were assumed as rigid bodies. Total numbers of elements in model (current collectors, BPP and GDLs) was 1936. Coulomb's friction model with coefficient of friction of 0.1 was used between parts. Material properties used in the simulations were presented in Table 3-2. Figure 3-12 shows the finite element model of ICR test.

Table 3-2 Mechanical parameters used in simulations.

	BPP	**GDL**[126]
Modulus of elasticity (GPa)	193	10
Poisson's ratio	0.3	0.09
Density (kg/m^3)	7500	1000
Material model	Power law, $\sigma = 1058 \cdot \varepsilon^{0.28}$	Linear Elastic
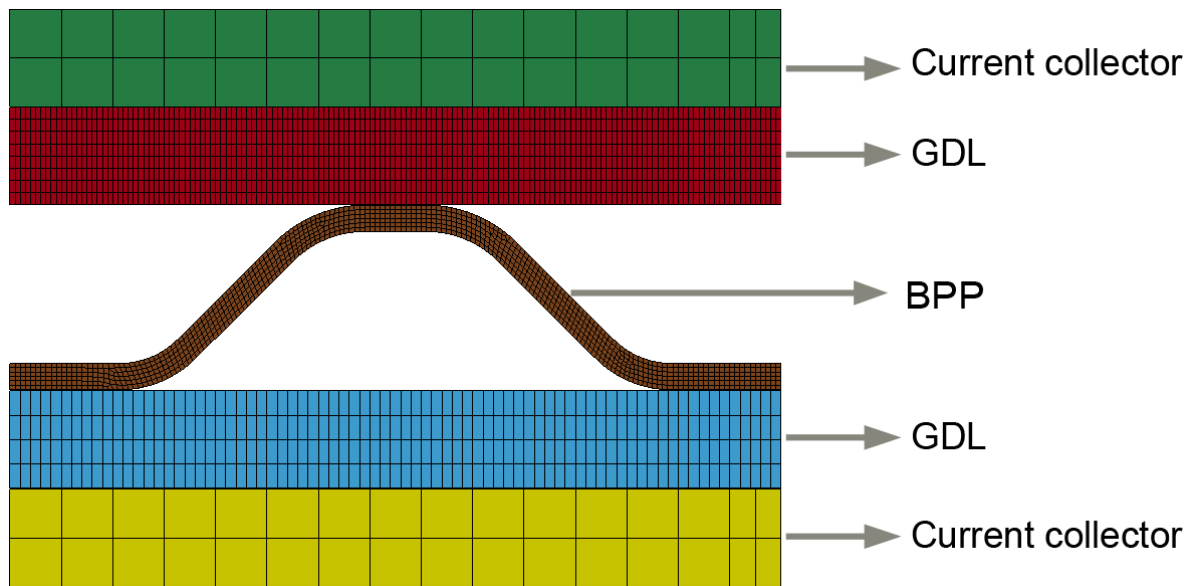
Figure 3-12 Finite element model of ICR test.

3.2.6. Interfacial Contact Resistance (ICR) Tests

In general, two types of measurement methods are used to determine ICR between BPP and gas diffusion layer (GDL). Ex-situ ICR measurement techniques allow users to approximate the contact resistance with relatively simple set-up and quickly. On the other hand, in-situ methods were developed to obtain more realistic measurement from operating single fuel cells or fuel cell stacks, particularly for extended time [27,127]. In this study, the ex-situ method, which was proposed and developed by Davies et al. [65] and modified by Wang et al. afterward [14], was followed for measurement of ICR.

Calibration measurements were needed to calculate ICR value between BPP and GDL. As schematically represented in Figure 3-13a, in the first configuration, the measured total resistance (R_{T1}) consists of bulk resistance of two current collectors (2_{RCC}), two interfacial contact resistance (ICR) between current collector and GDL ($2R_{CC/GDL}$), two bulk resistance of

50

GDL (R_{GDL}), two interfacial contact resistance between GDL and BPP ($R_{GDL/BPP}$), and bulk resistance of BPP (R_{BPP}). The R_{T1} can be expressed as follows:

$$R_{T1}=2R_{CC}+2R_{CC/GDL}+2R_{GDL}+2R_{GDL/BPP}+R_{BPP} \qquad (3\text{-}1)$$

In order to obtain $R_{BPP/GDL}$ term, an arrangement shown in Figure 3-13b was used. This configuration is consisted of bulk resistance of two current collectors ($2R_{CC}$), two interfacial contact resistances between current collector and GDL ($2R_{CC/GDL}$), and bulk resistance of GDL (R_{GDL}). Thus R_{T2} can be given as:

$$R_{T2}=2R_{CC}+2R_{CC/GDL}+R_{GDL} \qquad (3\text{-}2)$$

By using (3-1) and (3-2), ICR between the BPP and the GDL can be calculated as follows:

$$R_{BPP/GDL}= 0.5 (R_{T1} - R_{T2} - R_{GDL} - R_{BPP}) \qquad (3\text{-}3)$$

Since bulk resistances of GDL and BPP are negligible [22,128], ICR between GDL and BPP can be found by subtracting R_{T2} from R_{T1} and equation converts to following form:

$$R_{BPP/GDL}= 0.5 (R_{T1} - R_{T2}) \qquad (3\text{-}4)$$

Contact resistance values between the GDL and BPP samples (51µm thick, 316L and 304 stainless steel blank sheets and formed BPP samples with 16 cm^2 active area) were measured by using four-probe method. A bipolar plate specimen was sandwiched in between two GDL and they were placed between the two gold coated copper current collectors. Two Plexiglas plates used to electrically separate this group from testing system. The arrangements were depicted schematically in Figure 3-13 and exploded actual picture is presented in Figure 3-14. Electromechanical material testing system (MTS Insight 30, MTS Systems Corp., Eden Prairie, MN, USA) was used to provide compressive force. A micro ohmmeter (Agilent 34420A, Agilent Technologies, Santa Clara, CA, USA) was employed to measure total electrical resistance of the

51

setup (Figure 3-15). ICR of bipolar plates were measured and recorded in each step while applied force was elevated from 320 N to 4544 N with 384 N increments. Three specimens were tested for each case to monitor the repeatability of the tests.

Prior to tests, unformed (Blank), Hydroformed (Hf) and Stamped (St) BPP samples were degreased in ultrasound acetone bath during 30 minutes. Corroded samples washed with pure water and degreased in acetone bath without ultrasonic cleaning.
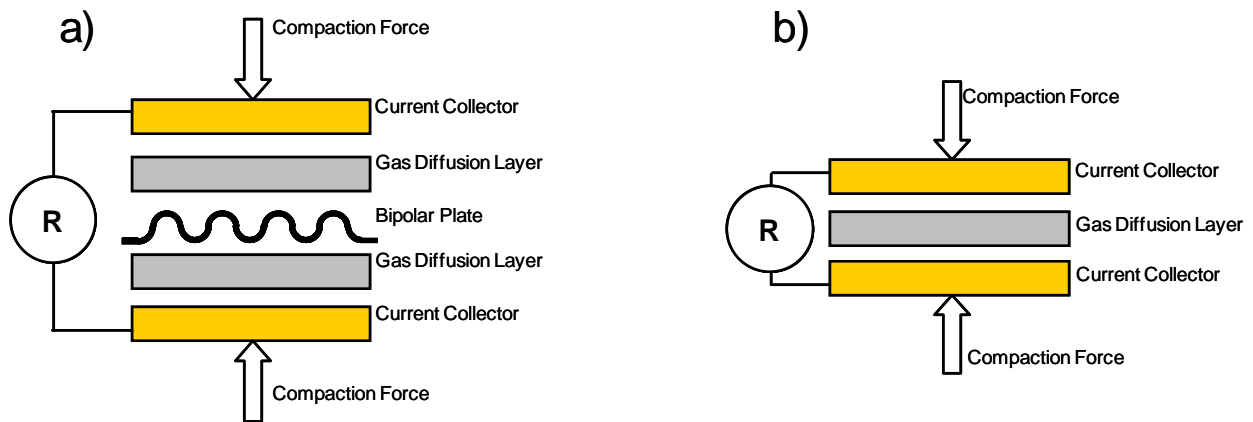
Figure 3-13 Two different component arrangements in a typical contact resistance test.
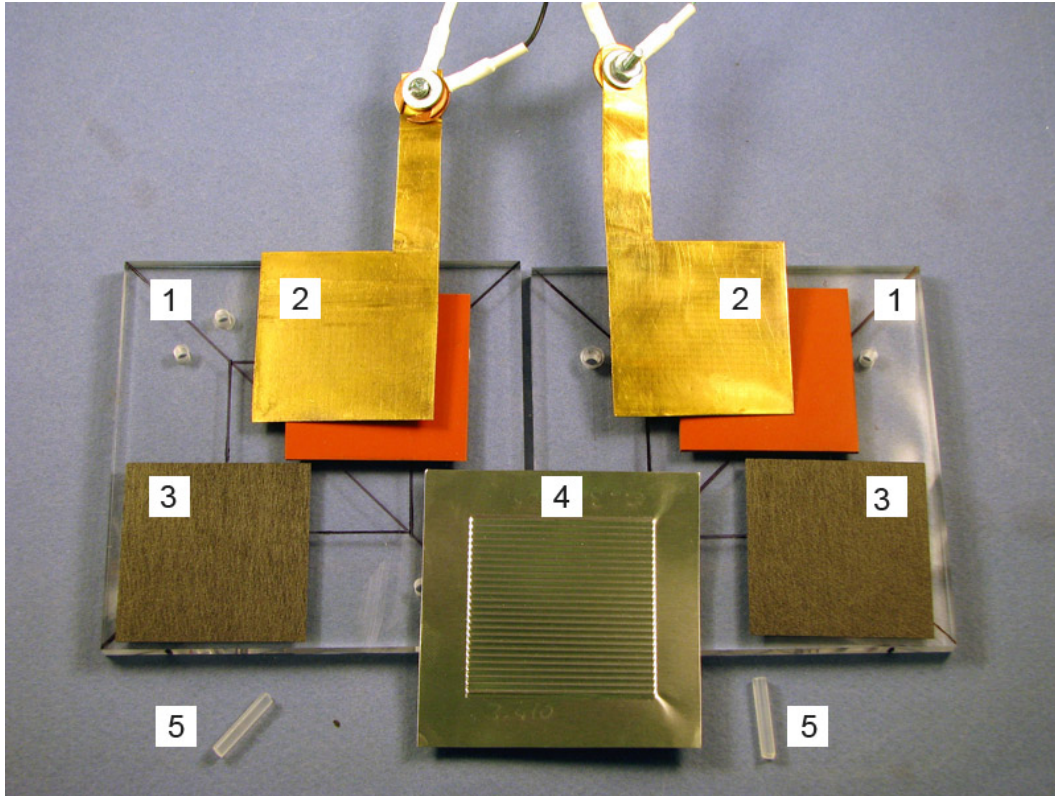
Figure 3-14 Elements of ICR test setup. 1- Plexiglas insulators, 2- gold plated copper current collectors, 3- carbon paper GDLs, 4- BPP sample, 5- alignment pins to keep together the setup.
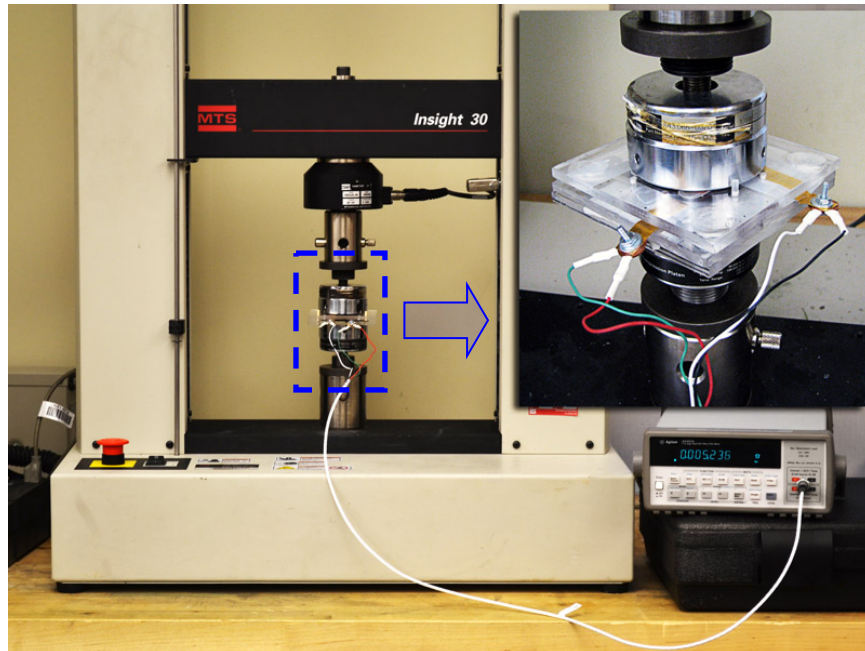
Figure 3-15 Mechanical testing system (MTS) and multimeter that used in ICR tests. Onset picture shows ICR setup between anvils of MTS.

53

3.2.7. Exposing Samples to PEMFC Conditions

In order to disclose effect of exposing PEMFC operating conditions on ICR of samples, contact resistance tests applied samples which previously subjected corrosion test. Two types of electrochemical tests, a potentiodynamic and a potentiostatic, were conducted to investigate the corrosion resistance of various BPP samples. H_2 and O_2 gases bubbled into test cell to simulate anodic and cathodic environments, respectively. 0.5M H_2SO_4 solution was used as the working electrolyte and the corrosion tests conducted in an electrical furnace at 80°C in order to simulate the PEMFC working conditions. The potentiodynamic experiments were performed in the potential range of -1.2 to 0.8V at a rate of 1 mV/s with respect to the reference electrode which is equivalent to standard hydrogen electrode (SHE) in the potential range of -1 to 1V. Tafel extrapolating analysis method including the intersection of two anodic and cathodic tangent lines was used to obtain corrosion current densities. The upper and lower limits (larger range) of the experiment were selected to include the anodic and cathodic transition potentials with an adequate offset for extrapolation. 0.6 V was also vs. reference electrode for cathodic condition with the oxygen purging. On the other hand, constant potentials of 0.6V, and -0.1V were applied during the 3 hour long potentiostatic experiments for O_2, and H_2 purges, correspondingly. Detailed explanation of the corrosion tests can be found in an earlier work [59].

3.2.8. Statistical Analysis

To investigate effect of the material, manufacturing process, process parameters and die feature size on ICR statistically; analysis of variance (ANOVA) tests were performed. Statistical significance of findings was presented in the next section along with ICR test results.

54

3.3. Results and Discussion

3.3.1. Dimensional Measurement Results

Average channel heights of manufactured BPPs were presented in Figure 3-16. All values represent average channel heights of three samples for each case. Increasing force in stamping and pressure in hydroforming processes resulted in increased channel heights. On the other hand, channel formability of bipolar plates was considerably less with respect to die channel geometry in use of both die with different channel heights.

Comparative profiles of channels obtained with contact type profiler (Ambios XP-1, Ambios Tech., CA, USA) were illustrated in Figure 3-17. The surface profile data obtained from profiler was analyzed with commercially available CAD software and channel tip radii were calculated as illustrated in Figure 3-18. Geometries of channel tips at both sides of the samples were point of interest as these sections were in contact with GDL and had significant effect on contact resistance values. It is observed that the channel radii for the plates formed with 250µm-die have significantly lower than with that of 750µm-die. BPP samples manufactured with 750 µm-die had more linear land area at channel valley (i.e. back side channel tip) and round section at the front side tip because of die design. However, upper and lower 250µm-dies had symmetric shape and resulted round tip at both side of the tip. BPPs stamped with 250µm-die had symmetric shape. Their tips measured and presented only for front side. On the other hand, hydroformed BPP samples in 250µm-die case had different geometry for front and back side; thus, their tip forms evaluated for both size.

Numerous studies have been conducted on optimum channel geometries in PEMFC from fuel distribution, water removal capability, operating conditions and manufacturing aspects. Kumar and Reddy, suggested in their studies that the optimum channel width, land width and

55

channel depth values as 1.5, 0.5 and 1.5 mm, respectively in order to maximize fuel consumption [129]. Scholta et al. investigated the effect of geometry on performance using computational fluid dynamics (CFD) software [130]. They reported that channel depth of more than 1.5 mm for a parallel flow field resulted in significant amount of unused oxygen; and a rib width of over 2 mm significantly decreased oxygen concentration across the rib. Experiments in their study showed that channel and rib widths between 0.7 and 1 mm were the optimum values. They also concluded that smaller channel dimensions were preferable for high current densities, whereas wider dimensions were better at low current densities. Cho and Mench experimentally investigated the effect of land to channel ratio and micro-porous structure of GDL on evaporative water removal properties [131]. They reported that land to channel ratio of greater than 0.52 was effective on minimum liquid saturation level of GDL and larger land to channel ratio increase the effective irreducible saturation due to the increase of immobile water under the land. Peng et al. took into account formability, in addition to reaction performance and they found that optimum dimension values for channel depth, channel width, rib width and transition radius are 0.5, 1.0, 1.6 and 0.5 mm, respectively [101]. The channel dimensions of BPP obtained by using 750 µm channel die in this study were found to be compatible with the abovementioned literature. Smaller feature size BPPs (formed by using 250 µm channel die) were included to the study to investigate effect of feature size on ICR.

56
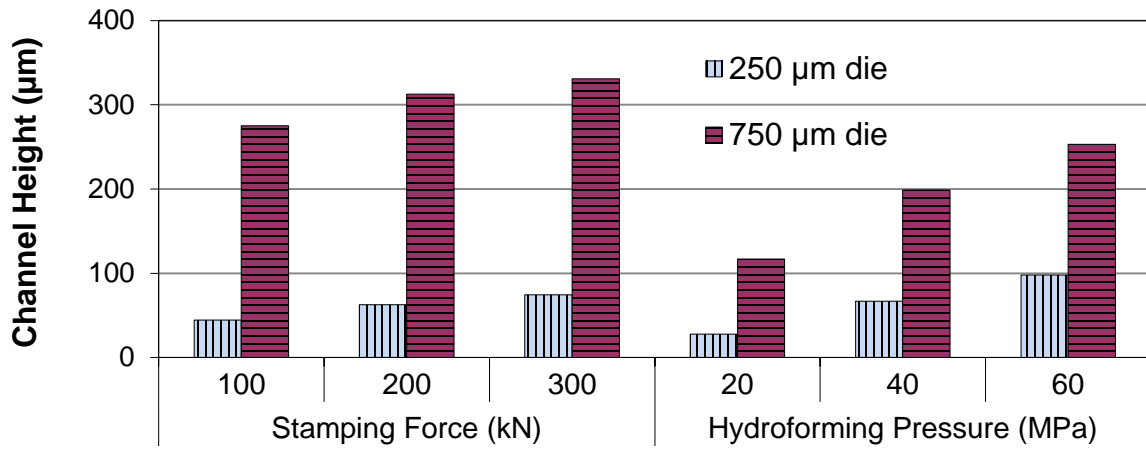
Figure 3-16 Average channel heights of BPP samples.
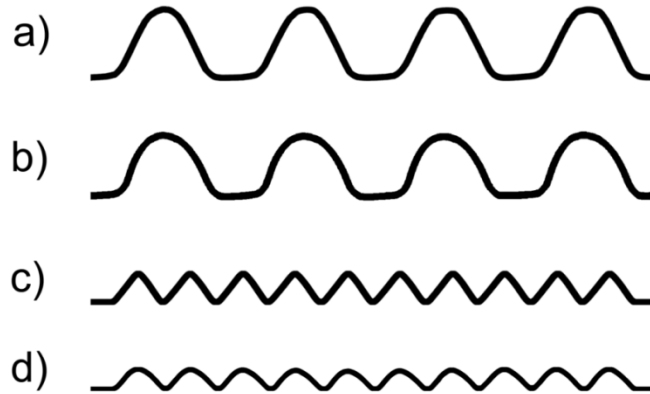
Figure 3-17 Representative channel profiles of formed BPP samples.(a) Stamped with 750 µm die, b)- Hydroformed with 750µm -die, c) Stamped with 250µm -die, d)-Hydroformed with 250µm -die.) (Height to width ratios are not to scale.)
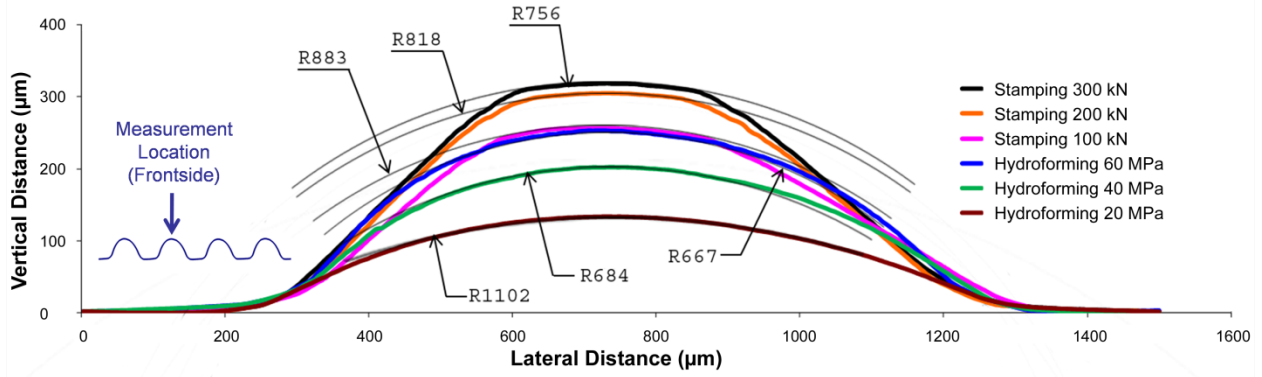
a)
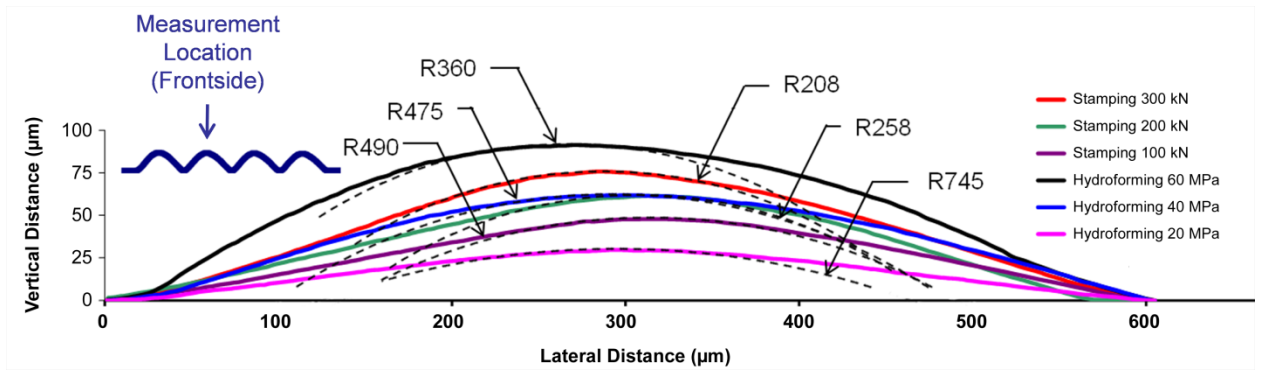
b)
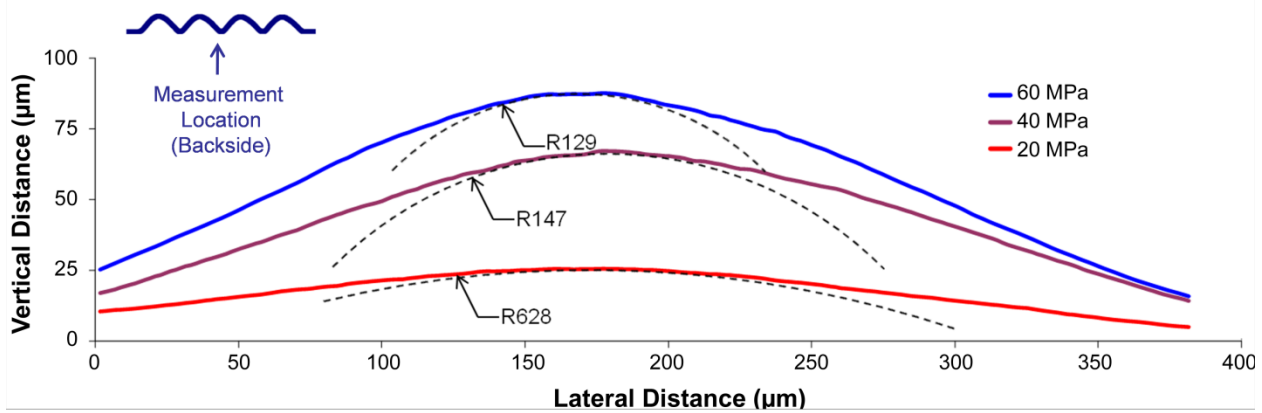
c)

Figure 3-18   Channel profiles and tip radii of manufactured BPP samples with (a) 750μm -die, (b) 250μm -die and c) 250μm -die (backside of hydroformed samples).

58

3.3.2. Surface Characterization Results

Surface morphology evolution of BPP due to forming process was portrayed in Figure 3-19. Also, surface roughness values of unformed blank samples and BPPs formed with various manufacturing conditions were reported in Figure 3-20. Roughness of uncoated blanks was almost one order of magnitude lower than that of formed samples while BPP samples with different forming parameters showed comparable values. Although forming process drastically increased roughness values, further strain (i.e. more stamping force or hydroforming pressure) slightly decreased roughness three out four cases as shown in Figure 3-20.

Surface roughening due to plastic forming can be induced by intrinsic and/or extrinsic effects. Microstructure dynamics of bulk plasticity induced intrinsic defects. On the other hand extrinsic defects are results of external effects such as mechanical contacts of tools and friction [183]. In the case of this study, roughening occurred mainly intrinsically yet die-sheet material contact occurred at the other side of channel tips. The most effective factors on roughening behavior were reported in literature as strain, grain size and texture whereas the roughness increase was irrespective of the stress state [189,190].

GDL structure was investigated by means of both SEM and non-contact 3D surface measurement system. In Figure 3-21, SEM images shows undamaged areas and damaged areas under excessive compaction force on GDL. This result was in a good agreement with the study by Matsuura et al. [93]. They used quite similar GDL (Toray TGP-H-090,280 µm thick) to GDL was used in this study (Toray TGP-H-060, 190 µm thick) and they concluded that compressive displacement more than 100 µm may damage GDL. Non-contact 3D surface measurements show effect of compression on GDL as shown in Figure 3-22. Carbon fibers came closer to each other and pore volume of the structure was decreased for compressed GDL

59
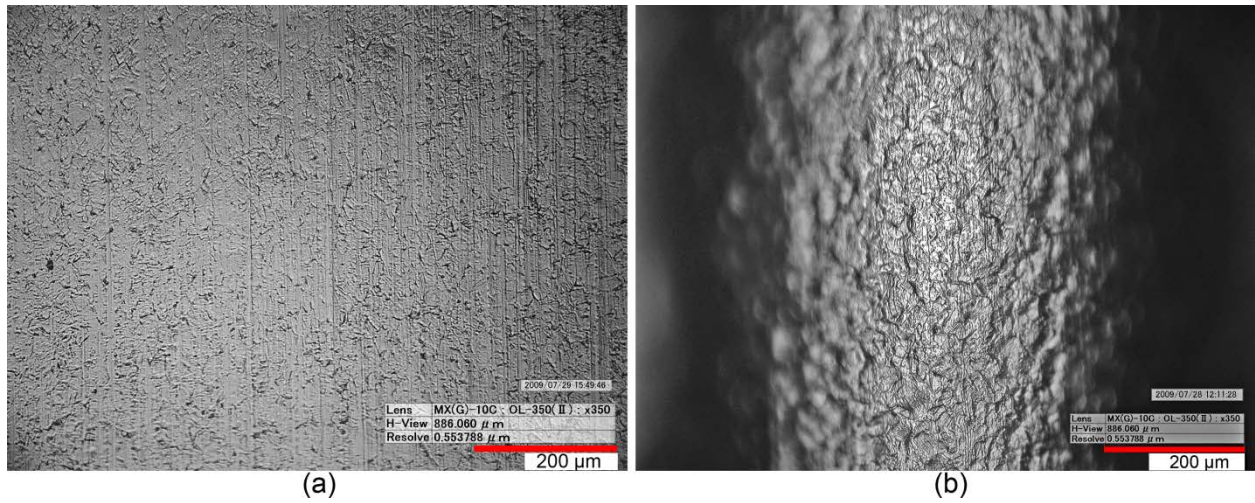
Figure 3-19 Optical images of a) unformed blank and b) channel tip of formed BPP.
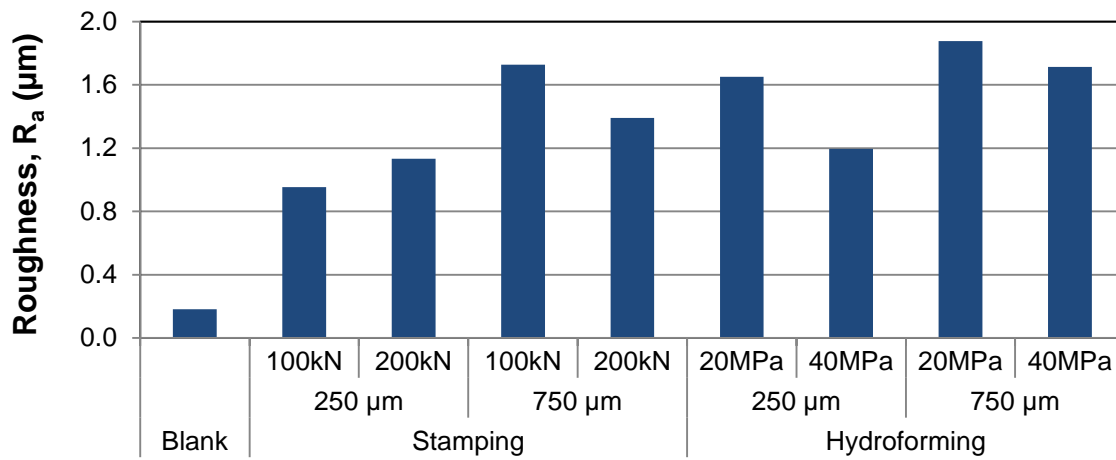
Figure 3-20 Surface roughness values of blank and some formed samples.
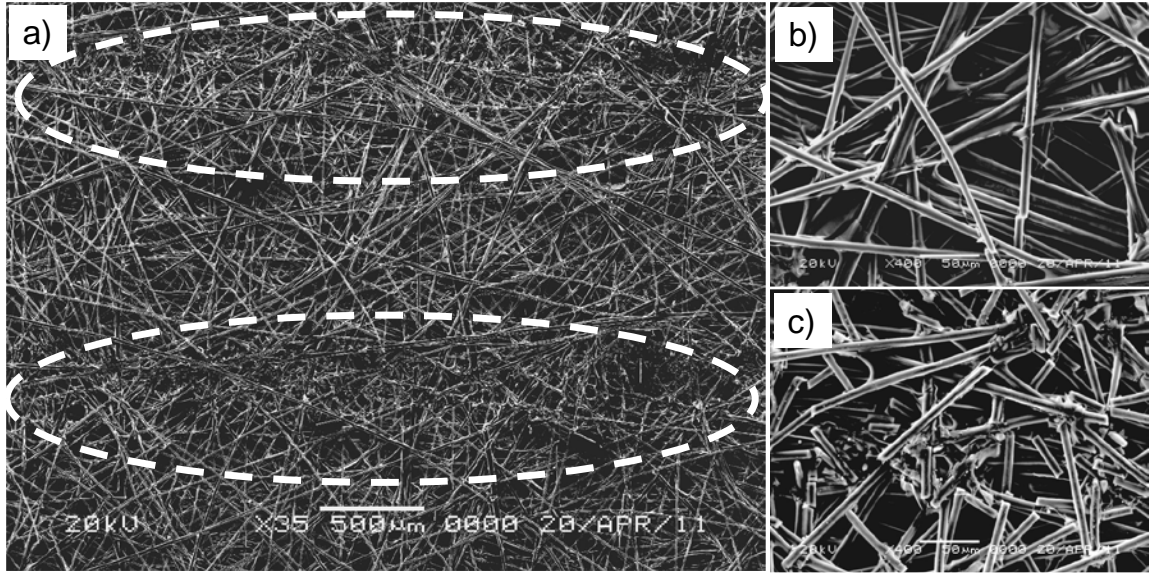
Figure 3-21 SEM images of the GDL. In picture a) white ellipses indicate damages on GDL due to excessive compression pressure. b) Non-damaged and, c) damaged area with high magnification.
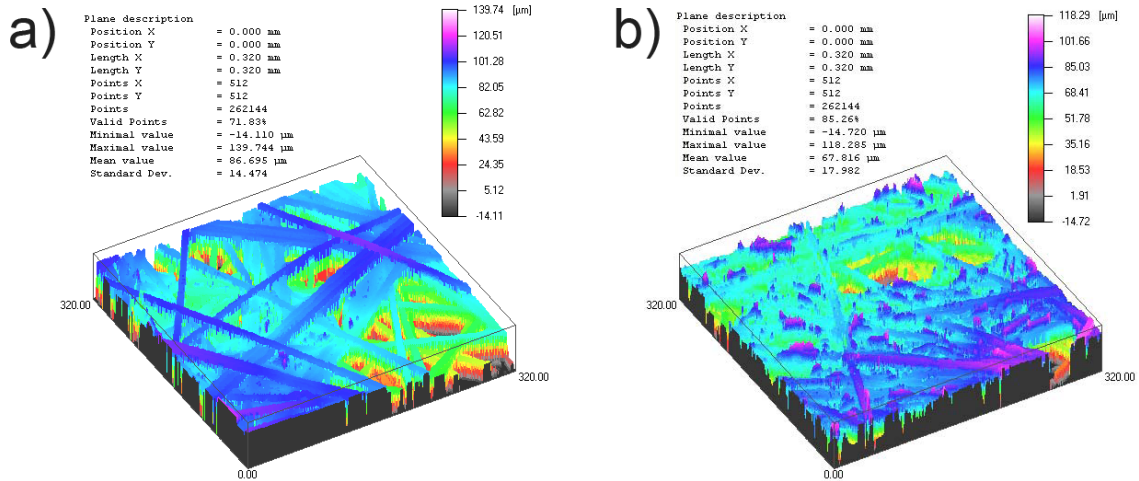
Figure 3-22 Non-contact 3D surface measurement system images of GDLs a) before b) after ICR test (taken by μsurf explorer at Nanofocus Inc., Glen Allen, VA, USA).

3.3.3. Contact Area Measurement Results with Pressure Sensitive Films

Contact areas between BPP and GDL with increasing compaction force were measured by using the procedure explained in Section 3.2.4. Figure 3-23 shows the results for stamped BPPs by using 750 µm-die and 200 kN stamping force. Contact areas increased with increasing compaction pressure due to deformation of GDL and BPP. Initial rapid increase of contact area became stabilized increase by compaction force most likely because of compaction of fibers in GDL. Area specific contact resistances of the formed BPP given in next sections were calculated based on this data.
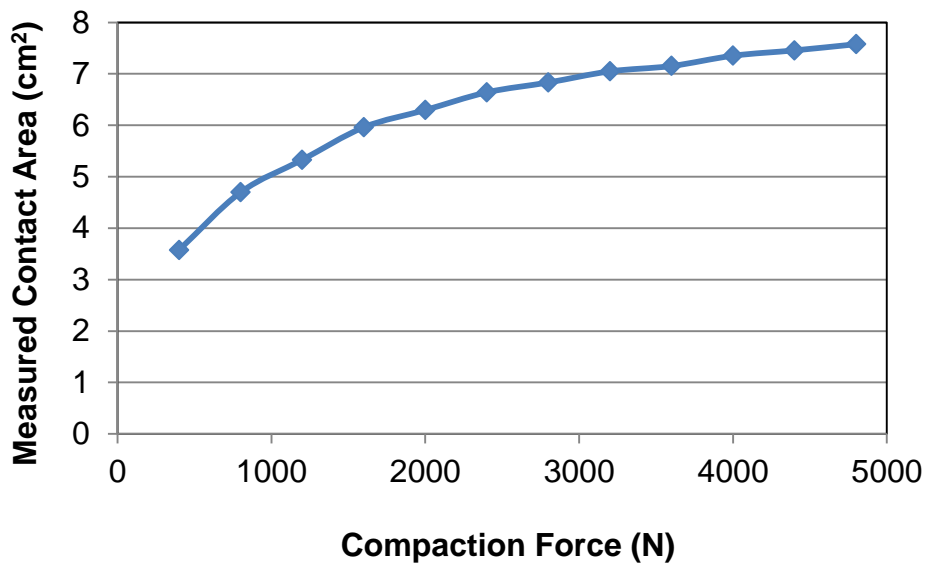
Figure 3-23 Contact area change by compaction pressure for BPP formed with 750 µm die.

3.3.4. Contact Area Calculation results with FEA Modeling

Simulation results for hydroformed and stamped BPPs with 250 µm channels were presented in Figure 3-24 and Figure 3-25, respectively. Contact areas between GDLs and BPPs for these cases were depicted in Figure 3-26. Similarly, Figure 3-27 and Figure 3-28 represent

www.manaraa.com

simulation results for 750 µm channel hydroformed and stamped BPPs, and Figure 3-29 shows calculated contact areas for these cases. In 250 µm channel cases, contact areas strongly depended on hydroforming pressure or stamping pressure. Increasing hydroforming pressure or stamping force in forming processes reduced contact areas in ICR test significantly. Contact area reduced from 15.9 to 6.7 cm^2 for increasing hydroforming pressure from 20 to 60 MPa in hydroforming, and contact area reduced from 12.8 to 7.9 cm^{2}for with increasing stamping force from 100 to 300 kN in stamping. However, in 750 µm case contact area stayed between 6.4 and 8.5 cm^2 for all hydroforming pressures and stamping forces. Especially in stamping, almost no correlation was observed between stamping force and contact area. Contact area differences between two different channel sizes can mainly be attributed to size effect. While thickness of GDL was the same for both (250 and 750 µm channels) cases, cross-section of BPPs was changed by almost three folds. Another reason for contact area differences between hydroforming and stamping could be different deformation patterns. In hydroforming, channels form freely under the effect of pressure while channel tips mainly conform to tips on the dies in stamping. Increasing hydroforming pressure produced smaller radii at the contact tips of the samples.

63
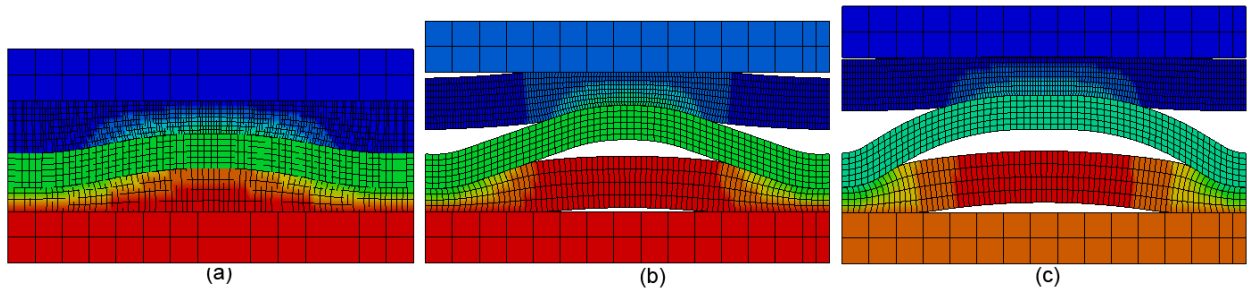
Figure 3-24 FEA results of ICR test for BPPs formed by using a) 20, b) 40 and c) 60 MPa hydroforming pressures with 250 µm-channel die.
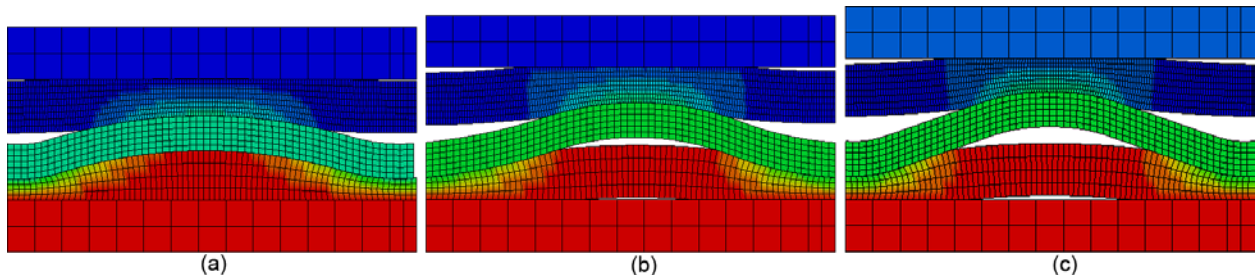
Figure 3-25 FEA results of ICR test for BPPs formed by using a) 100, b) 200 and c) 300 kN stamping force with 250 µm-channel die.
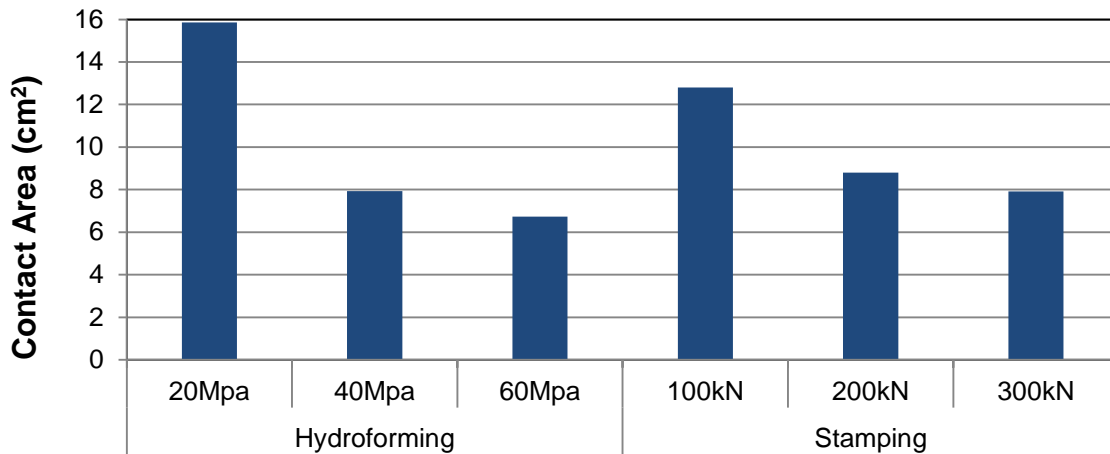
Figure 3-26 Average contact area between GDLs and BPPs formed with 250 µm-channel die.
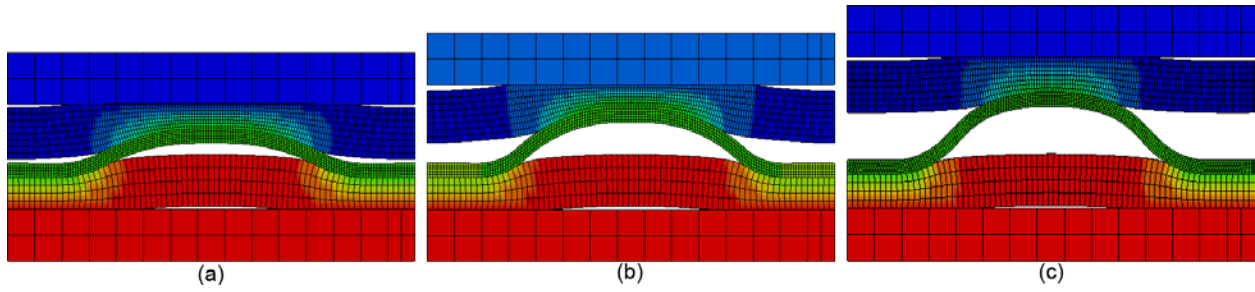
Figure 3-27 FEA results of ICR test for BPPs formed by using a) 20, b) 40 and c) 60 MPa hydroforming pressures with 750 μm-channel die.
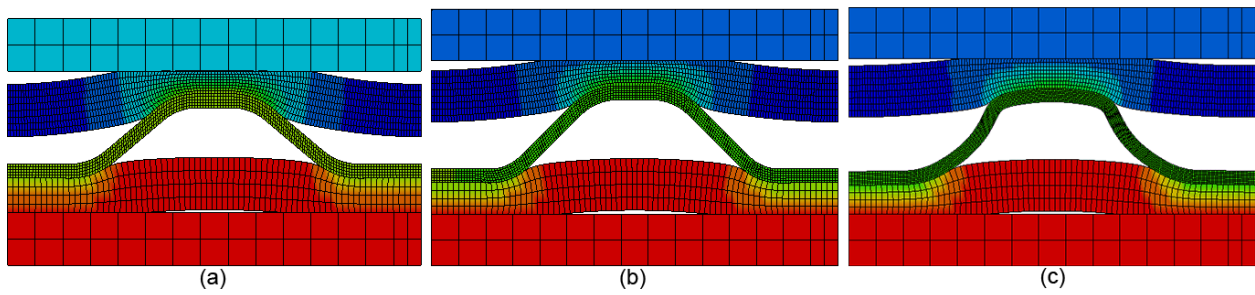
Figure 3-28 FEA results of ICR test for BPPs formed by using a) 100, b) 200 and c) 300 kN stamping force with 250 μm-channel die.
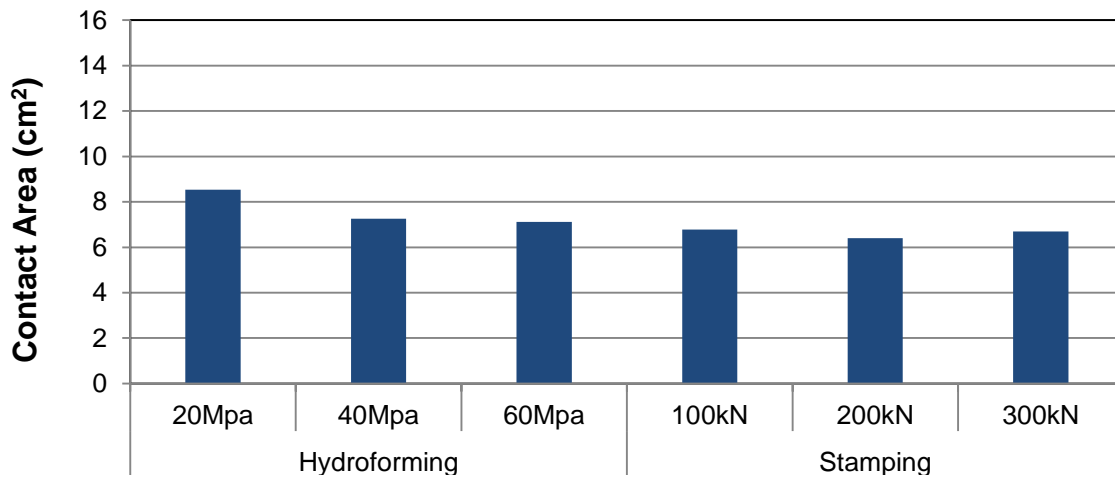
Figure 3-29 Average contact area between GDLs and BPPs formed with 750 μm-channel die.

3.3.5. Contact Resistance Measurements

Area specific contact resistance (ASR) evolution by compressive force between SS 304 and SS 316L blank samples and carbon paper GDL (Toray TGP-H 60, Toray Corp., Tokyo, Japan) were presented in Figure 3-30. Total contact resistance by compaction force for some representative BPP samples was presented in Figure 3-31. ASRs were compared in Figure 3-32 for a stamped, hydroformed and blank sample of SS316L. ASRs for formed BPP samples were calculated as explained in Section 3.2.4. and only common pressure intervals for formed and unformed samples were included in the Figure 3-32. As expected, an exponential decrease in ICR was observed with increasing compaction force due to increasing real contact area between GDL and BPP surfaces. Bar graphs were used to compare ICR values of different samples at 2240 N compaction force, corresponding 140 N/cm^2 compaction pressure for 16 cm^2 active areas of BPP samples used in this study in next sections.
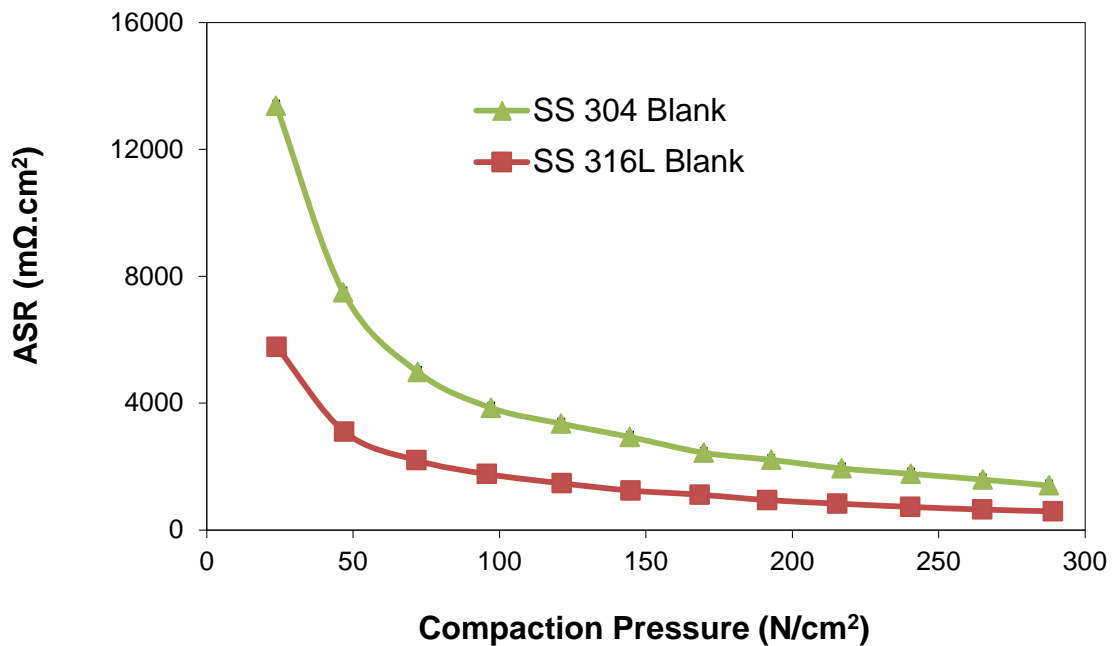
Figure 3-30 Area specific contact resistance with compaction pressure for blank samples.

66
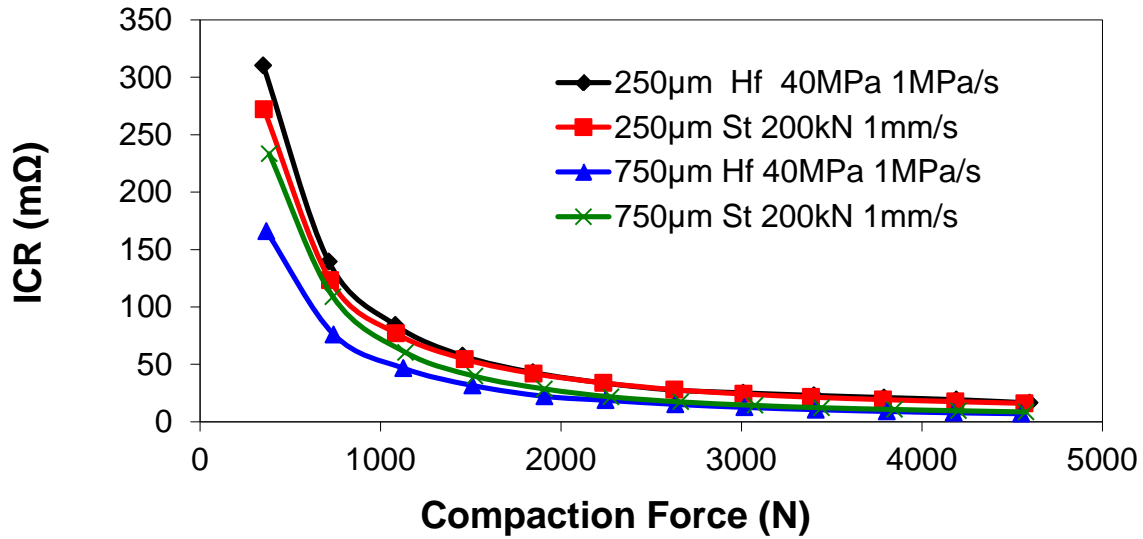
Figure 3-31 Variation of contact resistance with compaction force.
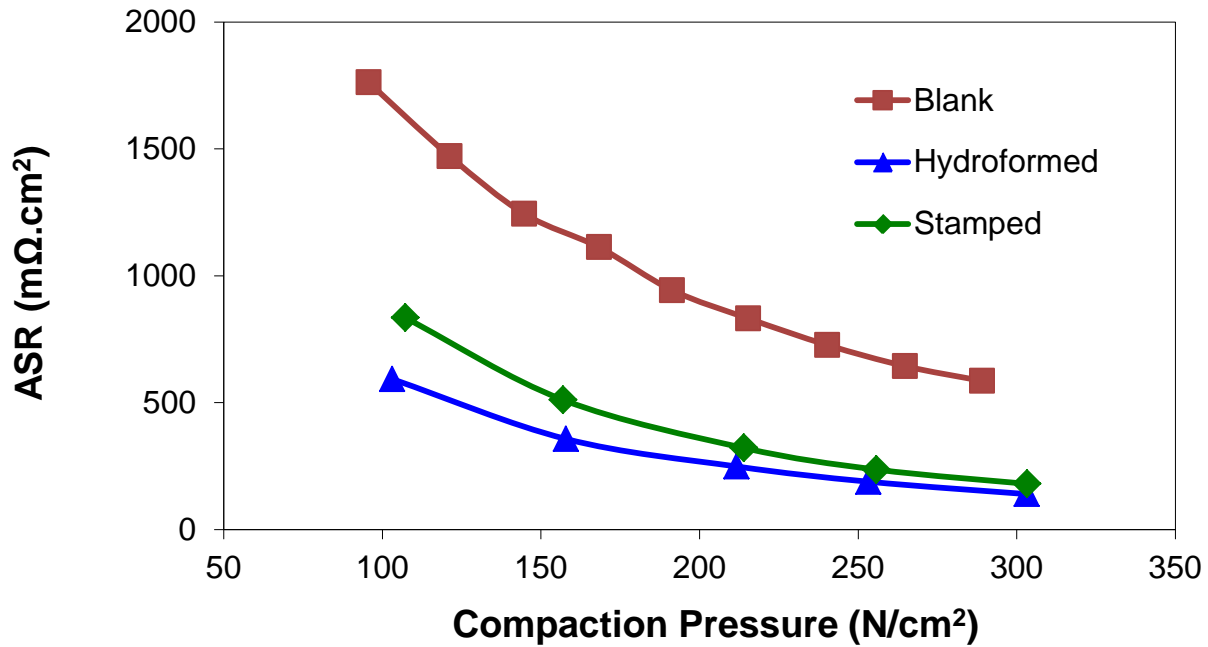
Figure 3-32 Area specific contact resistance of SS 316L blank, hydroformed and stamped samples. (200kN and 1mm/s for stamping; 40MPa and 1MPa/s for hydroforming and 750µm-die for both)

67

3.3.6. Effect of BPP materials

Two BPP materials, namely SS 316L and SS 304, were compared in terms of ICR values. It was observed that SS 304 showed lower ICR (average of 17.4 mΩ) compared to SS 316L (average of 21.25 mΩ) in each case of stamped samples. ANOVA test confirmed that ICR value differences in stamping were statistically significant (p=0 for α =0.05). However, in hydroforming, effect of these two BPP materials on ICR was found statistically insignificant (p=0.285 for α=0.05) for average values of 20.94 mΩ in SS304 and 19.31 mΩ in SS316L. In literature, better corrosion resistance was reported for SS 316L [23,59]. Therefore, the experiments in next steps were performed only with SS 316L material.

3.3.7. Effect of Process and Process Parameters

As depicted in Figure 3-33a, stamped BPPs exhibited higher ICR values (mean value of 21.25 mΩ) than that of hydroformed BPPs (mean value of 18.38 mΩ) for the channel geometry of 750 µm channel die (p=0 for α=0.05). In this case, process parameters such as stamping force and speed; hydroforming pressure and pressure rate, did not significantly affect the resultant ICR values. However, for the channel geometry of 250 µm channel-die case, notably decreasing ICR (from 56.63 to 29.31 mΩ) values were observed with increasing hydroforming pressure (from 20 to 60 MPa) in hydroforming (Figure 3-33b) while various pressure rate in hydroforming as well as stamping force and punch speed in stamping process resulted in insignificant differences for ICR values. This discrepancy can be attributed to different deformation patterns for stamping and hydroforming. In stamping, channel tips mainly conform to tips on the dies while upside channels form freely under the effect of pressure in hydroforming (Figure 3-17). Increasing hydroforming pressure produced smaller radii at the contact tips of the samples (Figure 3-18).

68

According to Hertzian Contact Theory, smaller contact radius provides higher contact stress on contact area of BBP and GDL. Therefore, this increased contact stress and possible deeper penetration of BPP contact tips toward GDL provided by smaller contact radii may explain reduced ICR with increasing hydroforming pressure. Decreasing trend of ICR and BPP channel tip radii with increasing stamping force and hydroforming pressure can easily be observed in Figure 3-34. However, all the ICR values obtained were much higher than desired goal set by DOE.

Due to the numerous approaches of measuring the ICR various experimental conditions, inconsistent values of ICR of given material have been reported in literature [3]. Most literature studies presented ICR values for flat coupons whereas focus was on formed BPP samples in present study. Also researchers involved surface modification before conducting ICR test while any surface preparation, other than cleaning, were not employed this study. In the light of these differences, ICR values of the present study for unformed samples were higher than ICR values reported in literature as presented Table 3-3.

69

Table 3-3 Some ICR values reported on SS304, SS316 and SS316L.

Material	ICR ($m\Omega$-cm^2)	Compaction Pressure (N/cm^2)	Before/After Corrosion	Reference
SS 304	51	220	Before	[65]
SS 304	140	140	Before	[26]
SS 316	37	220	Before	[65]
SS 316	44	220	After	[65]
SS 316	200	140	Before	[14]
SS 316	320	140	After	[14]
SS 316L	160	140	Before	[22]
SS 304	2929	140	After	This study
SS 304	232	140	After	This study
SS 316L	1244	140	Before	This study
SS 316L	238	140	After	This study

3.3.8. Effect of Die Feature Size

BPPs formed with two different channel geometries were compared to investigate the size effect on contact resistance behavior. The first group of BPP samples was manufactured with a die set which had 750 µm-die channel height and 1500 µm channel pitch whereas in the second group, a geometry of 250 µm channel height and 605 µm channel pitch were chosen for the die set to produce the BBP samples as given in Figure 3-1. BPP samples formed with 250 µm channel die resulted in higher contact resistance (min. 27.56 mΩ; max. 56.63 mΩ) than that of 750 µm channel (min. 17.75 mΩ; max. 22.44 mΩ) die for both hydroforming and stamping process. There were 26 and 65 channels on BPP plates samples manufactured with 750µm-die and 250µm-die, respectively. It is assumed that total clamping force distributed among the channels uniformly. Therefore, BPP plates manufactured with 750µm -die had more contact force on each channel tips compared to that of BPP samples manufactured with 250µm-die. ICR discrepancy between two different samples can be explained by the force difference on the individual channels. Increasing hydroforming pressure had lowered the ICR where 250µm-die

70

used. In contrast, any significant ICR trend was not registered by changing manufacturing parameters in stamping of both cases, and also for hydroforming of 750µm-die case. ASR graphs by compaction pressure based on calculated areas confirm this explanation as shown in Figure 3-35Figure 3-36. These findings indicate that BBP feature size has significant effect on ICR due to the fact that it directly alters the contact area.
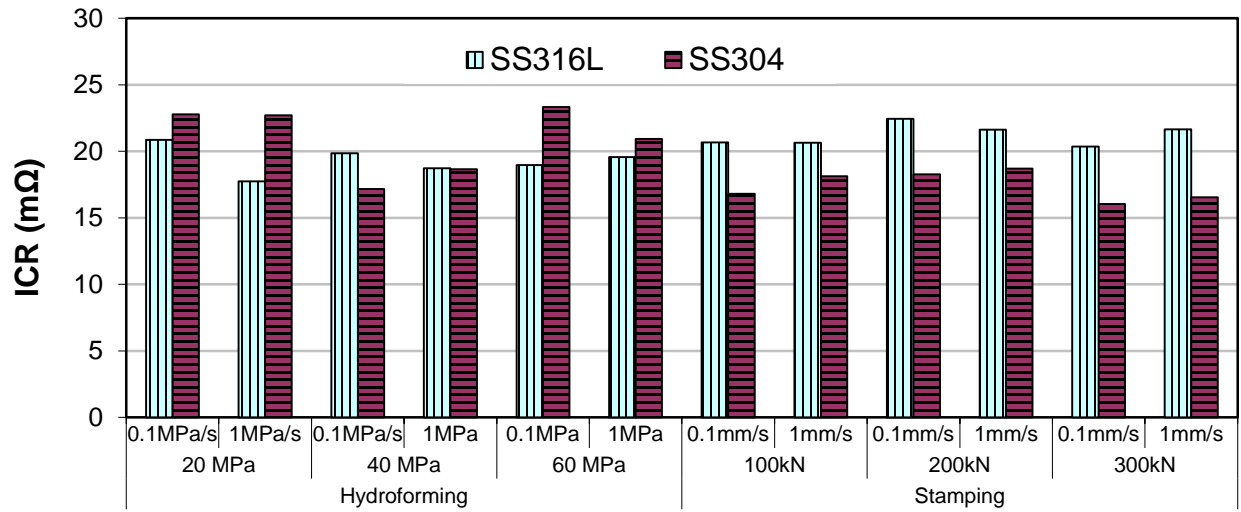
a)
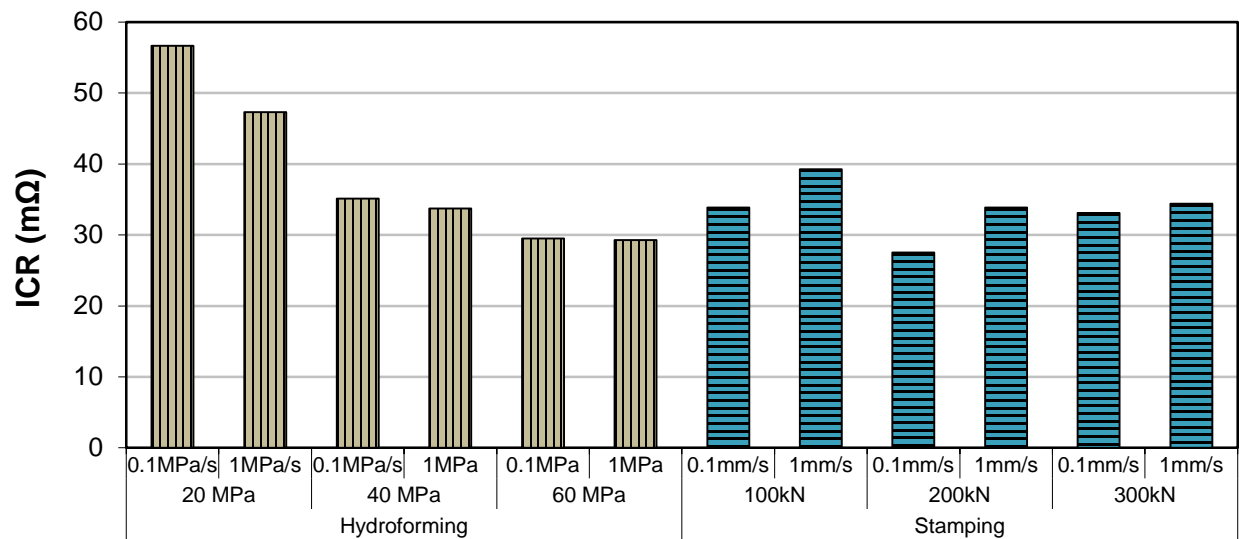
b)

Figure 3-33 Interfacial contact resistance values at 2240 N compaction force for BBP samples manufactured with (a) 750µm-die and (b) 250-µm-die.
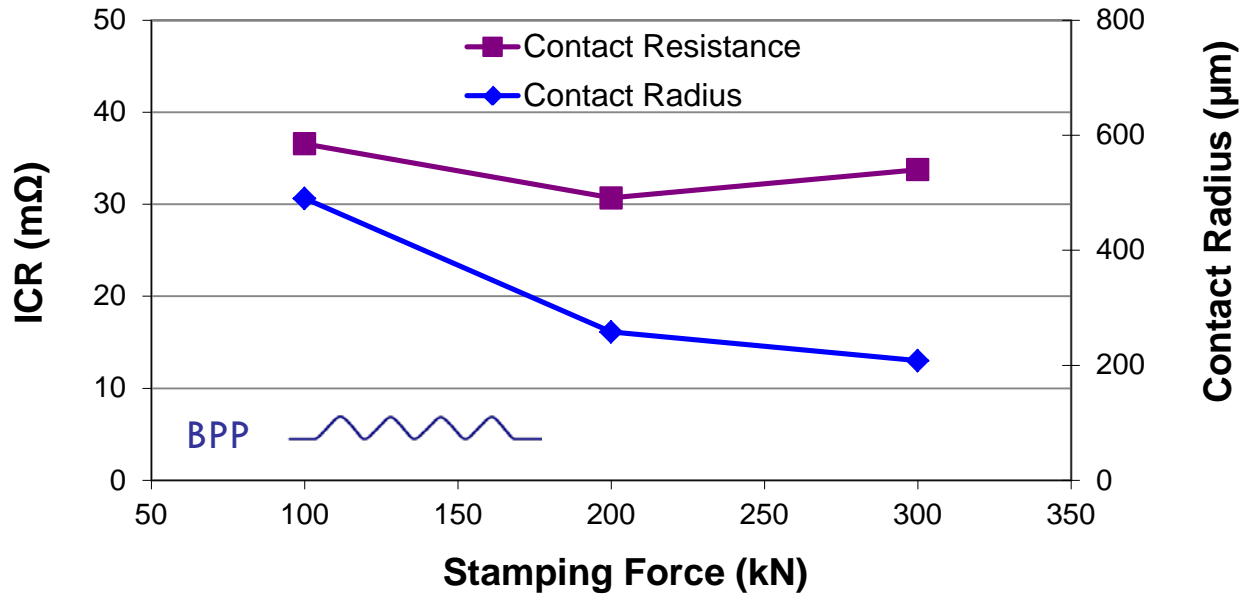
a)
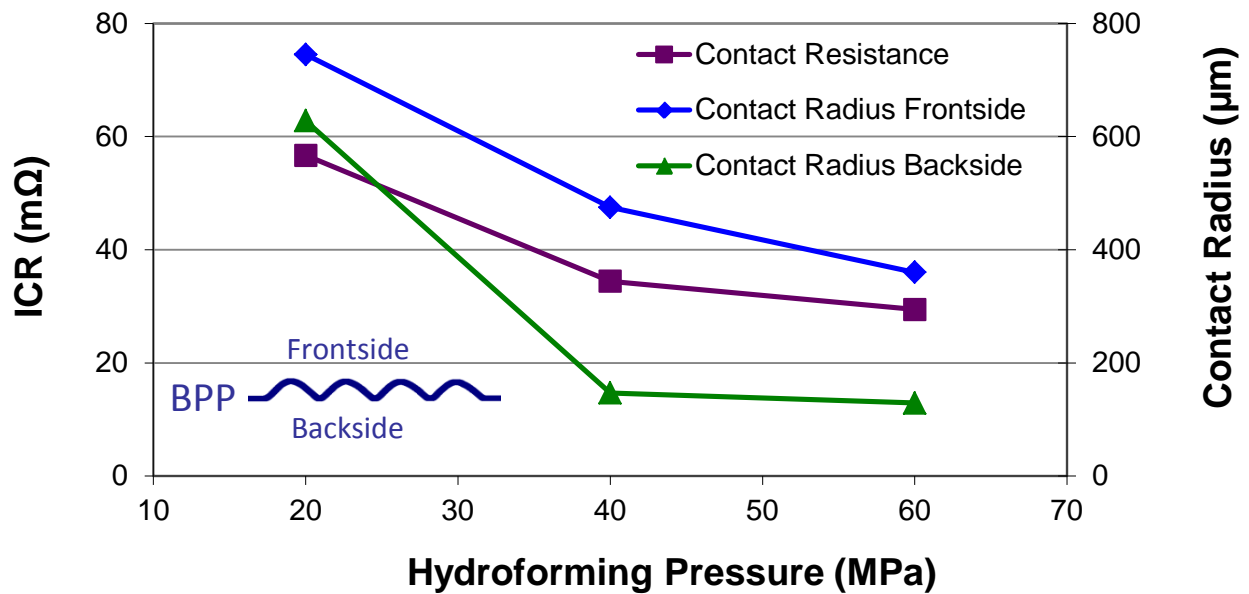
b)

Figure 3-34 Variations of ICR with channel tip radii (a) stamped (b) hydroformed BPP samples (250μm -die).

73
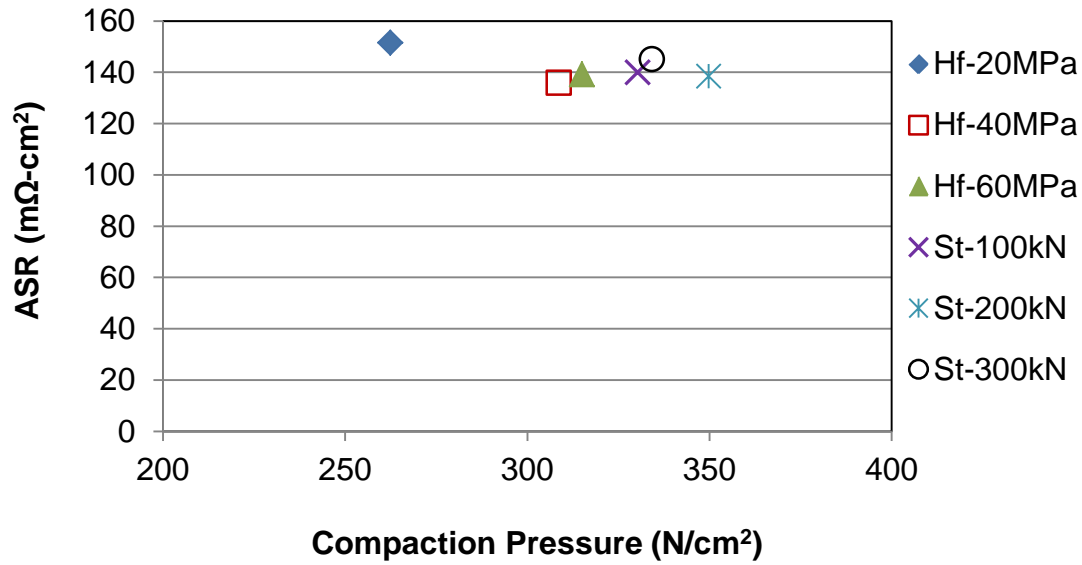
Figure 3-35 ASR of SS 316L BBP with 750 μm channels by compaction pressure (Contact areas were calculated by FEA model).
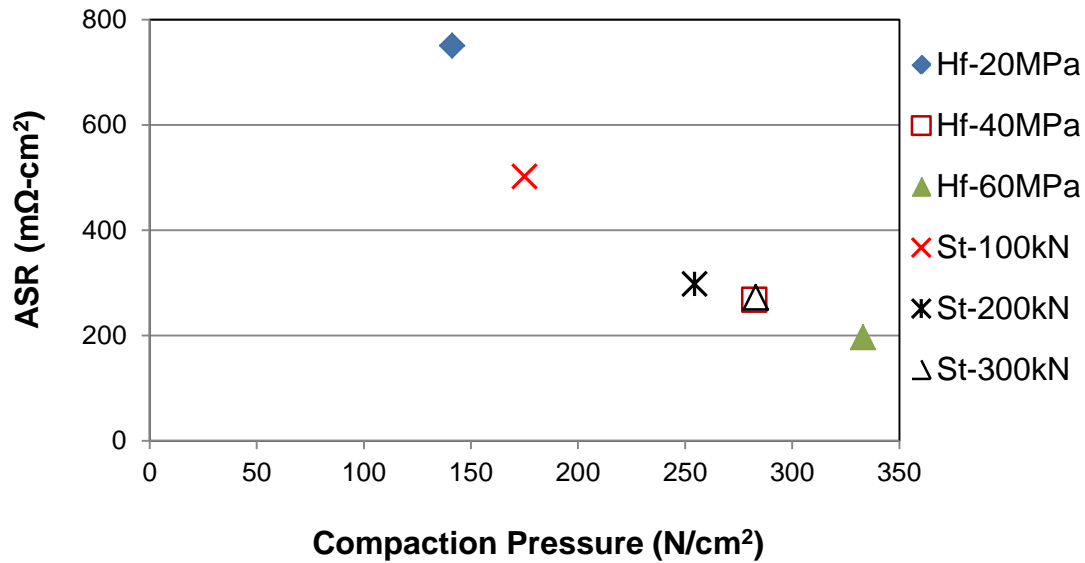
Figure 3-36 ASR of SS 316L BBP with 250 μm channels by compaction pressure (Contact areas were calculated by using FEA model).

74

3.3.9. Effect of Roughness on Contact resistance

Relationship between the ICR and the roughness of SS 316L blank and BPPs were investigated. As shown in Figure 3-37 increasing roughness decreased ICR in general. This result agreed the study by Kraytsberg et al. They showed that the surface roughness significantly affects the ICR [66]. The rougher surface showed lower ICR value than the finer one due to the difference in the real contact area between GDL and BPP.
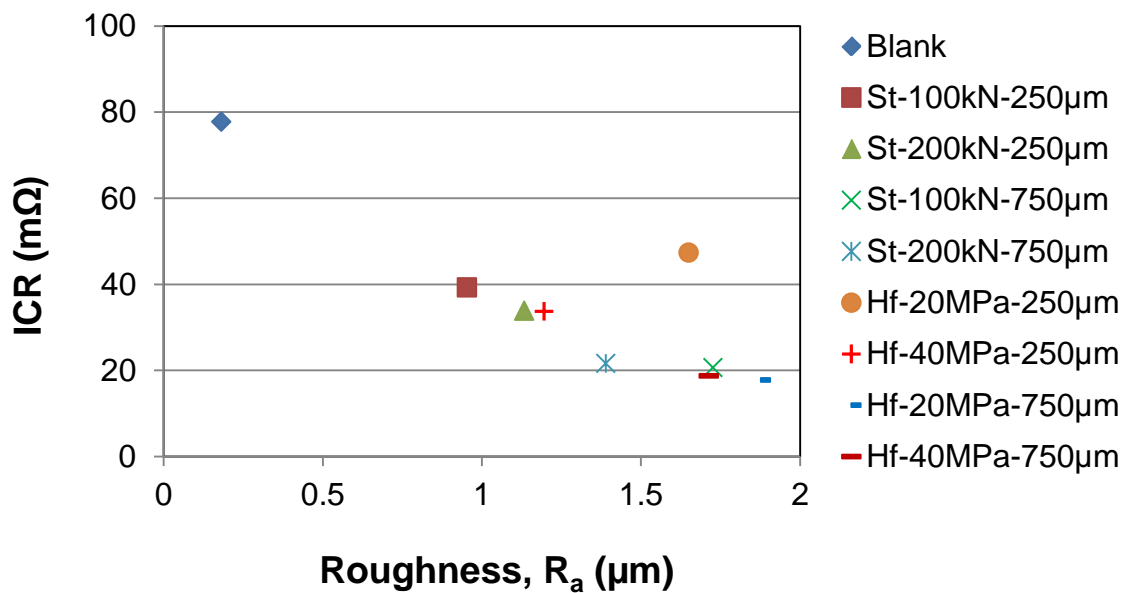
Figure 3-37 Comparison of ICR and roughness for SS316 blank and various BPPs.

3.3.10.   Effect of Corrosion on the ICR

BPP samples previously subjected corrosion tests and uncorroded BPP samples were tested to measure their ICR values and results were summarized in Table 3-4 and Table 3-5. In general, corroded BPPs yielded lower ICR values than the uncorroded BPPs.   However, any systematic tendency was not observed for the samples tested with different corrosion tests.   Most of the

studies in the literature investigated polished samples, and reported increasing ICR with increasing corrosion test duration. However, Andre examined the evolution of the ICR with aging time in a synthetic fuel cell (resting conditions) environment and they registered similar behavior with the present study [132].

Table 3-4 Effect of corrosion test on ICR for hydroformed SS 304 BPP samples (750µm-die).

Manufacturing Conditions							
Hydroforming Pressure (MPa)		20		40		60	
Pressure Rate (MPa/s)		0.1	1.0	0.1	1.0	0.1	1.0
ICR at 2240 N (mΩ)	Uncorroded	23	23	17	19	23	21
	Corroded in PDH[a]	8	11	5	9	10	10
	Corroded in PDO[b]	7	5	12	10	14	7
	Corroded in PSH[c]	N/A	11	N/A	6	N/A	12
	Corroded in PSO[d]	N/A	12	N/A	5	N/A	N/A

a: Potentiodynamic test with H2 bubbling during 40 minutes.
b: Potentiodynamic test with O_2 bubbling during 40 minutes.
c: Potentiostatic test with H_2 bubbling during 3 hours.
d: Potentiostatic test with O_2 bubbling during 3 hours.

Table 3-5 Effect of corrosion test on ICR for hydroformed SS316L BPP samples (750µm-die).

Manufacturing Conditions							
Stamping Force (kN)		100		200		300	
Punch Speed (mm/s)		0.1	1.0	0.1	0.1	0.1	1.0
ICR at 2240 N (mΩ)	Uncorroded	21	21	22	22	20	22
	Corroded in PDH[a]	10	6	7	5	3	6
	Corroded in PDO[b]	7	N/A	5	7	N/A	8
	Corroded in PSH[c]	N/A	8	N/A	3	8	8
	Corroded in PSO[d]	N/A	8	N/A	9	N/A	7

a: Potentiodynamic test with H_2 bubbling during 40 minutes.
b: Potentiodynamic test with O_2 bubbling during 40 minutes.
c: Potentiostatic test with H_2 bubbling during 3 hours.
d: Potentiostatic test with O_2 bubbling during 3 hours.

76

3.4.Summary and Conclusions

Stainless steel BPP samples were manufactured with two different processes, namely stamping and hydroforming, under various process conditions, and then were subjected ICR tests. In general, stamped BPP samples demonstrated higher conductivity (i.e. low ICR) than the hydroformed BPP samples. It is concluded that manufacturing methods and their parameters are significantly effective on ICR performance of metallic BPP since they determine the geometry and surface condition of BPPs which is effective on ICR. Increasing maximum pressure levels in hydroforming resulted in decreasing ICR values. In addition, BPP samples produced with larger channel size die (750µm-die) exhibited lower ICR than the BPPs with smaller channel size (250µm-die). It is verified that the geometry of the forming dies are also effective in ICR values. Short term electrochemical corrosion tests decreased ICR values of the BPP samples. Nevertheless, all ICR values registered during experiments were distinctly higher than DOE target. Thus, it can be concluded that properly chosen coatings on stainless steel alloys are necessary to meet the ICR performance target as noted by several other researchers. Upcoming study by authors will investigate the effect of manufacturing process on coated BPP samples with different coating types and thickness on the ICR of BPP.

CHAPTER 4: Contact Resistance Characteristics of Coated Metallic Bipolar Plates for PEM Fuel Cells- Investigations on the Effect of Manufacturing [1]

This chapter aimed for understanding the effects of hard coatings used in bipolar plates (BPP) on the contact resistance characteristics of BPP. To this goal, 51 µm-thick SS316L stainless steel sheet blanks were formed into BPPs using two forming techniques (stamping and hydroforming); then formed plates were coated with three different PVD coatings (CrN, TiN, ZrN) at three different coating thicknesses (0.1, 0.5 and 1µm). Contact resistance of the formed and coated BPP samples were measured before and after those were exposed to the polymer electrolyte membrane fuel cells (PEMFC) operating conditions. Interfacial contact resistance (ICR) tests indicated that CrN coating increased the contact resistance of the samples, unexpectedly. TiN samples showed the best performance in terms of low ICR; however, their ICR dramatically increased after short term exposure to corrosion. ZrN coating also improved conductivity of the SS316L BPP samples and those demonstrated similar ICR performance before and after corrosion exposure.

---

[1] The contents of this chapter are under review for publication in International Journal of Hydrogen Energy with manuscript number of HE-D-11-03241.

4.1. Introduction

In Chapter 3, effect of these two manufacturing methods on ICR of uncoated metallic BPPs was investigated [133]. It was concluded that manufacturing process, process conditions and die geometry affect the ICR to different extents. Moreover, contact resistance of uncoated BPP did not satisfy ICR targets, hence properly chosen or developed coatings on stainless steel alloys are needed to improve ICR performance. The objective of this part of the study was set to investigate and reveal the possible effect of these two manufacturing processes on the contact resistance behavior of coated and formed stainless steel BPPs.

79

4.2. Experimental Methodology and Conditions

4.2.1. Manufacturing and Coating of Bipolar Plates

SS 316L bipolar plate samples with three different PVD metal nitride coatings, namely titanium nitride (TiN), chromium nitride (CrN), zirconium nitride (ZrN), at three different coating thicknesses, 0.1, 0.5 and 1 μm, were tested and compared in terms of their ICR. To begin with, BPP samples were shaped into micro-channels using both stamping and hydroforming. Formed plates, then, were outsourced for PVD coating (Tanury Industries Co., Lincoln, RI). Lastly, ICR tests were conducted on formed and coated BPPs as well as unformed blanks with similar coatings. Three samples were used in each case to address the repeatability of test results.

In forming of bipolar plates using hydroforming and stamping processes, pre-determined process parameters from previous studies were 40 MPa hydroforming pressure with 1 MPa/s rate in hydroforming, and 200 kN stamping force with 1 mm/s punch speed [32,133]. Necessary sheet sizes for forming process were 70x70 mm in stamping and 150x150 mm in hydroforming while formed (micro-channeled) areas were limited to 40x40 mm in both processes. Two different die geometries with micro-channel dimensions of 250 and 750 µm in height were used in both forming methods to investigate effect of feature size. Some of the formed BPPs are shown in Figure 4-1. Detailed description of the forming processes benefited was presented at Chapter 3 and also can be found elsewhere in literature [60,133].

PVD coating process parameters are listed in Table 1. Detailed information on the coating process can be found in a study by Yoon et al. [90]. Surface roughness of the samples was measured by using Wyko NT1100 optical profiler (Veeco Instruments Inc., Tucson, AZ, USA). Surface morphology and cross-sections of coated samples were investigated by using Hitachi

SU-70 scanning electron microscope (SEM) equipped with EDAX energy dispersive X-ray spectroscopy system (EDX).

4.2.2. Interfacial Contact Resistance (ICR) Tests

Contact resistance of BPPs was measured by a method established by Wang [28]. Test setup and detailed procedure was explained in Section 3.2.5. Three specimens were tested for each case to monitor the repeatability of the tests. Uncoated samples were subjected to ultrasonic cleaning for 30 minutes in acetone bath while coated ones were tested as received. To reveal the effect of PEMFC corrosive conditions on ICR of BPP samples, ICR tests were conducted before and after corrosion tests.

In contact resistance calculation, real contact areas of BPP samples were measured by using pressure sensitive film (Pressurex Super Low, Sensor Products, NJ, USA). As explained in Section 3.2.4., films were placed between BPP and GDL at the both sides of BPP. As the sandwiched BPP is compressed, the peaks of micro-channels were imprinted on films. These imprints then were analyzed by using Image J software to calculate real contact areas on films [125].

4.2.3. Exposing BPPs to corrosive conditions

To disclose the effect of the PEMFC operating conditions on ICR, BPP samples were subjected to corrosion tests first. Potentiodynamic electrochemical corrosion test were employed in 0.5 M H_2SO_4 solution as the working electrolyte at 80°C with oxygen bubbling to simulate cathodic conditions of PEMFC. Potential range was changed between -1.2 V and 0.8 V with

81

respect to standard hydrogen electrode (SHE) at a rate of 1 mV/s. Detailed explanation of the

corrosion test applied and their results can be found in earlier works [59,134].

Table 4-1 Chemical composition of SS316L (Browns Metals Co., Rancho Cucamonga, CA, USA).

C	Mn	P	S	Si	Cr	Ni	Mo	Cu	N	Fe
0.021	1.48	0.033	0.001	0.43	16.20	10.03	2.06	0.43	0.04	Bal

Table 4-2 Coating conditions (provided by Tanury Industries).

Run#	Coating	Thickness	Temperature	Deposition Time	Deposition Current	Bias Voltage	Nitrogen flow rate	Argon flow rate	Pressure
		(μm)	*(°C)*	*(mins)*	*(A)*	*(V)*	*(sccm)*	*(sccm)*	*(m Torr)*
1	TiN	0.1	60	6	450	75	500	800	5
2	TiN	0.5	60	38	450	75	500	800	5
3	TiN	1	60	75	450	75	500	800	5
4	CrN	0.1	60	2	450	75	500	800	5
5	CrN	0.5	60	4	450	75	500	800	5
6	CrN	1	60	8	450	75	500	800	5
7	ZrN	0.1	60	2	450	75	500	800	5
8	ZrN	0.5	60	8	450	75	500	800	5
9	ZrN	1	60	16	450	75	500	800	5

4.3.   Results

Effect of certain process parameters such as coating type, thickness, as well as corrosion

exposure on both blank and formed BPP samples will be reviewed in detail in following sub-

sections.

4.3.1. Appearance, SEM and EDX Investigation Results

Examples of "formed and coated BPP samples" used in this study are presented in Figure 4-1. BPP samples with 1 and 0.5 µm coating thickness showed very similar color while 0.1 µm thick coated samples exhibited slightly lighter color compared to their thicker counterparts. Colors of the BPP samples correspond their respective stoichiometric colors as reported in the literature as TiN coated samples with golden, CrN coated samples with silver-gray and ZrN coated samples with light-yellow colors were observed. Colors of reactively deposited coatings depend on stoichiometry [107,135-143]. Cheng at al. reported that only stoichiometric TiN exhibited golden color while lower N leaded light-yellow [107]. In addition, Johansson et al. revealed reddish-brown for TiN as amount of N was increased [138]. Benia et al., Liu and Yang, and Carvalho et al. observed metallic-gray for low N ZrN, semi-transparent brownish for high N flows and golden-yellow for stoichiometric ZrN compound [136,142,143].

Polished cross-sections of the 1 µm thick TiN coated samples are shown in Figure 4-2. Surface morphology of BPP samples appears in Figure 4-3. Pin holes (black dots in the pictures) and macro-defects (as white dots) with various densities can be seen on the all samples. It was observed that CrN coated plates have less number of pinholes and macro-defects while relatively higher number of these defects were available on TiN coated samples. Dimensions and number of defects increase with increasing coating thicknesses. Many studies showed that although reducing amount of pinholes and macro-defects is possible, totally eliminating them almost impossible in PVD coating techniques [144,145].

EDX analysis was also conducted on coated samples to obtain elemental information on different regions of the samples. Figure 4-4 shows the comparison of regular smooth areas to a macro-defect and a pitting zone for 1 µm-thick ZrN coated sample. Similar comparison is

shown in Figure 4-5 for 1 µm-thick TiN coated sample. EDX analyses on macro-defects (Figure 4-4.b and Figure 4-5.c) confirmed the high concentration of coating metals (Zr or Ti) while measurements on pinhole or pitting zones (Figure 4-4.c, Figure 4-5.b) yielded lower percentage coating material compared to regular area, as expected.
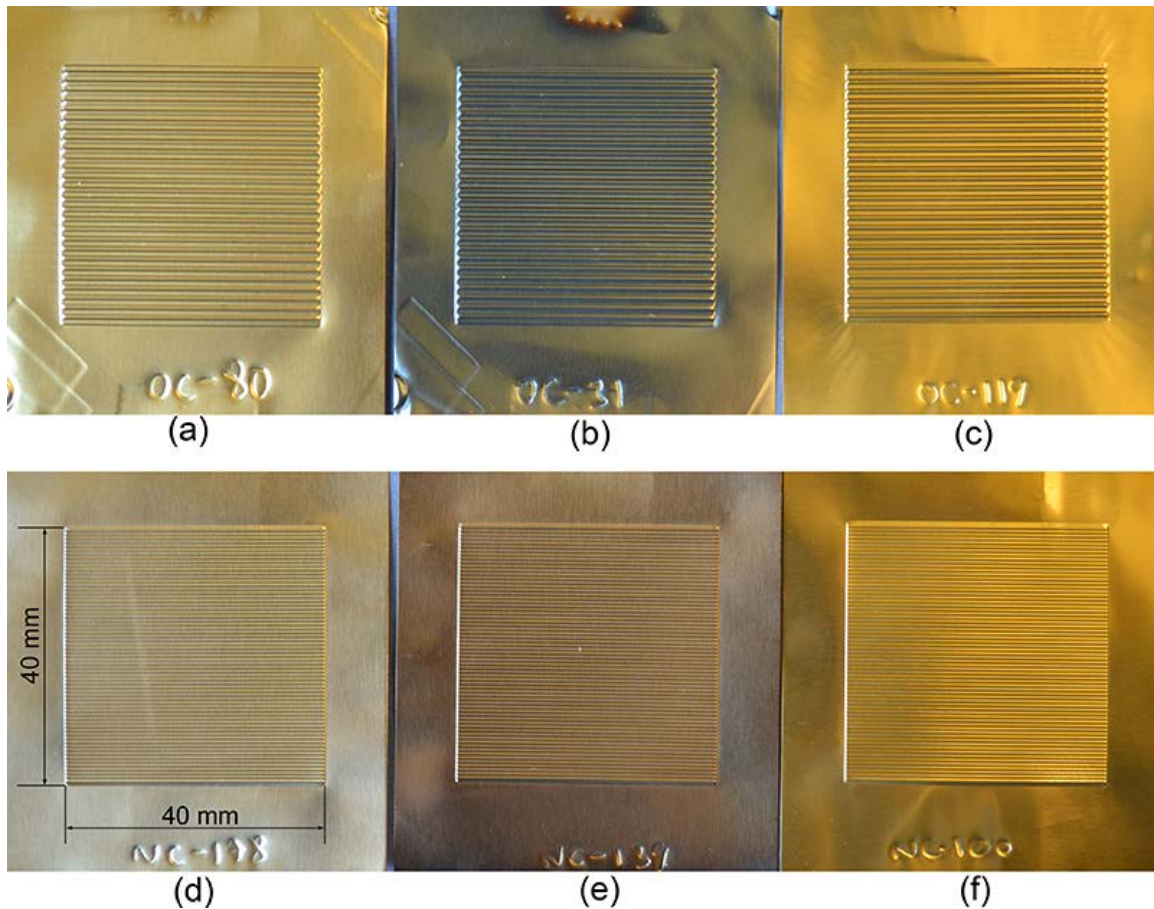
Figure 4-1 Examples to SS316L BPPs coated with different coatings and formed at different feature sizes: a) 1 µm ZrN, b) 1 µm CrN, c) 1 µm TiN, d) 0.1 µm ZrN and e) 0.1 µm TiN coated BPP.
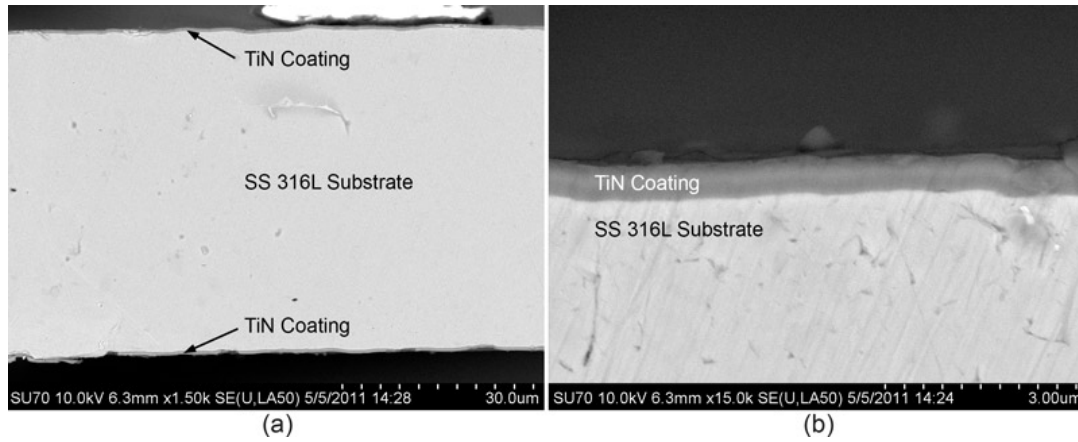
Figure 4-2 Cross-section SEM pictures of BPP substrate material with 1µm-thick TiN coating showing a) whole-width cross-section of substrate and coating layers at two side, b) higher magnification at one side.
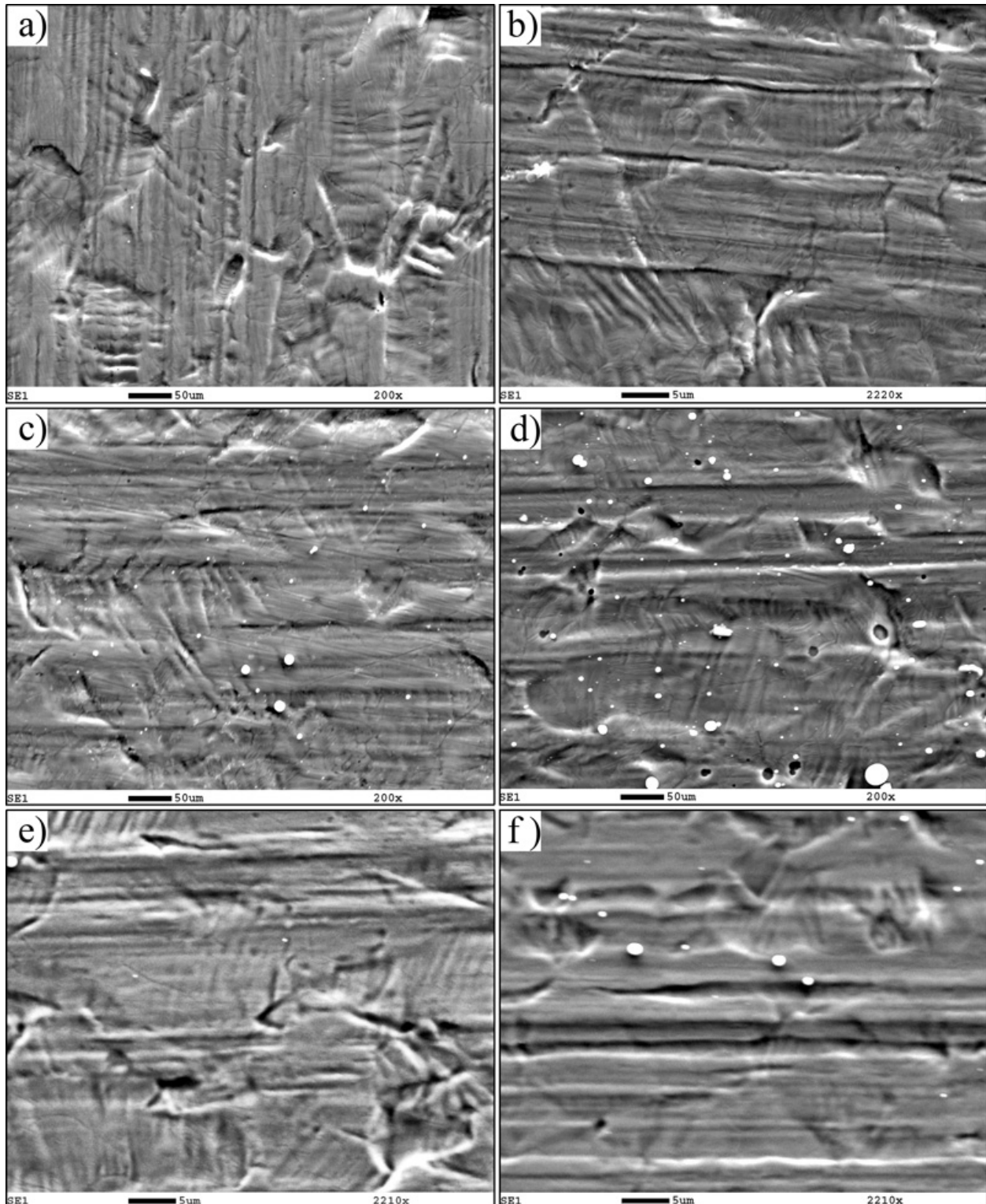
Figure 4-3 SEM images of some BPP samples with a) 0.1 μm CrN, b) 1 μm CrN, c) 0.1 μm TiN, d) 1 μm TiN, e) 0.1 μm ZrN and f) 1 μm ZrN coating.
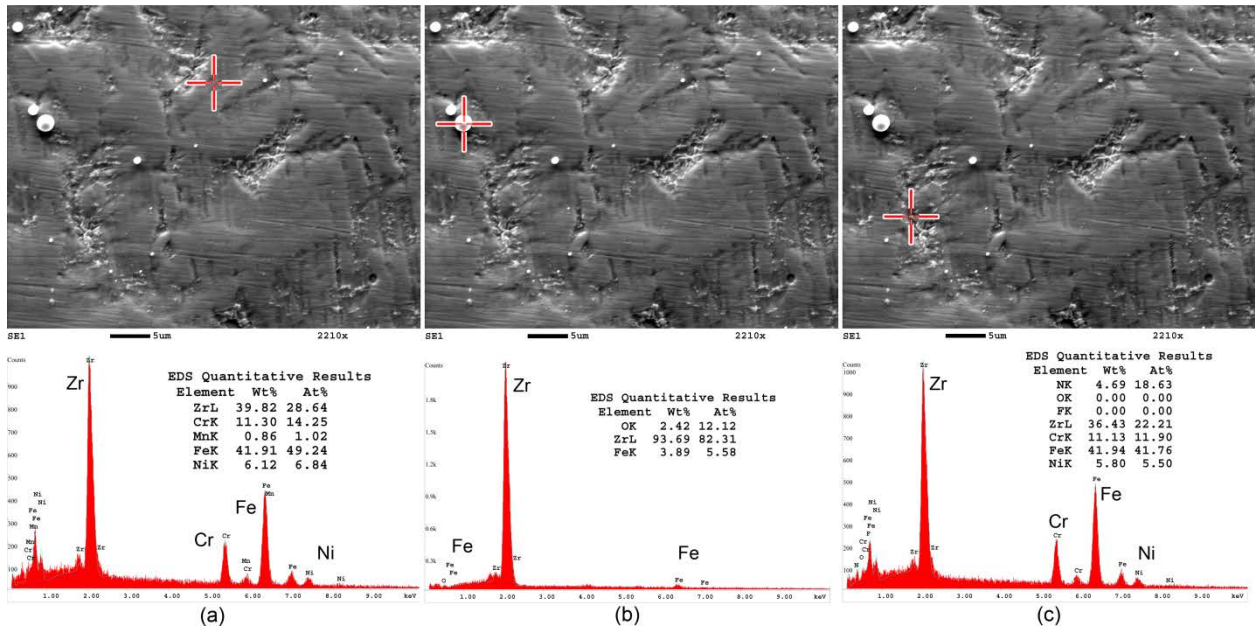
Figure 4-4 SEM images and EDX results for 1μm-thick ZrN coated samples showing a) regular smooth area, b) macro-defect and c) pitting region.
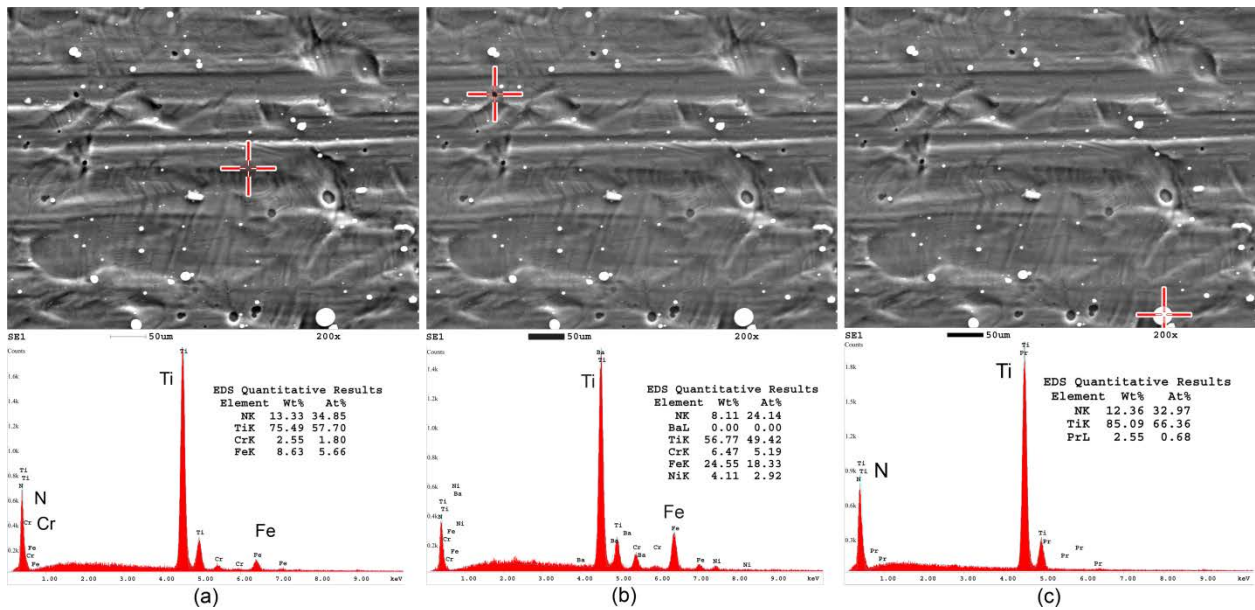
Figure 4-5 SEM images and EDX results for 1μm-thick TiN coated samples showing a)regular smooth area b) pinhole and c) macro-defect.

4.3.2.   Surface Roughness Results

To reveal a possible relationship with ICR, surface roughness values of the BPP samples were measured and reported in Figure 4-6.   Roughness measurements were taken from channel tips, which are typically in contact with gas diffusion layer (GDL) in PEMFC.   Average roughness (R_a) of uncoated and 1 µm-thick ZrN coated blanks was almost one order of magnitude lower than that of formed counterparts.   Stamped samples showed slightly higher roughness than hydroformed samples, 1.72 µm and 1.76 µm respectively, in uncoated case.   On the other hand, this discrepancy markedly increased in 1µm-thick ZrN coated case with 2.39 and 3.51 µm for hydroforming and stamping, respectively.

Surface roughening due to plastic deformation can be induced by intrinsic and/or extrinsic effects.   Microstructure dynamics of bulk plasticity induced intrinsic defects.   On the other hand extrinsic defects are results of external effects such as mechanical contacts of tools, friction and wear [146,147].   In the case of this study, roughening occurred mainly intrinsically yet die-substrate contact occurred at the other side of channel tips.   The most effective factors on roughening behavior were reported in literature as strain, grain size and texture whereas the roughness increase was irrespective of the stress state [148,149].

88
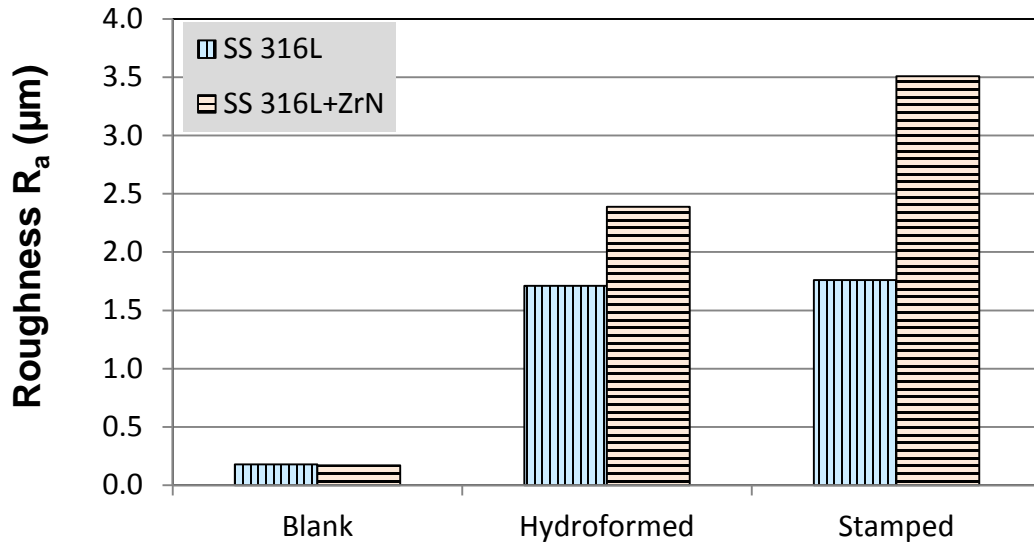
Figure 4-6 Surface roughness values of uncoated and 1 μm-thick ZrN coated samples

4.3.3. ICR Test Results for Blank (Unformed) Samples

4.3.3.1. Effect of Compaction Pressure

The first set of tested samples was uncoated and coated blank sheets (unformed). Evolution of the ICR between blank samples and carbon paper GDLs with increasing compaction pressure is presented in Figure 4-7. Pictures at right-hand side show ICR between 100 and 200 N/cm^2 compaction pressure for easy comparison while pictures at left-hand side show whole range used in the experiments. Each condition was tested three times to address the repeatability. A noticeable decrease in ICR was observed with increasing compaction pressure. Increase in compaction pressure brings the BPP and GDL surfaces closer; consecutively, the number of contacting surface asperities increases. Moreover, existing contact points at the interface are flattened due to plastic deformation. Thus, increase of real contact area between GDL and BPP surfaces decreases ICR [118,150].

89

4.3.3.2. Effect of Coating Type for Blank Samples

ICR tests showed that the coating type affected the ICR values of the samples, distinctively. Lower ICR values are desired to reduce parasitic power losses and increase current density in order to improve efficiency and power density of PEMFC. TiN coated samples showed the best (lowest) ICR values while the CrN coating yielded the highest ICR, even higher than that of uncoated samples, unpredictably. ICR performance of ZrN coated samples was found to be between TiN and uncoated samples as depicted in Figure 4. ICR values were obtained as 157, 21, and 12 mΩ-cm^2 for TiN, 1583, 339 and 343 mΩ-cm^2 for ZrN and 1762, 1364 and 3788 mΩ-cm^2 for CrN coated BPPs with 0.1, 0.5 and 1 µm thickness values, respectively. Findings were discussed and compared with literature in Section 4.4 in detail.

4.3.3.3. Effect of Coating Thickness on ICR Values of Blank Samples

In order to determine the optimum coating thickness for ICR value, coating thickness effect was investigated. It was observed that the increase in the coating thickness from 0.1 µm to 0.5 µm led to a decrease in the ICR values considerably in the cases of TiN and ZrN-coated BPPs while an ambiguous trend was observed for CrN case (see Figure 4-7). Further increase in coating thickness (from 0.5 to 1 µm) did not help lowering the ICR values, in general. A coating thickness of 0.5 µm resulted in the lowest ICR value of 1364 mΩ-cm^2 for CrN coated samples. Thicker CrN coating layer (1µm), on the other hand, yielded a remarkably increased ICR value of 3788 mΩ-cm^2.   It should be noted that even the lowest ICR value obtained for CrN coated samples was higher than that of uncoated SS316L. ANOVA tests were performed to reveal the statistical significance of coating thicknesses on ICR results. Analyses were conducted for %95 confidence interval. P-values of less than 0.05 indicated statistically significant differences

90

between two compared groups. According to ANOVA results, differences between coating thicknesses for the same type of coating were significant (p-vales between 0 and 0.016) except the case of comparison between 0.5 and 1 μm thick-ZrN coated samples (p=0.959) as shown Table 4-3. Coating thickness of 0.5 μm seems to be enough to obtain optimum ICR values for ZrN coating material, disregarding other possible factors such as degradation in time in PEMFC working conditions.
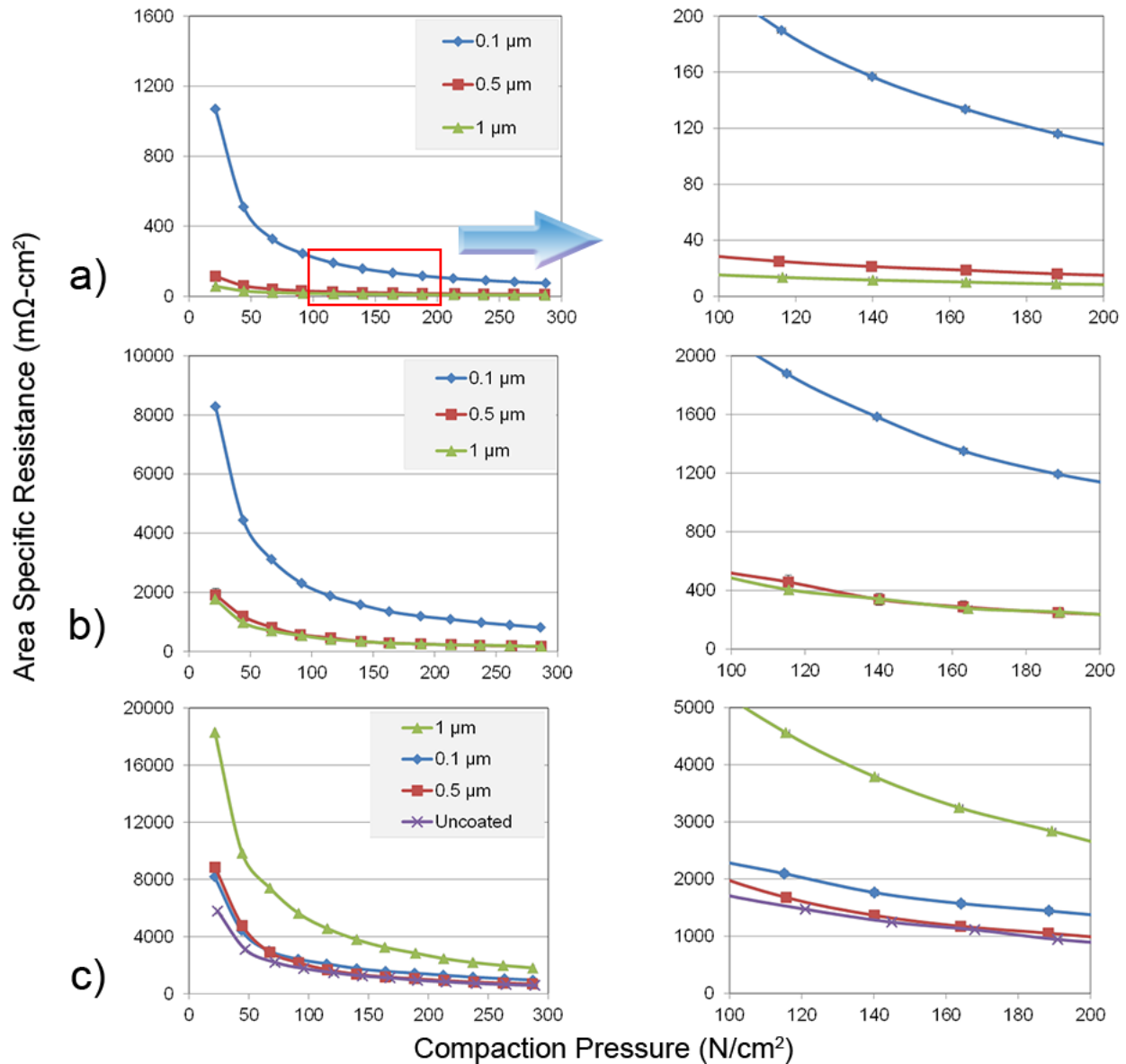
Figure 4-7 ICR evolution of SS316L blanks coated with a) TiN, b) ZrN, c) CrN and uncoated samples with respect to compaction pressure. (0.1μm, 0.5μm and 1μm are coating thicknesses.)

Table 4-3 Statistical analyses on the ICR values of SS 316L blankss with different coating thicknesses.

| Coating Type | Comparison of Coating Thicknesses (µm) | |
| | 0.1 vs 0.5 | 0.5 vs 1 |
	Statistical Significance (p-value)	Statistical Significance (p-value)
CrN	Yes (0.010)	Yes (0.000)
TiN	Yes (0.016)	Yes (0.004)
ZrN	Yes (0.000)	No (0.959)

4.3.4. ICR Results for Formed Samples

4.3.4.1. Effect of Compaction Pressure

Evolution of the ICR with regard to increasing compaction pressure is presented in Figure 4-8 for some of the representative uncoated and coated BPP samples. Carbon paper GDLs (Toray TGP-H 60, Toray Corp., Tokyo, Japan) were used in all tests. Since ICR values for various coatings distinctly differ from each other, logarithmic scale was employed. Variation bars represents maximum and minimum ICR values encountered. Due to increasing real contact area between GDL and BPP surfaces, a noticeable decrease in ICR was observed with increasing compaction pressure.

Contact areas were measured as explained Section 3.2.4. and area specific contact resistance (ASR) values as well as compaction pressures were recalculated based on these measurements as shown in Figure 4-9. Because of simplifications and lack of precision of the area measurement method, resistance of formed samples examined in terms of ICR instead of ASR in next sections. ASR values of formed and coated BPPs based on FEA calculation were presented in Appendix.

93
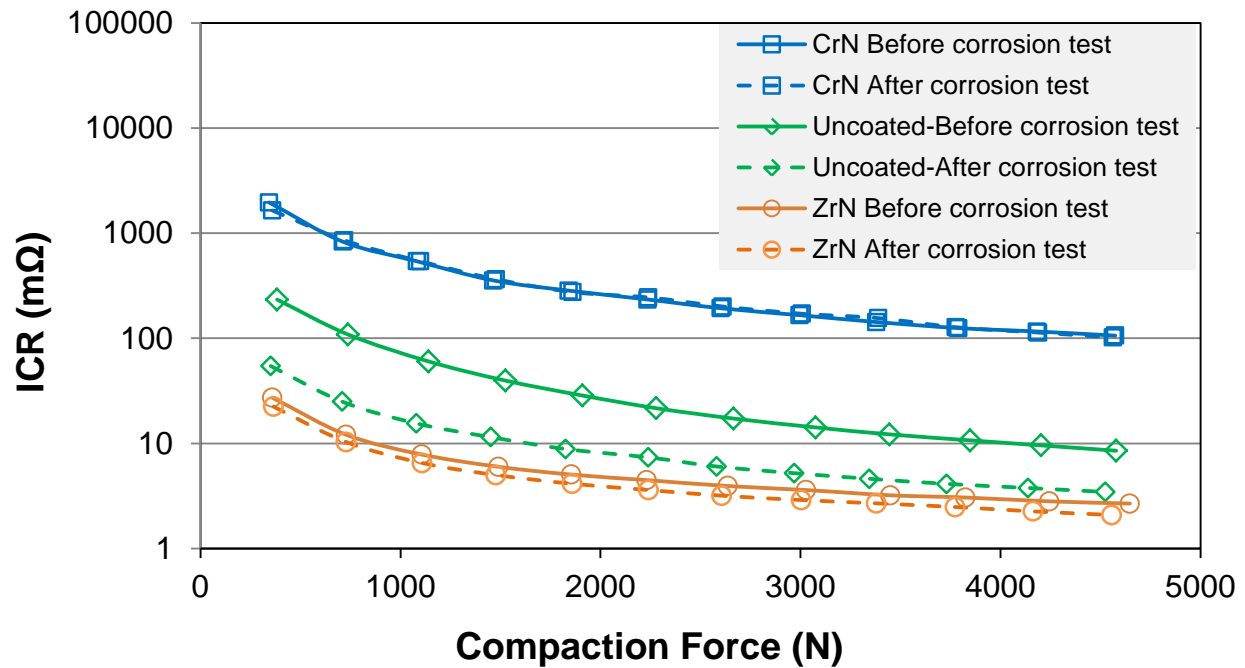
a)
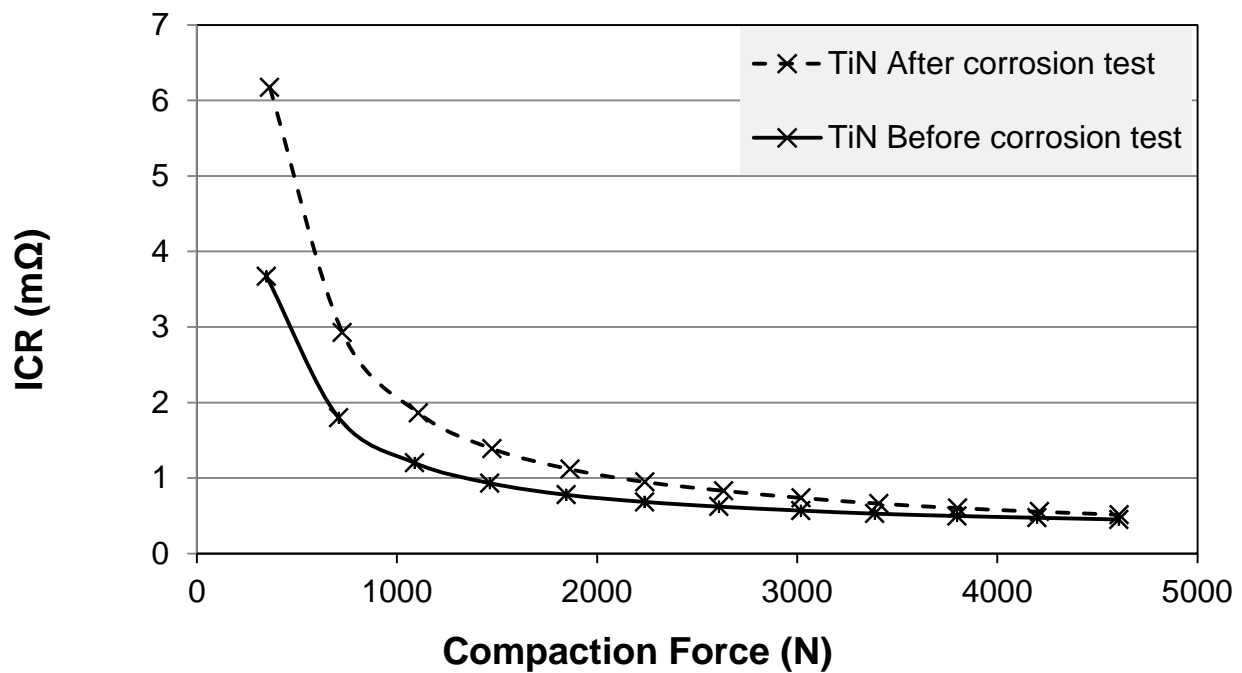
b)

Figure 4-8 ICR evolution of some representative a) CrN and ZrN coated and uncoated, b) TiN coated BPP samples by compaction force (Coating thickness: 1 μm, Forming Method: Stamping, Die: 750 μm).
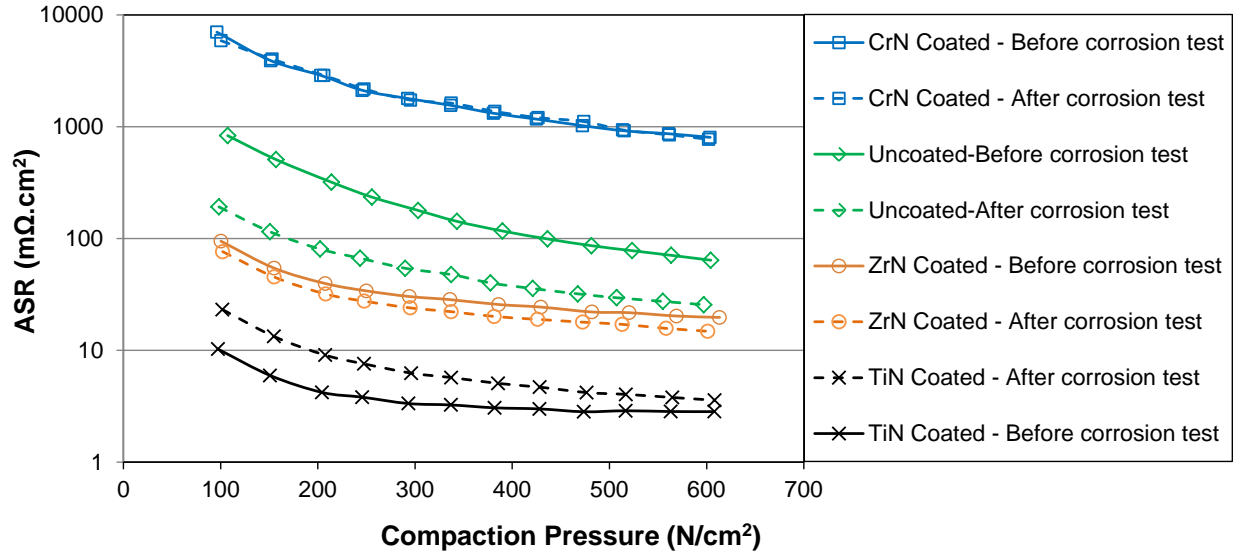
Figure 4-9 ICR evolution of samples by compaction pressure based on real contact areas measured by using pressure sensitive films (Coating thickness: 1 μm, Forming Method: Stamping, Die: 750 μm).

4.3.4.2. Effect of Forming Process and Feature Size on the ICR Values of Formed Samples

Figure 4-10 demonstrates the effect of different manufacturing methods and micro-channel size of dies used to form BPP samples on ICR. It can easily be noticed that forming process did not differentiate the ICR results significantly, in most cases. Similarly, channel size was observed to be effective in few cases only. To confirm these statements ANOVA analyses were conducted. Three different ICR test results for each case were obtained at the compaction force level of 2240 N were subjected to ANOVA tests for 95% confidence interval. Comparison of ICR values was performed in terms of manufacturing method, and channel size. Analyses showed that manufacturing method affected the ICR values in 3 out of 18 cases, only (* Indicates statistically significant difference between two adjacent columns in Figure 4-10). It is concluded that the forming method was not a significant factor on ICR values for BPPs.

95

Similarly, differences between the ICR values for BPPs manufactured with two different die channel size (250 and 750μm) were statistically significant in 5 out of 18 cases.

4.3.4.3. *Effect of coating thickness on the ICR values for formed samples*

Coating thickness yielded different effects on ICR values as illustrated in Figure 4-10. Increasing the thickness for CrN coating increased the ICR while increasing the thickness for TiN and ZrN coatings decreased the ICR. ANOVA analyses were conducted to disclose the statistical significance of coating thicknesses on ICR. Seven out of nine cases indicated that differences between the compared 0.1 and 0.5μm thick-coated samples were statistically significant (see Table 4-5). On the other hand, there were no significant difference between 0.5 and 1μm coated samples for six out of nine cases. As shown in Figure 4-10, CrN coating yielded very close ICR values for 0.1 and 0.5 μm-thick coating cases. Similarly, ICR values for TiN and ZrN coatings with 0.5 and 1μm thicknesses were in close proximity (see Table 4-5).
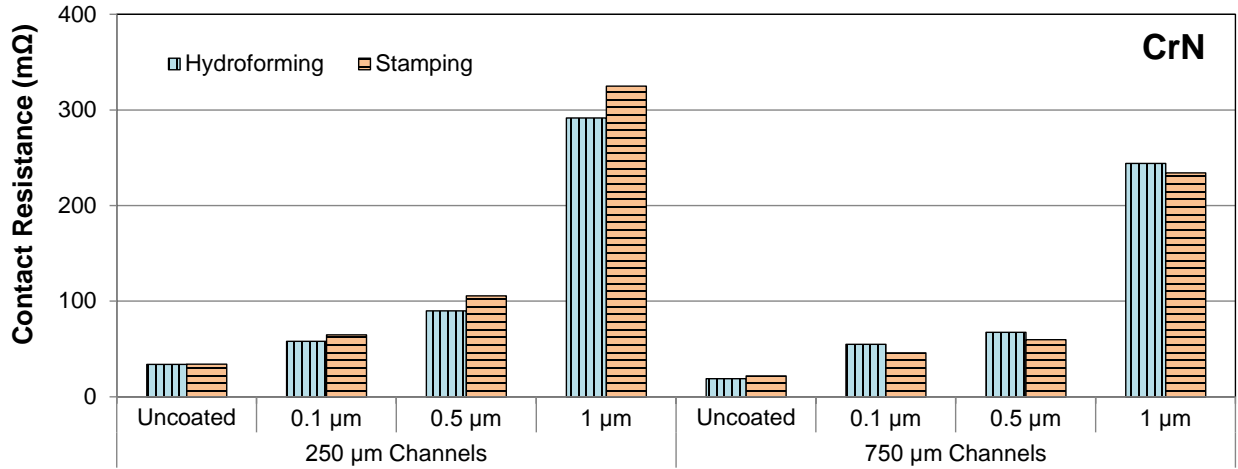
a)
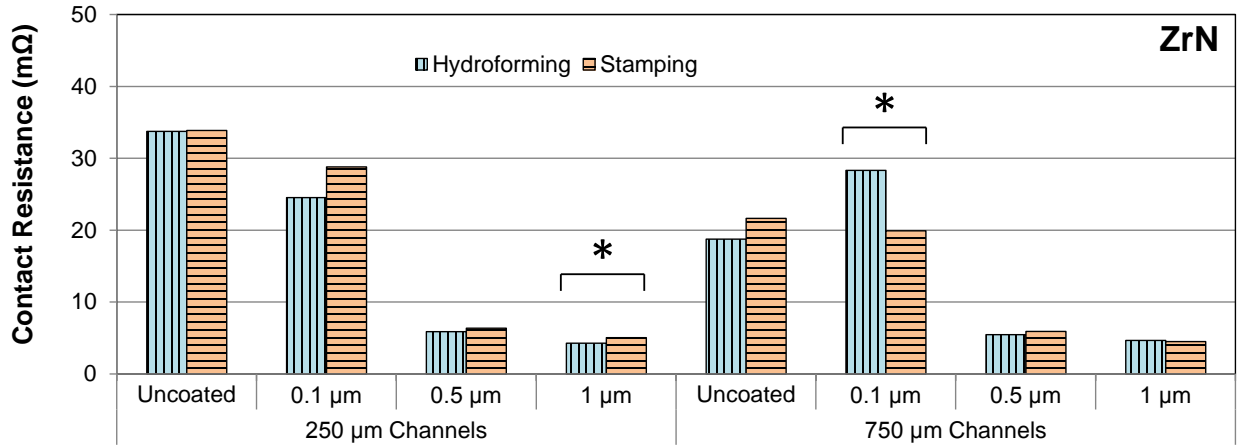
b)
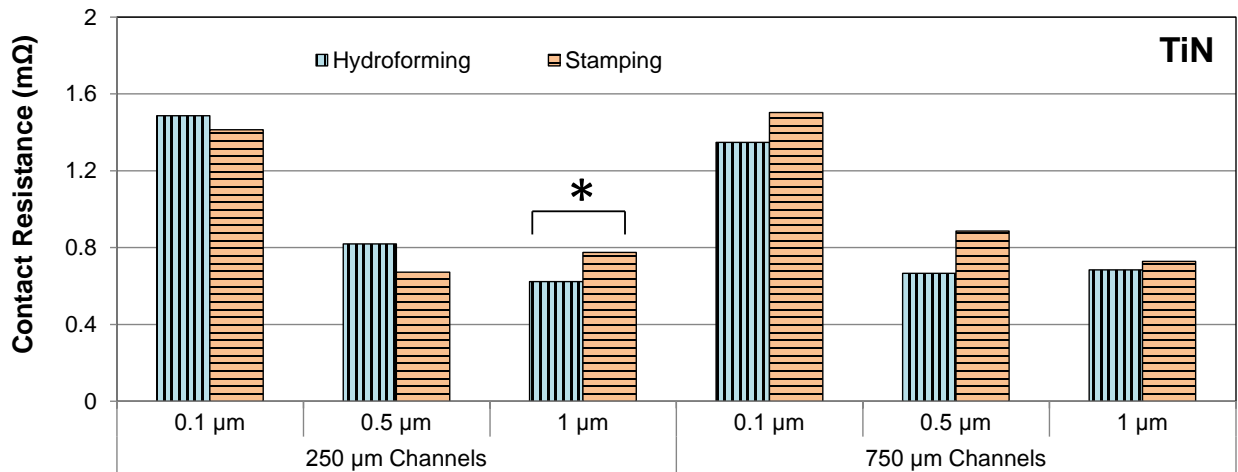
(c)

*Figure 4-10 Contact resistance of a) CrN, b) ZrN, and c) TiN Coated BPP samples acquired at 2240 N compaction force. * Indicates statistically significant differences between two columns.*

97

Table 4-4 Comparison of ICR values for BPPs in terms of two different channel size.

Coating Material	Forming Method	Coating Thickness (µm)	Statistical Significance (p-value)
CrN	Hydroforming	0.1	No (0.733)
		0.5	Yes (0.045)
		1	No (0.304)
	Stamping	0.1	Yes (0.020)
		0.5	Yes (0.024)
		1	No (0.070)
TiN	Hydroforming	0.1	No (0.395)
		0.5	No (0.408)
		1	Yes (0.048)
	Stamping	0.1	No (0.512)
		0.5	No (0.178)
		1	Yes (0.012)
ZrN	Hydroforming	0.1	No (0.207)
		0.5	No (0.329)
		1	No (0.127)
	Stamping	0.1	No (0.051)
		0.5	No (0.605)
		1	No (0.133)

Table 4-5 Statistical significance of effect of coating thickness on ICR.

Coating Type	Manufacturing Method	Die Feature Size (μm)	Comparison of Coatings (μm)	
			0.1 vs 0.5	0.5 vs 1
			Statistical Significance (p-value)	Statistical Significance (p-value)
CrN	Hydroforming	250	Yes (0.004)	Yes (0.002)
		750	No (0.293)	Yes (0.005)
	Stamping	250	Yes (0.030)	Yes (0.003)
		750	No (0.090)	Yes (0.001)
TiN	Hydroforming	250	Yes (0.008)	No (0.191)
		750	Yes (0.030)	No (0.262)
	Stamping	250	Yes (0.000)	Yes (0.015)
		750	Yes (0.025)	No (0.197)
ZrN	Hydroforming	250	Yes (0.001)	Yes (0.001)
		750	Yes (0.000)	No (0.133)
	Stamping	250	Yes (0.002)	No (0.057)
		750	Yes (0.000)	No (0.119)

4.3.5. Effect of Corrosion Test on ICR Results

In order to reveal the effect of PEMFC operation conditions on ICR values for BPPs, coated and uncoated BPP samples were subjected to corrosion conditions. Table 4-7 presents the ICR results of coated blank samples obtained before and after corrosion tests. As a general trend, corroded samples revealed higher ICR values than that of fresh samples.

Figure 4-11 presents ICR values for BPPs measured before and after corrosion tests. 1μm CrN coated samples demonstrated increased ICR values after corrosion test whereas ICR values of 0.1 and 0.5μm CrN coated samples did not change the results, significantly. In the case of ZrN coated samples, ICR values of the 0.1 and 0.5 μm thick-coated samples increased significantly after corrosion test while ICR measurements for 1μm coated samples remained same or even decreased after the corrosion test. Table 9 summarizes ANOVA results to assess effect of ZrN coating on BPP samples under corrosion test conditions. TiN coated samples were

99

found to be most vulnerable to the corrosion. Their ICR values were excessively increased after corrosion tests. Coating thickness was found to be very significantly affecting the ICR of TiN coated samples. 1μm-thick TiN coated BPP samples showed the lowest ICR values. Moreover, increasing coating thickness alleviated the effect of corrosion on ICR for TiN coated BPP samples.

Table 4-6 ICR values of unformed samples before and after corrosion test.

Coating Type	Coating Thickness (μm)	ICR Before Corrosion Test (mΩ)	ICR After Corrosion Test (mΩ)			
			PDH	PDO	PSH	PSO
CrN	0.1	110.1	127.1	118.6	183.6	121.4
	0.5	85.3	-	102.9	123.5	208.1
	1	236.8	-	225.7	487.5	-
TiN	0.1	9.8	-	4.7	2.3	10.5
	0.5	1.3	-	19.6	2.6	4.3
	1	0.7	1.0	2.7	1.0	1.5
ZrN	0.1	99.0	-	132.6	103.0	167.4
	0.5	21.2	-	38.9	196.9	132.2
	1	21.5	22.5	21.7	43.6	22.0
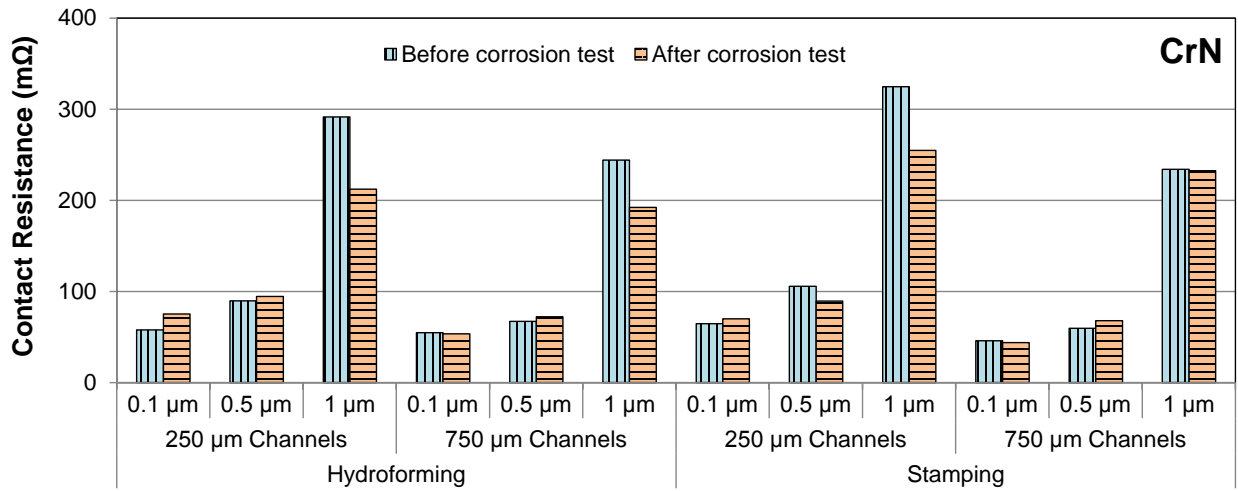
a)
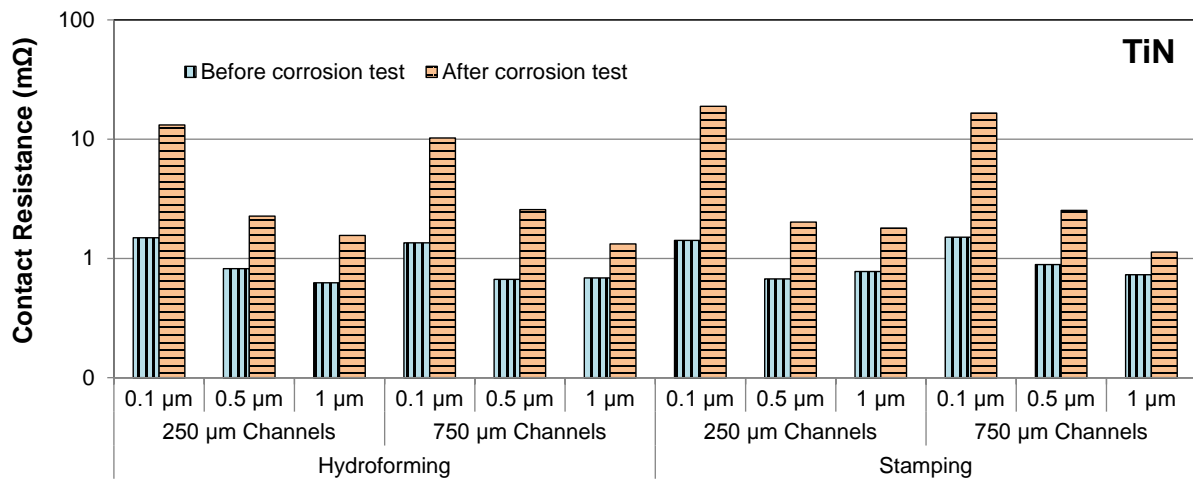
b)
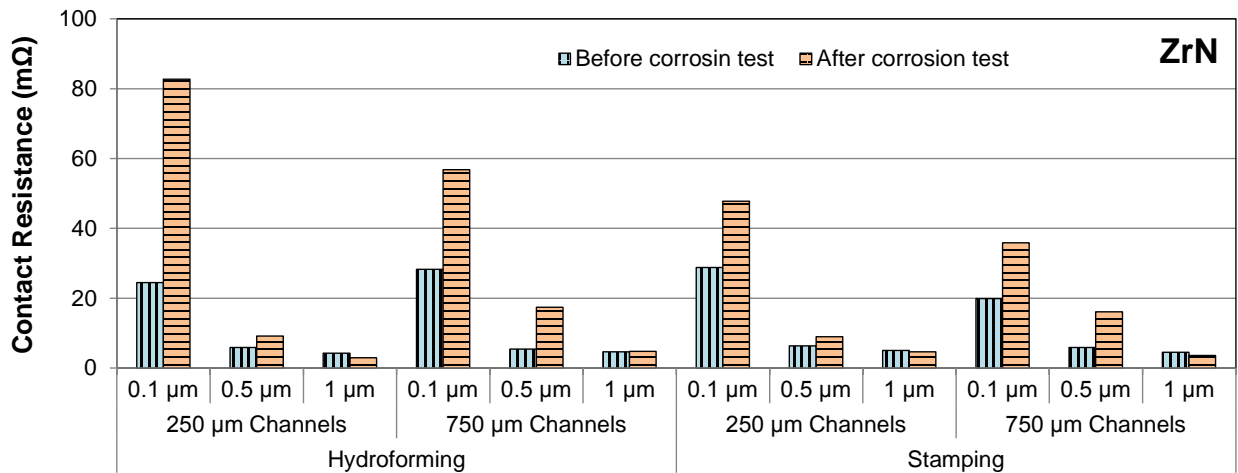
c)

Figure 4-11 ICR of BPP samples before and after corrosion test for bipolar plates coated with a) CrN, b) ZrN, c) TiN coatings

101

Table 4-7 ICR values of ZrN coated BPP samples before and after corrosion test and statistical significance of the differences between them.

Forming Method	Die Feature Size (μm)	Coating Thickness (µm)	Statistical Significance (p-value)
Hydroforming	250	0.1	Yes (0.007)
		0.5	No (0.228)
		1	Yes (0.002)
	750	0.1	Yes (0.004)
		0.5	Yes (0.027)
		1	No (0.875)
Stamping	250	0.1	No (0.083)
		0.5	No (0.443)
		1	No (0.629)
	750	0.1	Yes (0.000)
		0.5	No (0.057)
		1	No (0.410)

4.4. Discussion and comparison of ICR values with literature

ICR between BPP and GDL are dictated by surface morphology and chemical composition of contacting pairs for a given compaction pressure. To ensure the reliability of tests, several measures were applied. For example, average roughness (R_a) for all the tested BPP samples was measured in the range of 0.15-0.17 µm. In each test, same type of undeformed GDL materials was utilized. Hence, coating type and thickness values are left as only variables in test spec.

Numerous studies have been dedicated to reveal effect of coating materials and methods on ICR of BPPs in literature. Table 4 summarizes ICR values reported in some of those studies for uncoated blanks and coated plates for comparison to current study. As it can be noticed from Table 4, a very wide range of ICR values were reported for similar coatings. The most

102

consistent data presented in literature is for TiN coated BPP materials and these values are in relatively good agreement with this study as well (see Table 4-8). ZrN is the least reported coating for BPPs, and the value obtained in current study is higher than that of available in literature [90]. This discrepancy, most likely, came from difference between substrate preparation processes. While simple degreasing and cleaning processes were applied on substrates before coating in current study, some mechanical and chemical treatments were performed on substrates in most studies. CrN coating with different preparation variables was extensively studied by researchers and wide range of ICR values were reported. Although low ICR values were generally reported in literature, CrN coated samples showed higher ICR values, even more than that of uncoated samples, in present study. All these variations, especially in CrN, can be explained by complex nature of resistivity of the coatings as discussed below.

Wide range of resistivity values for TiN, CrN and ZrN reported in literature as summarized some of them in Table 5. The change in the electrical resistivity has been explained by variations in the microstructure, roughness, stoichiometry of the films, the level of impurities incorporated, and defect density [108]. The lowest resistivity values of each material can be cited as ρ_{TiN}=18 µΩ-cm [138] , ρ_{ZrN}=13.6 µΩ-cm [151] and ρ_{CrN}=µ640 Ω-cm [152] for their single-crystal bulk forms. However, resistivity of thin polycrystalline films is strongly higher than the resistivity of the corresponding bulk single-crystalline material [153]. The electrical resistivity of thin films depends on their composition, microstructure and impurities [113]. Reactively deposited films show the lowest resistivity in their stoichiometric composition [154-161]. For example, Kang and Kim observed minimum resistivity of 60 µΩ-cm for stoichiometric composition of TiN, while substoichiometric $TiN_{0.7}$ and super stoichiometric $TiN_{1.2}$ showed increased resistivity values of 102 and 79 µΩ-cm, respectively [155]. Similarly,

103

Benia et al. reported 65, 200 and 65,000 μΩ-cm for stoichiometric ZrN, substoichiometric $ZrN_{0.25}$ and super stoichiometric $ZrN_{1.4}$, respectively [161]. Indeed, resistivity of CrN_x is much more sensitive to stoichiometry, compared to that of TiN_x and ZrN_x. Martinez et al. measured resistivity of 640 μΩ-cm for $CrN_{0.96}$ when resistivity of $CrN_{1.06}$ was 10,000 μΩ-cm [158]. Moreover, Gall et al. cited that the resistivity values of CrN films reported in literature vary by more than six orders of magnitude, ranging from 300 to $6x10^8$ μΩ-cm [162]. They speculated that non-stoichiometry, grain boundaries, impurities, extended defects, sample geometry, and density might alter resistivity of powder or polycrystalline thin film samples. TiN and ZrN materials exhibit metallic resistivity behavior with positive temperature coefficient. In CrN case, early reports also indicated metallic like character; however, newer studies argued that CrN display semiconductor, even insulator behavior [163,164].

In the light of above mentioned reports, it can be said that the rank of the measured values of ICR of coated BPP samples were found in accordance with rank of electrical resistance of their coating materials, in general. Lower ICR values for CrN coated samples may be attributed to possibility of formation of Cr_2N which has markedly lower resistivity, compared to CrN. It is reported in literature occasionally that formation of Cr_2N is very likely in thermal nitridation process and high temperature deposition process [74,76,79,145,165-169].

Table 4-8 ICR values of metallic BPP materials prepared with various coating and/or surface treatment methods reported in literature.

Substrate Material	Coating Method/ Surface Treatment	Coating Material	Contact Resistance ($m\Omega\ cm^2$)	Reference
SS316L	Uncoated	Uncoated	160 at 140 N/cm^2	[74]
Ni-50Cr	Uncoated	Uncoated	60 at 140 N/cm^2	[74]
Ni-50Cr	Thermal Nitridation	CrN/Cr$_2$N	<20 at 140 N/cm^2	[74]
SS349^{TM}	Uncoated	Uncoated	100 at 140 N/cm^2	[74]
SS349^{TM}	Thermal Nitridation	CrN/Cr$_2$N	12 at 140 N/cm^2	[74]
SS446	Uncoated	Uncoated	~170 at 140 N/cm^2	[76]
SS446	Thermal Nitridation	CrN/Cr$_2$N	~4 at 140 N/cm^2	[76]
SS316L	Thermal Nitridation	CrN/Cr$_2$N	10 at 140 N/cm^2	[79]
SS316	Cathode discharge ion plating	TiN	40 at 140 N/cm^2	[28]
SS316	Physical vapor deposition	ZrN	160 at 140 N/cm^2	[90]
SS316	Physical vapor deposition	Zr	1000 at 140 N/cm^2	[90]
SS316L	Thermal Chromizing	Cr$_{23}$C$_6$ /Cr$_2$N	22 at 140 N/cm^2	[170]
1020	Thermal Chromizing		11.8 at 140 N/cm^2	[171]
SS316L	Thermal nitridation	Cr$_2$N	66 at 150 N/cm^2	[165]
SS316L	Thermal nitridation	CrN/Cr$_2$N	50 at 150 N/cm^2	[165]
SS446M	Thermal nitridation	CrN/Cr$_2$O3	6 at 140 N/cm^2	[166]
Fe–27Cr	Thermal nitridation	CrN/Cr$_2$N	50 at 140 N/cm^2	[167]
Fe–27Cr–2V	Thermal nitridation	CrN/Cr$_2$N	8 at 140 N/cm^2	[167]
Fe–27Cr–6V	Thermal nitridation	CrN/Cr$_2$N	5 at 140 N/cm^2	[167]
SS 316L	PVD	Cr/CrN/Cr$_2$N	100 at 150 N/cm^2	[168]
SS316L	Multi-arc ion plating PVD	Cr/CrN	30 at 150 N/cm^2	[168]
SS316L	Uncoated	Uncoated	66.4 at 274.4 N/cm^2	[145]
SS316L	Electron beam PVD	TiN	35 at 274.4 N/cm^2	[145]

105

SS316L	Electron beam PVD	CrN	21.8 at 274.4 N/cm^2	[145]
SS316L	Electron beam PVD	TiAlN	7.5 at 274.4 N/cm^2	[145]
SS (not specified)	Pulsed bias arc ion plating	Cr+Cr$_2$N/CrN	5.8-24.5 at 120 N/cm^2	[169]
SS316	Uncoated	Uncoated	34.19 at 180 N/cm^2	[28]
SS316	Hollow cathode discharge ion plating	TiN	32.71 at 180 N/cm^2	[28]
SS310	Uncoated	Uncoated	~130 at 150 N/cm^2	[84]
SS310	Electrophoretical deposition	TiN	40 at 150 N/cm^2	[84]
SS310	Electrophoretical deposition	TiN/SBR	20 at 150 N/cm^2	[84]
SS316	Hollow cathode discharge ion plating	TiN	36 at 150 N/cm^2	[172]
SS316L	Uncoated	Uncoated	175 at 150 N/cm^2	[173]
SS316L	Radio frequency magnetron sputtering	TiN	25 at 150 N/cm^2	[173]
SS316L	Radio frequency magnetron sputtering	CrN	16 at 150 N/cm^2	[173]
SS304	Uncoated	Uncoated	240 at 140 N/cm^2	[174]
SS304	Pulsed bias arc ion plating and magnetron sputtering	TiN	30 at 140 N/cm^2	[174]
SS304	Pulsed bias arc ion plating and magnetron sputtering	TiN/Ti$_2$N	25 at 140 N/cm^2	[174]
SS316L	Electropolished	Uncoated	590 at 150 N/cm^2	[175]
SS316L	Physical vapor deposition	CrN	3.5 at 150 N/cm^2	[175]
SS340	Physical vapor deposition	CrN	4.2 at 150 N/cm^2	[175]
A283-C	Electroplated Cr + thermally nitrided CrN	5µm Cr+CrN/Cr$_2$N	15 at 150 N/cm^2	[176]
A283-C	Electroplated Cr + Nitrided CrN/Cr2N	10 µm Cr+ CrN/Cr$_2$N	8 at 150 N/cm^2	[176]
SS316L	Uncoated	Uncoated	82.2 at 150 N/cm^2	[177]

106

SS316L	Inductively coupled plasma nitridation (-100V)	CrN	79.3 at 150 N/cm^2	[177]
SS316L	Inductively coupled plasma nitridation (-200V)	CrN	34.0 at 150 N/cm^2	[177]
SS316L	Inductively coupled plasma nitridation (-300V)	CrN	5.6 at 150 N/cm^2	[177]
SS316L	Uncoated	Uncoated	570 at 150 N/cm^2	[100]
SS316L	Unbalanced magnetron DC sputtering	CrN/Cr	4 at 150 N/cm^2	[100]

Table 4-9 Reported resistivity values of TiN, CrN and ZrN prepared with various methods and conditions.

Material	Coating Method / Structure	Resistivity ($\mu\Omega$-cm)	Reference
TiN	Single-crystal film	18	[138]
TiN	Polycrystalline	90	[138]
TiN	Single-crystal	23	[107]
TiN	Filtered vacuum cathodic arc	20	[113]
TiN	Off-plane double bend filtered cathodic vacuum arc	43-86 at deposition temperature between 50 and 500 °C (43 cm at 500°C)	[107]
TiN_x	DC reactive magnetron sputtering	60-110 at x between 0.7 and 1.2 (60 at x=1)	[155]
TiN	Radio frequency magnetron sputtering	24 prepared at 400 °C with 8% of nitrogen flow	[156]
TiN	Two step thermal nitridation	27-208 at various stoichiometry	[157]
TiN	Reactive evaporation and radio frequency sputtering	76-800 at various O_2 impurity	[178]
TiN	Reactive sputtering	20	[179]
TiN	Filtered vacuum cathodic arc source and simultaneous bombardment from nitrogen ion beam.	72-250 at N energy between 50 and 500 eV (72 at 50 eV)	[108]
$Ti_xTa_{1-x}N$	Dual ion beam sputtering	180-290 at x between 0 and 1	[180]
(Ti,Zr)N	Radio frequency magnetron sputtering	72.3 to 224.1 at packing factor between 0.62 and 0.8 (72.3 at packing factor of 0.8)	[181]
TiN	Radio frequency magnetron sputtering	75-415 at density between 4.99 and 5.12 g/cm^3	[182]
TiN	Reactive sputtering	47-95 at film thickness between 50 and 195 nm	[183]
TiN	The plasma beam sputtering at 200 °C	62	[184]
TiN	The plasma beam sputtering at 460 °C	21	[184]

TiN	Reactive sputtering	75-200 at N_2 flow ratio between 0 and 1 (75 at 0 and 0.22 N2 flow ratio)	[185]
TiN	Reactive sputtering	50-300 O/Ti ratio between 0.02 and 0.23 50 at the O/Ti ratio of 0.02	[186]
TiN	Sputter deposition	39-65 at Ti/N between 0.83 and 1.02 (39 at Ti/N ratio of 1.02)	[154]
TiN	Reactive sputtering	55	[187]
TiN	Bulk	20 ± 10	[188]
TiN	Bulk	25	[189]
TiN	Bulk	25	[190]
TiN	Single crystal by ultrahigh vacuum reactive magnetron sputter deposition	13	[191]
TiN	DC reactive magnetron sputtering	12.4	[192]
TiN	Plasma-beam sputtering	53	[193]
Cr_2N	Bulk	75	[189]
CrN/Cr_2N	Physical vapor deposition	min 29 at 0.01 N elemental composition	[159]
Cr/CrN	DC sputtering with different levels of argon and nitrogen flows	100-10,000 at N_2/Ar flow ratio between 0 and 1 100 at N_2/Ar flow ratio of 0	[160]
CrN	Ultra-high vacuum magnetically unbalanced magnetron sputter deposition	77,000	[162]
CrN	-	300- 600,000,000	[162]
CrN	-	600-800	[165]
Cr_2N	-	79-89	[165]
CrN	The plasma beam sputtering at 200	600-650	[184]
CrN	Plasma-assisted molecular-beam epitaxy	8,000	[194]
CrN	Reactive magnetron sputtering	350,000	[195]
CrN	DC magnetron sputtering	7,300-71,400 at substrate temperature between 550 °C and 850 °C 7,300 at 550 °C	[196]

109

CrN	Bulk	640	[152]
CrN	Reactive magnetron sputtering	2,000-1,0000	[152]
CrN	Plasma-beam sputtering	304	[193]
CrN	Reactive magnetron sputtering	1,200-7,000	[158]
CrN_x	Reactive magnetron sputtering	640 at x=0.96 10,000 at x=1.06	[158]
CrN	Bulk	10,000	[158]
ZrN	DC reactive magnetron sputtering under different negative substrate bias.	130-210 at bias voltage between 0 and 300V (130 at 200V)	[197]
ZrN	Single-crystal	13.6	[151]
ZrN_x	DC magnetron sputtering	65-20,000 at x between 0 and 1.4 (65 at x=0 and x=1, similar resistivity for Zr and ZrN)	[161]
ZrN	Hollow cathode discharge ion plating	64-837 at substrate bias between 0 and -150 V (64 at substrate bias of -120 V)	[198]
ZrN	Single ion beam sputtering	1,000-1,4000 at substrate temperature between 373 and 723 K (1,000 at substrate temperature 373 K)	[199]
ZrN	Bulk	7-21	[188]
ZrN	Bulk	21	[190]
ZrN	DC magnetron sputtering	190	[200]
ZrN	Ion beam sputter-deposition	250-300	[201]

110

4.5. Conclusions

Interfacial contact resistance of bipolar plates, as one of the crucial issues in PEM fuel cell operations, have been investigated in order to understand the effect of manufacturing method, and conditions, coating type and thickness, and corrosion exposure.

It was revealed that the manufacturing method and BPP channel size slightly affected the ICR of the metallic BPP samples whereas the effect of coating material and coating thickness was found to be significant. ICR tests surprisingly indicated that CrN coating increased the contact resistance of the samples compared to uncoated blank SS316L substrate material. ZrN coating, on the other hand, improved conductivity of the SS316L substrate material. Another noticeable finding with ZrN coated BPPs was that 0.5 and 1µm coated samples showed similar ICR performance after and before corrosion tests. Nevertheless, such improved levels of performance in ICR still do not meet the respective targets set by DOE [29]. TiN coated samples revealed the lowest electrical contact conductivity among the other coatings. ICR values for TiN coated samples were the only group close to meet the DOE targets. However, their ICR significantly increased after short term corrosion test. Next chapter is aimed to reveal the effect of manufacturing-coating sequence on ICR values to obtain a broader understanding in this field.

111

CHAPTER 5: Process Sequence Effect on Contact Resistance Characteristics of Coated Metallic Bipolar Plates for PEM Fuel Cells [1]

Abstract

This chapter is aimed for understanding the effect of process sequence on interfacial electrical contact resistance (ICR) of coated stainless steel (SS) 316L bipolar plates (BPP) for polymer electrolyte membrane fuel cells (PEMFCs). To this aim, in first group of testing, BPP samples were formed using two different manufacturing methods (hydroforming and stamping). Then, these formed BPP samples were coated with three different PVD coatings (CrN, TiN and ZrN) at three different coating thicknesses (0.1, 0.5 and 1 µm). In the second group, SS 316L blank samples were coated first; then, they were formed by the same manufacturing methods as in the first group. Finally, these two groups of BPP samples (formed-then-coated and coated-then-formed) were tested for their ICR to reveal effect of process sequence, namely coating before or after forming. In addition, ICR tests were applied to BPP plates both before and after corrosion exposure to disclose effect of near-real PEMFC conditions on the ICR. Contrary to predictions, BPP samples which were coated-then-formed exhibited similar or even better performance than formed-then-coated BPP samples in terms of ICR. Thus, forming of coated blanks seemed to be more favorable and worth further investigation in quest of making cost effective BPPs for mass production of PEMFC.

---

[1] The contents of this chapter are under final preparation to be submitted for publication.

5.1.Introduction

When coated metallic materials are preferred for BPP, order of process sequence would be important. Coating of BPPs after forming seems to be reasonable choice since one can expect that forming of coated blanks may deteriorate the surface due to possible deformation of coatings with brittle characteristics. On the other hand, forming of pre-coated metallic material can increase manufacturing speed of BPPs. "Finish first, fabricate later" is a growing trend in sheet metal manufacturing due to promise of simpler workflows, reduced stock, easier environmental compliance and lower overall costs [146,202].   Although the literature is abundant on investigating the effect of forming process on coating failures [203-206], to the best of knowledge of the authors, there is no dedicated study exploring the effect of processes sequence on ICR behavior of coated metallic BPP. The aim of this study was determined as to disclose effect of process sequence e.g., coating before forming versus coating after forming, on contact resistance of the coated metallic BPPs.

113

Table 5-1 Performance requirements for PEM fuel cell bipolar plates [29]

Property	Unit	Value
Tensile strength – ASTM D638	MPa	>41
Flexural strength – ASTM D790	MPa	>59
Electrical conductivity	S cm^{-1}	>100
Corrosion rate	μA cm^{-2}	<1
Contact resistance	mΩ cm^2	<20
Hydrogen permeability	cm^3 (cm^2 s)$^{-1}$	<2.10^{-6}
Mass	kg/kW	<1
Density – ASTM D792	g cm^{-3}	<5
Thermal conductivity	W (m K)$^{-1}$	>10
Impact resistance (unnotched) ASTM D-256	J m^{-1}	>40,5

5.2.Experimental Methodology and Conditions

In this study, two groups of coated metallic BPPs were investigated in terms of process sequence on ICR between BPPs and gas diffusion layer (GDL). The first group of samples were 'formed-then-coated' (FtC) BPPs while the second group of 'coated-then-formed' (CtF) BPP samples were coated as blank sheets; then, formed with same forming methods (stamping and hydroformed). Three different PVD metal nitride coatings, namely titanium nitride (TiN), chromium nitride (CrN), zirconium nitride (ZrN), at three different coating thicknesses, 0.1, 0.5 and 1 μm, were applied by Tanury Industries Co. (Lincoln, RI, USA). Table 5-3 shows PVD process parameters provided by supplier.

114

Two different die geometries were employed to obtain channels on BPP samples. Forming dies were named according to their channel heights, 250 and 750 μm, throughout the study. Forming parameters were selected as 40 MPa pressure with a pressure rate of 1 MPa/s in hydroforming and 200 kN force with a punch speed of 1 mm/s in stamping based on previous works. Detailed description of the forming processes employed and test setup used were given in a previous study by authors [133].

Bipolar plate surfaces were investigated with Hitachi SU-70 scanning electron microscope (SEM) fitted with EDAX energy dispersive X-ray spectroscopy system (EDX) and HIROX KH-7700 (HIROX-USA, NJ, USA) confocal optical microscope. Wyko NT1100 optical profiler (Veeco Instruments Inc., Tucson, AZ, USA) was used for BPP surface roughness measurements.

Interfacial contact resistances between samples and carbon paper GDL (Toray TGP-H 60, Toray Corp., Tokyo, Japan) were measured by the method developed by Wang [14]. The detailed information about the method and experimental setup were explained in Section 3.2.5 and [60,133]. ICR tests were conducted before and after corrosion tests in order to reveal effect of PEMFC conditions exposure on ICR values. Potentiodynamic electrochemical corrosion test with O_2 bubbling was chosen to simulate cathodic conditions of PEMFC. Potential range was changed between -1.2 V and 0.8 V with respect to standard hydrogen electrode (SHE) at a 1 mV/s rate in potentiodynamic experiments. Detailed explanation of the corrosion test procedure can be found in an earlier work [59].

Coated-after-forming samples underwent to ICR test as received whereas coated-before-forming BPP samples were subjected to ultrasonic cleaning in an acetone bath prior to ICR tests. Post corrosion test samples were also cleaned by acetone to remove the acidic solution residues.

115

Table 5-2 Chemical composition of SS316L (Browns Metals Co., Rancho Cucamonga, CA, USA).

C	Mn	P	S	Si	Cr	Ni	Mo	Cu	N	Fe
0.021	1.48	0.033	0.001	0.43	16.20	10.03	2.06	0.43	0.04	Bal

Table 5-3 Coating conditions (provided by Tanury Industries).

Run#	Coating	Thickness	Temperature	Deposition Time	Deposition Current	Bias Voltage	Nitrogen flow rate	Argon flow rate	Pressure
		(μm)	(°C)	(mins)	(A)	(V)	(sccm)	(sccm)	(m Torr)
1	TiN	0.1	60	6	450	75	500	800	5
2	TiN	0.5	60	38	450	75	500	800	5
3	TiN	1	60	75	450	75	500	800	5
4	CrN	0.1	60	2	450	75	500	800	5
5	CrN	0.5	60	4	450	75	500	800	5
6	CrN	1	60	8	450	75	500	800	5
7	ZrN	0.1	60	2	450	75	500	800	5
8	ZrN	0.5	60	8	450	75	500	800	5
9	ZrN	1	60	16	450	75	500	800	5

5.3. Results and discussions

5.3.1. Surface evaluation of substrate

Surface morphology of the substrate was investigated by using confocal optical microscopy. Figure 5-1a represent general appearance of formed uncoated BPP surface. Evolution of the surface due to forming process can easily be seen by comparing unformed blank (Figure 5-1b) and channel tip of formed BPP (Figure 5-1c).

Surface roughness values of unformed blank and formed BPPs with various surface conditions were reported in Figure 5-2. While roughness of uncoated and coated BPPs were in same order, roughness of uncoated blank was almost one order of magnitude lower than that of formers.

116

Surface roughening due to plastic forming can be induced by intrinsic and/or extrinsic effects. Microstructure dynamics of bulk plasticity induced intrinsic defects. On the other hand extrinsic defects are results of external effects such as mechanical contacts of tools and friction [146,147]. In the case of this study, roughening occurred mainly intrinsically yet die-substrate contact occurred at the other side of channel tips.   The most effective factors on roughening behavior were reported in literature as strain, grain size and texture whereas the roughness increase was irrespective of the stress state [148,149].
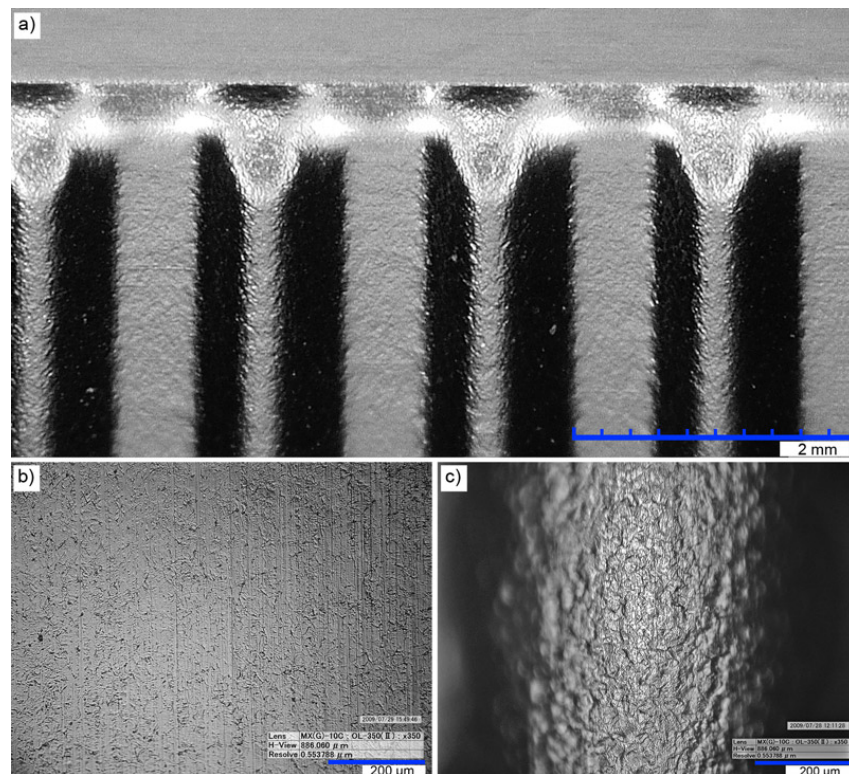

Figure 5-1 Optical images representing surface evolution due to forming process. a) Confocal microscopy image of BPP; b) surface morphology of unformed blank and c) channel tip of BPP.
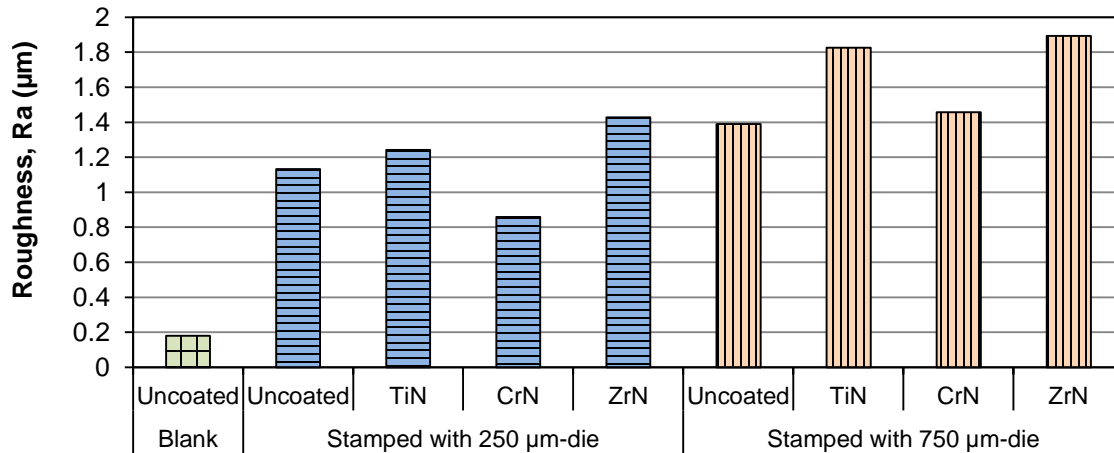
Figure 5-2 Surface roughness values of unformed blank substrate and BPP samples with different surface conditions.

5.3.2. SEM images of BBP samples

SEM images were used to investigate surface morphology of various BPP samples. Figure 5-3 compares effect of process sequence on coating structure. The sample in Figure 5-3a was formed first, then coated with 1 µm TiN, whereas samples in Figure 5-3b, Figure 5-3c and Figure 5-3d formed by using pre-coated blanks with 1, 0.5 and 0.1 µm thick TiN layer, respectively. Pitting defects are more visible in FtC sample (Figure 5-3a); coating cracks in transverse direction to strain are clearly noticeable only on CtF samples. Macro defects (white particles in pictures) are common for all samples (also investigated at Section 4.3.1). Density of cracks was higher at channel tips and walls compared to channel valleys due to different deformation pattern, as shown Figure 5-4a and Figure 5-4b respectively. Small amount of coating delamination and spallation were also detected as presented Figure 5-4c. Cracking paths mostly preferred to overlap macro defect points (see Figure 5-4d for close-up SEM micrograph). This fact can indicate that macro defects behave as notches in coating structure. TiN and ZrN coatings with different thicknesses exhibited similar patterns, mostly directional cracks to perpendicular to strain direction while various thickness CrN coatings showed different shape of

118

cracks (see Figure 5-5). Approximate interval between adjacent cracks was 2 µm for TiN and ZrN coatings regardless of thickness. On the other hand, 0.7 µm crack distance on 1 µm CrN coating reduced to 0.15 µm for 0.1 µm thick CrN coating, roughly. Another difference for 0.1 µm CrN coating was small rhombic cracks instead of directional and continuous patterns compare to others (see Figure 5-5).

In order to reveal elemental composition differences between non-cracked and cracked area EDX analysis was conducted on 1 µm-thick ZrN coated samples. Although ratio of Zr decreased markedly in cracking region (from 29.59 to 5.72 percent in weight), significant amount of Zr atoms were still detectable. This finding indicates that protective ZrN coating are still available in cracking area which is crucial to maintain corrosion protection while in contact resistance aspect, composition of this area is not expected so critical yet contact occurs at top of the coating surface only.

Erikkson et al. conducted a similar experiment to investigate the effect of plastic deformation on integrity of TiN coating [206]. They observed that cracking behavior depended on amount of strain and coating thickness. The authors also reported improvement of corrosion resistance of TiN coated samples compared to bare substrate material, in spite of damages on coating layer.
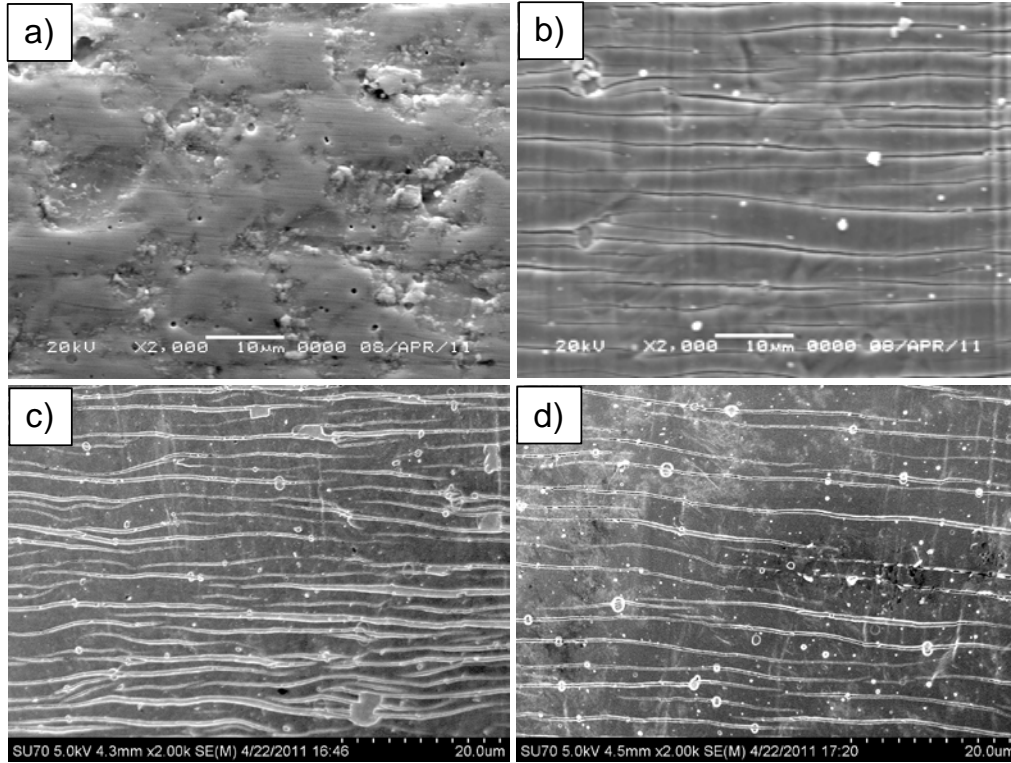
Figure 5-3 SEM images for a)1 µm TiN coated after forming, b) 1 µm, c) 0.5 µm,d 0.1 µm TiN coated beforeBPP samples.
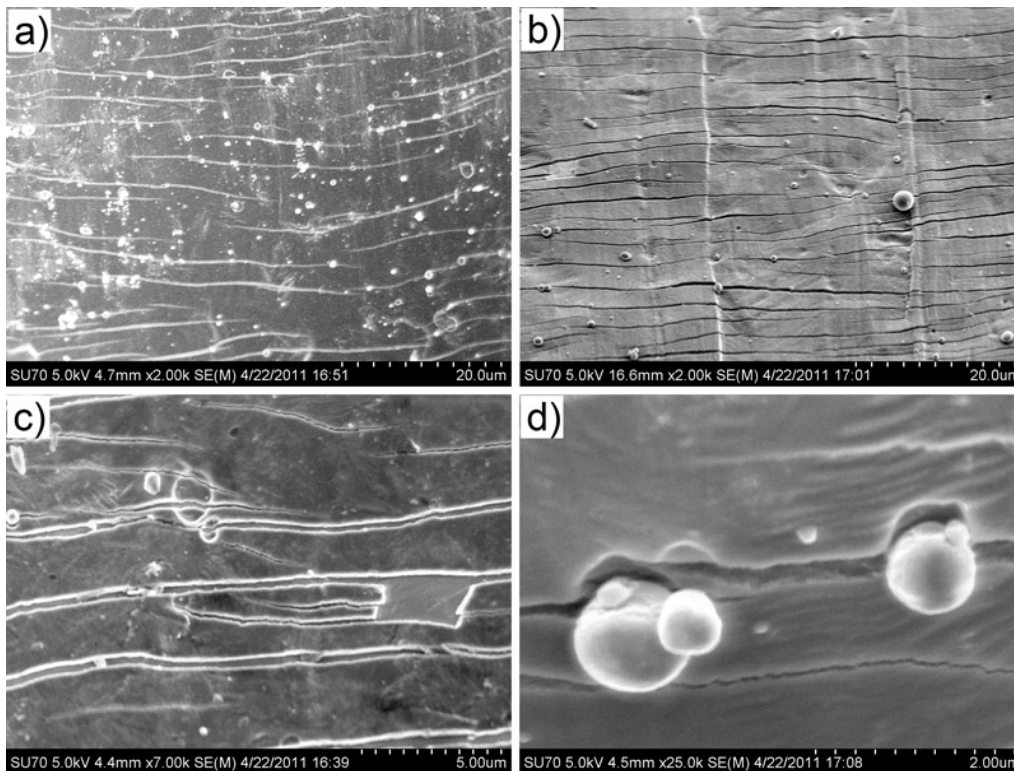
Figure 5-4 SEM images of 0.5 µm TiN coated BPP samples showing a) channel valley, b) channel wall, c) close up view cracking and spallation area and d) macro defects.

Figure 5-5 SEM images of a) 1 µm ZrN b) 1 µm CrN c) 0.5 CrN and d)0.1 µm CrN coated samples. (All samples were stamped with 750 µm-die and images were taken from channel tips).

Figure 5-6 EDX analysis of ZrN coated BPP samples at a) non-cracked and b) cracked area.

121

5.3.3. ICR Evolution of BPP Samples with Compaction pressure

Evolution of the ICR with regard to increasing compaction pressure is presented in Figure 5-7 for some of the representative uncoated and coated BPP samples. Uncoated BPP sample was also included to the experime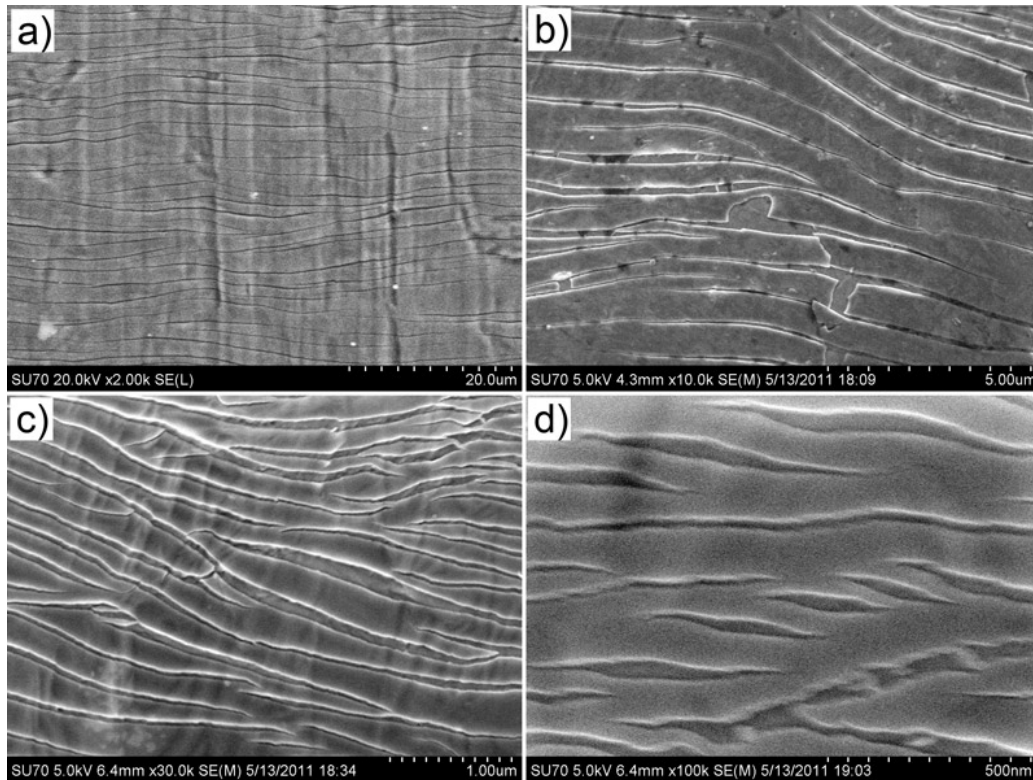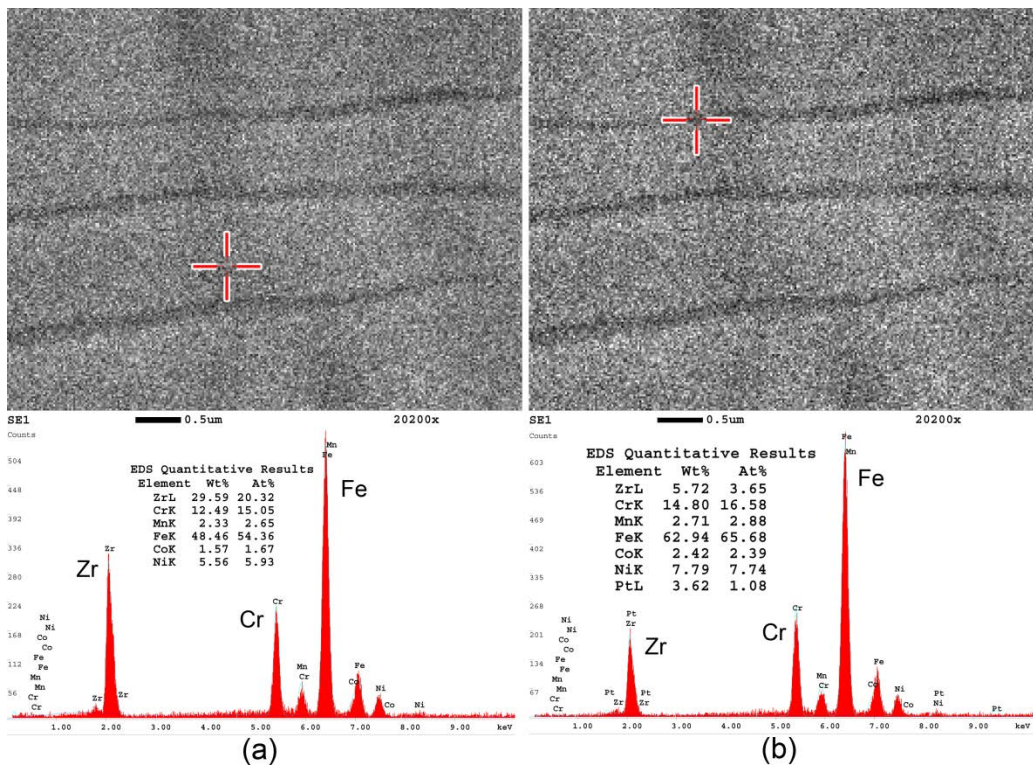nts for comparison purposes. In Figure 5-7a, logarithmic scale was used to cover wide range of ICR values of various coated samples in the same graph. Due to the increasing real contact area between GDL and BPP surfaces, an exponential-like decrease in ICR was observed with increasing compaction pressure as expected. TiN coated samples exhibited lowest level of contact resistance among the reported cases, and it was followed by ZrN, and CrN coated samples. Uncoated samples yielded lower ICR values than CrN coated samples. While the process sequence (formed+coated vs. coated+formed) did not affect the ICR values in TiN and ZrN cases, significant differences were observed in CrN cases.

Area specific contact resistance (ASR) and compaction pressure were calculated based on measured contact area, explained Section 3.2.4., as represented in Figure 5-8. Ranking of the contact resistance values for the samples did not change compared to Figure 5-7. ICR of the samples at 2240 N were presented and statistically compared in next sections. ASR values of coated and formed BPPs based on FEA calculation were presented in Appendix.
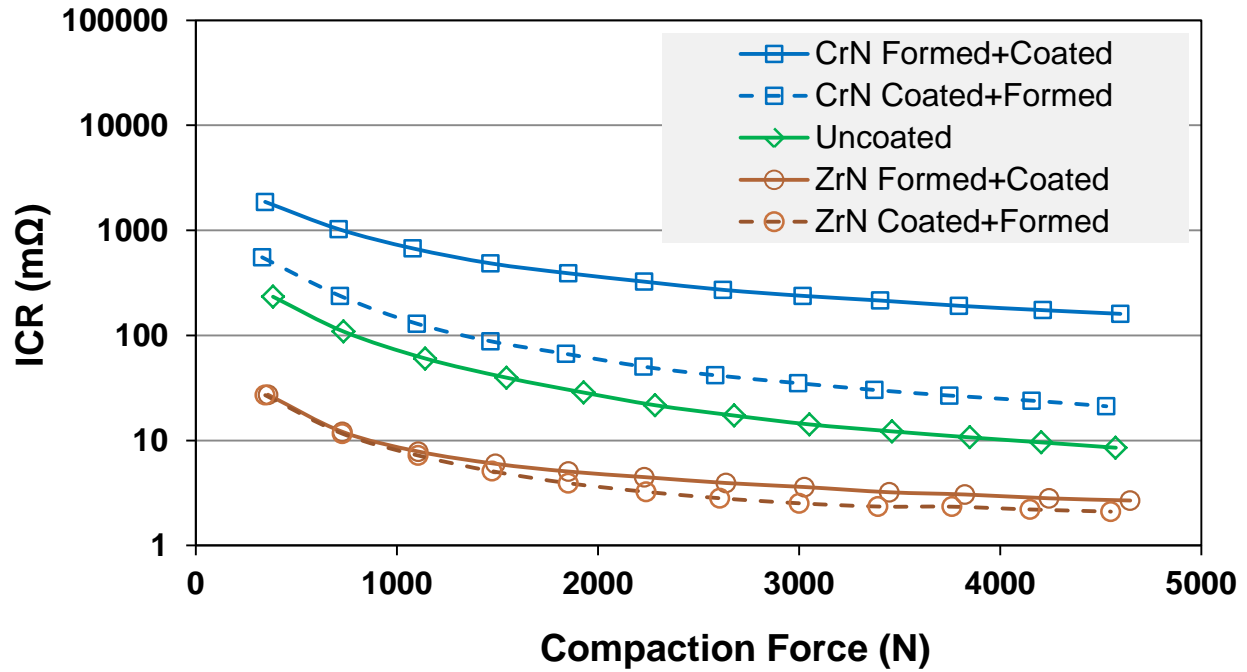
a)
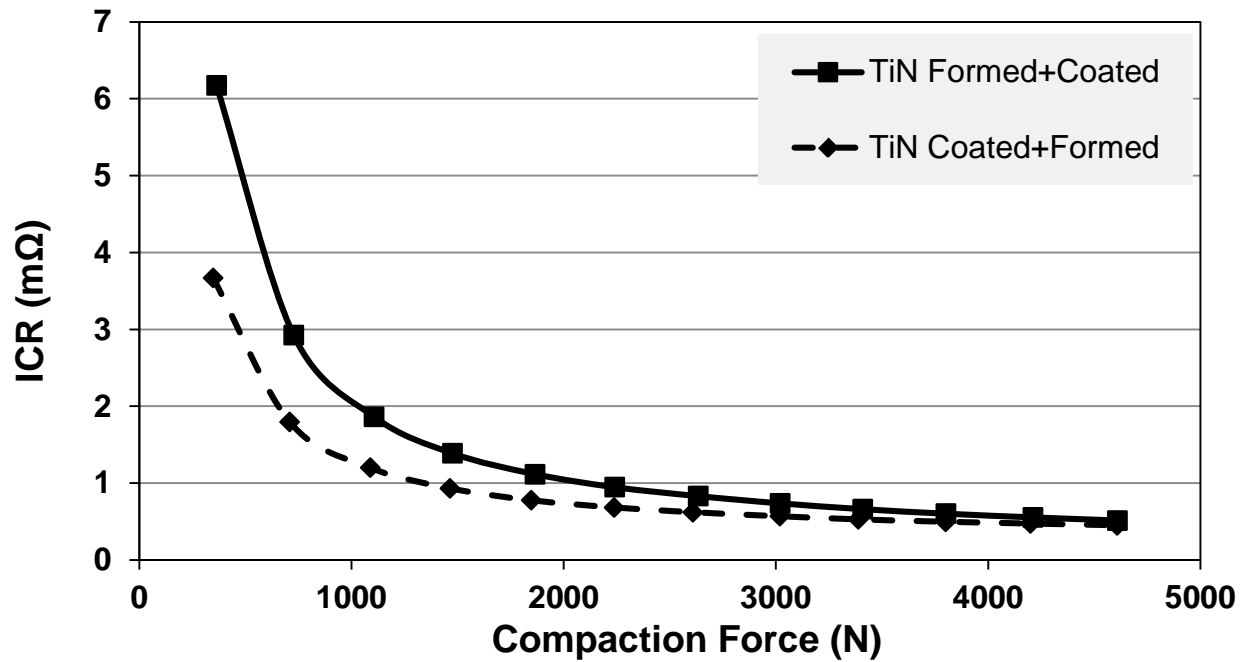
b)

Figure 5-7 ICR evolution of some representative a) CrN and ZrN coated and uncoated, b) TiN coated BPP samples manufactured with two different sequence as function of compaction force (Coating thickness:1 μm, Forming Method: Stamping, Die: 750 μm channel height).
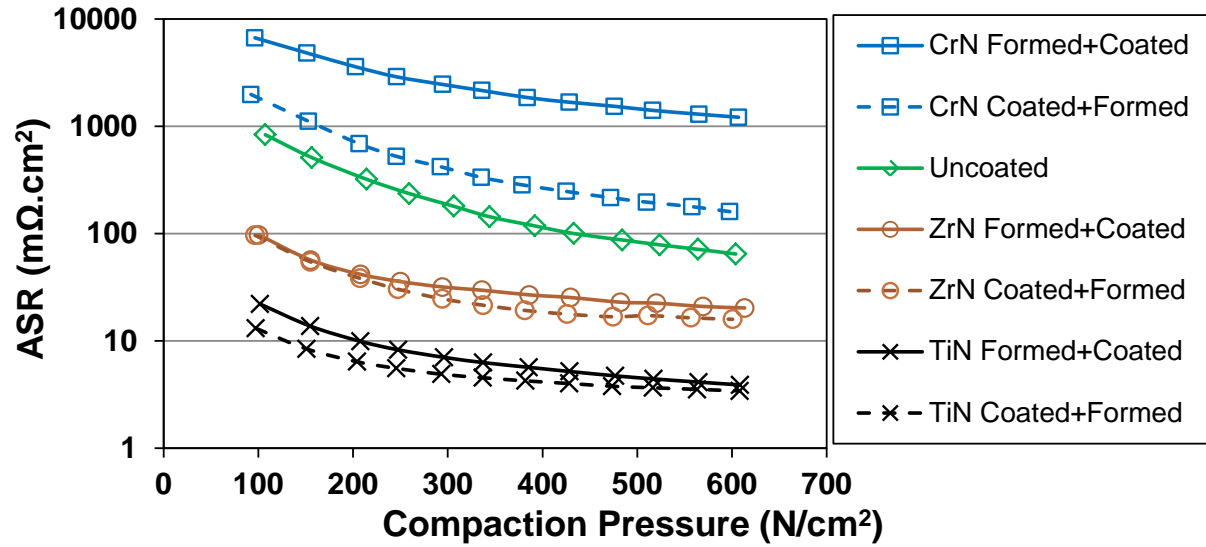
Figure 5-8 ASR evolution of BPP samples manufactured with two different sequence as function of compaction pressure based on contact area measured pressure sensitive film. (Coating thickness: 1 μm, Forming Method: Stamping, Die: 750 μm channel height).

## 5.3.4. Effect of Process Sequence on ICR Before Corrosion test

BPP samples manufactured with two different process sequences namely, formed-then-coated (FtC) and coated-then-formed (CtF) are compared in Figure 5-9. CrN CtF BPP samples gave lower ICR values for all conditions (regardless of forming method, die channel heights and coating thicknesses) than that of FtC BPP samples. ANOVA analyses for 95% confidence interval indicated that differences between these groups are statistically significant except for four cases (* in Figure 5-9, Figure 5-10 and Figure 5-11 indicates that difference between two adjacent column statistically significant). Three out of four cases, which showed insignificant changes, were in 0.1 µm CrN coated samples. ICR differences between BPP samples for the investigated process sequences were more distinct at 1 µm coating thickness. One of the most notable differences between these two groups is that 1 µm CrN FtC forming showed distinctly higher ICR values than 0.1 and 0.5 µm coating cases whereas this difference was not so distinct for FtC BPP samples. This fact can be attributed that semiconducting CrN layers fractured during forming process and permitted more electron to flow in CtF cases. ICR values for all CrN coated samples were found to be too higher than the acceptable levels although they reported as the most corrosion resistant among others [134].

1 µm TiN FtC BPP samples had the best ICR performance among all the tested cases showing under 0.62 mΩ. Differences between two sequences were significant for all 1 µm cases where only one case registered with statistically significant difference among 0.1 and 0.5 µm TiN coated cases. Effect of process sequence was found to be insignificant for ZrN coated samples except two out of 12 cases in stamping. 0.5 and 1 µm coated ZrN samples had relatively similar ICR whereas 0.1 µm coated samples showed markedly higher ICR compared to them.

125

Alaca et al. tested effect of tensile strain on resistivity for Al thin films (400nm) on 152 µm-thick polyimide substrates [207]. They reported steep increase in resistivity by strain because of micro crack formation in Al film. A similar study with 100 nm thick Al films on micrometer-thick polysulfone was reported by Bautista et al., recently [208]. They observed a slight decrease at the beginning of the tensile test and then similar marked increase in resistivity with increasing strain due to cracks occurred in film. Although studies like mentioned above provide information on conductive films on insulating substrate (typical for electronic and electro mechanic applications) relevance of these information to the case in present study is very limited due to different nature of the application. Interest was on through plane electron flow in this study whereas cited studies investigated in plane current mainly.
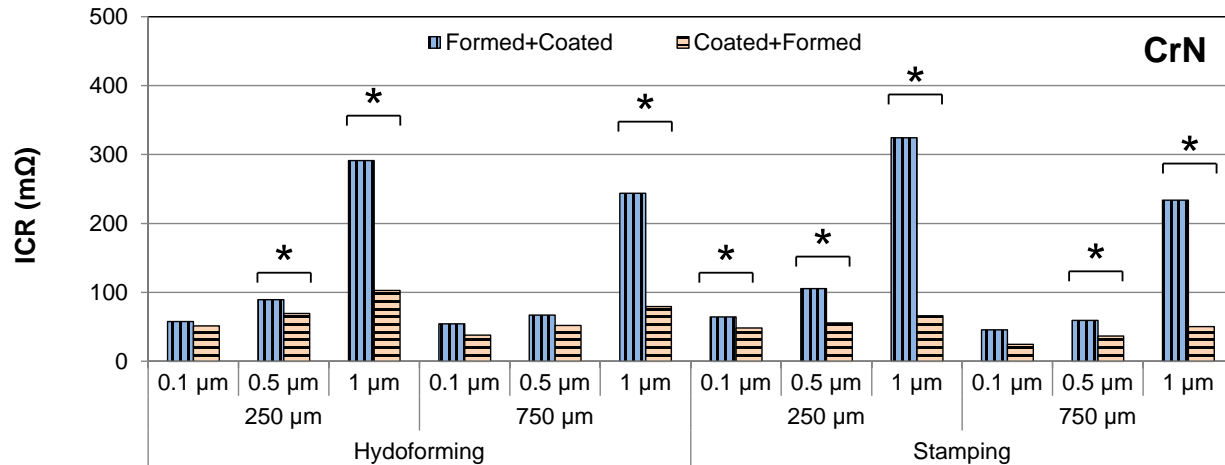
a)
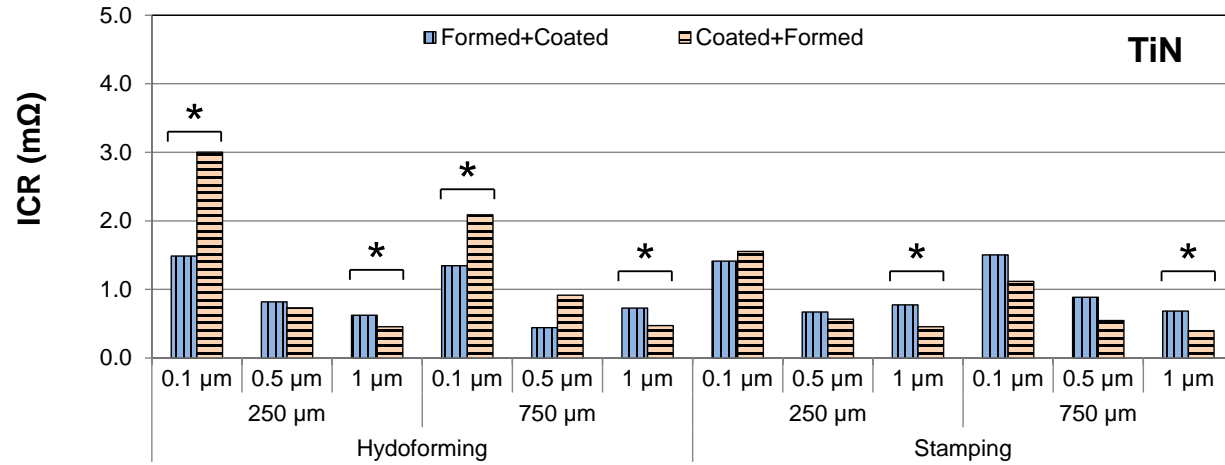
b)
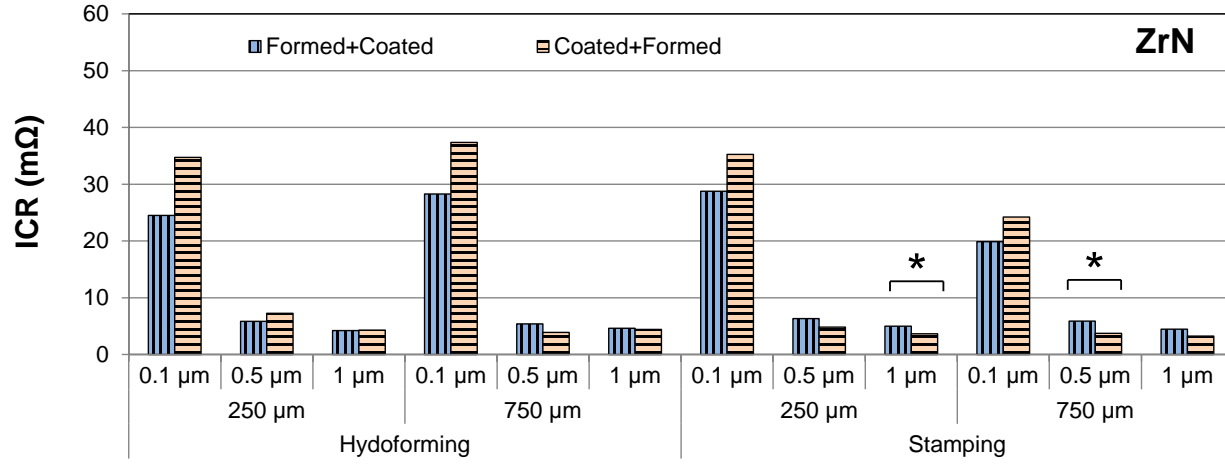
c)

Figure 5-9 ICR of a) CrN, b) TiN, c) ZrN coated BPP samples at 2240N. (For hydroforming and stamping; using 250 and 750 μm feature sized dies; and 0.1, 0.5 and 1 μm coating thicknesses).

127

5.3.5. Effect of Corrosion Exposure on ICR

Effect of corrosion test on ICR values of BBP samples which were coated before and after forming have been investigated and presented in this section. As depicted in Figure 5-10, ICR values of only CrN coated BPP samples significantly decreased in two cases whereas changes for ten remaining cases were found as insignificant. All the ICR values for TiN coated samples increased after corrosion test. Although these increases look markedly in first glance, approximately three fold for 0.1 µm, two fold for 0.5 and 20 percent for 1 µm coating thicknesses, ANOVA showed that changes were statistically significant for only half of the cases due to scattered ICR values obtained especially after corrosion test. Similar to TiN coated BPP samples, ICR for ZrN coated samples increased after corrosion test as well. However, ICR differences between before and after corrosion tests were not distinct, opposed to TiN coated samples, and ANOVA detected statistically significant increases in three out of twelve cases. Decrease in ICR of CrN coated samples can be ascribed that degradation of semiconducting CrN layer increased their conductivity yet CrN coated BPPs had higher ICR values than that of uncoated samples.
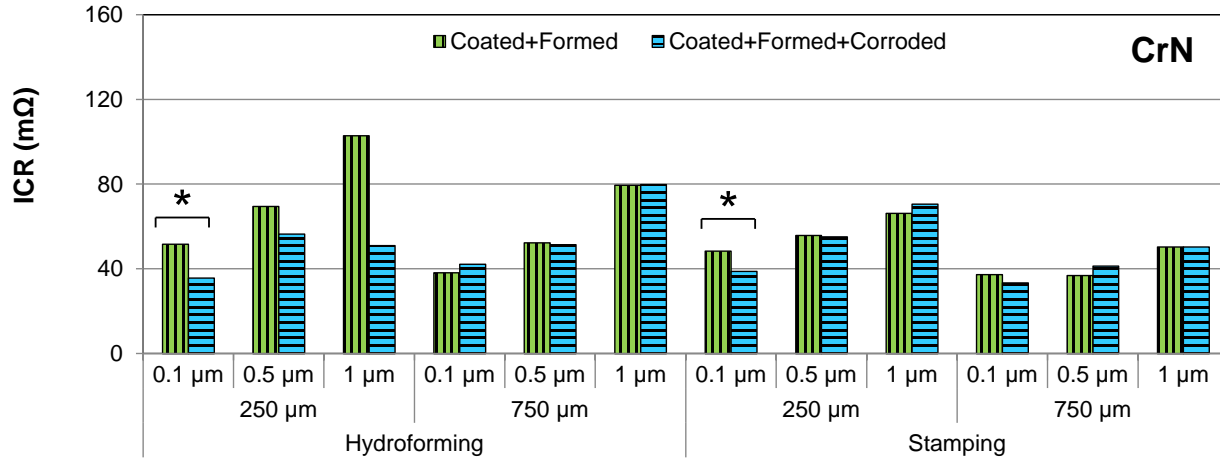
a)
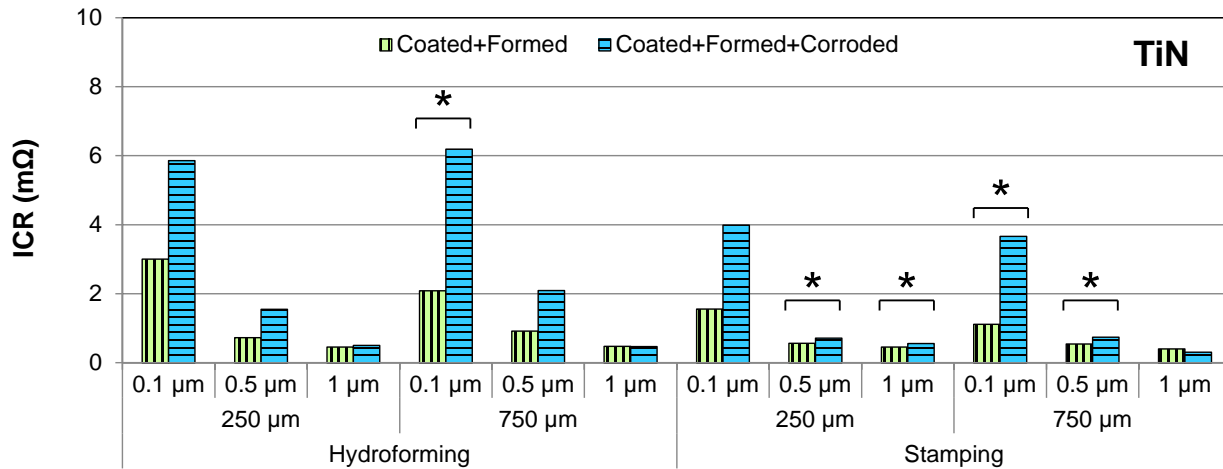
b)
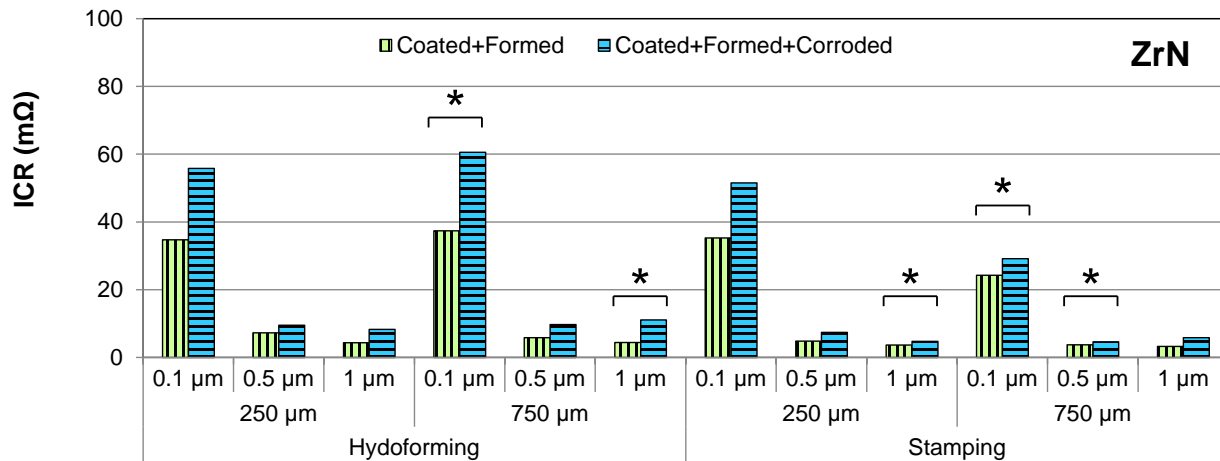
c)

Figure 5-10 ICR values of a) CrN, b) TiN, c) ZrN coated BPP samples at 2240N before and after corrosion test. (* indicates statistically significant difference between two colomns) .

129

5.3.6. Effect of Process Sequence on ICR After Corrosion Exposure

BPP samples manufactured with two different process sequences were compared after they were exposed to 30 minutes potentiodynamic corrosion tests. As a general remark, corrosion resistance of coatings was in descending order of ZrN, CrN and TiN [134]. ICR tests after corrosion exposure revealed that CrN FtC samples showed lower ICR compared to CrN coated BPP samples after forming. In most of the cases, differences between these two groups of samples were found to be statistically significant. Like CrN coated samples, TiN coated BPP samples before forming demonstrated lower ICR values compared to other sequence type. Although obvious ICR value differences between these two sequences were observed, ANOVA detects statistically significant differences between four cases out of twelve because of scattered ICR values. In the case of ZrN coated samples, effect of sequence did not reveal any clear pattern on ICR. All the differences between these two groups were found as statistically insignificant. More stable ICR performance of ZrN coated samples after corrosion test can be attributed to the better corrosion resistance of ZrN compared to CrN and TiN.
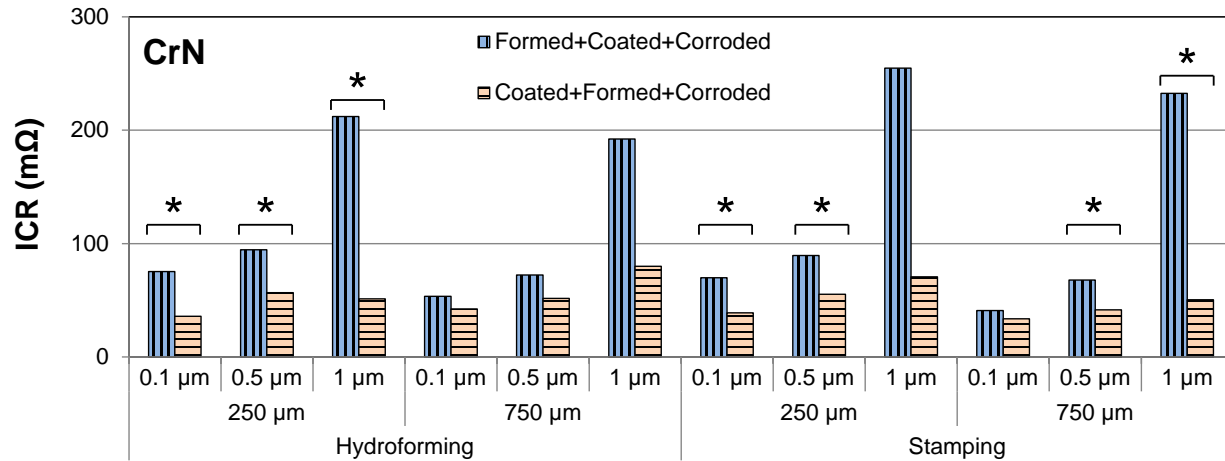
a)
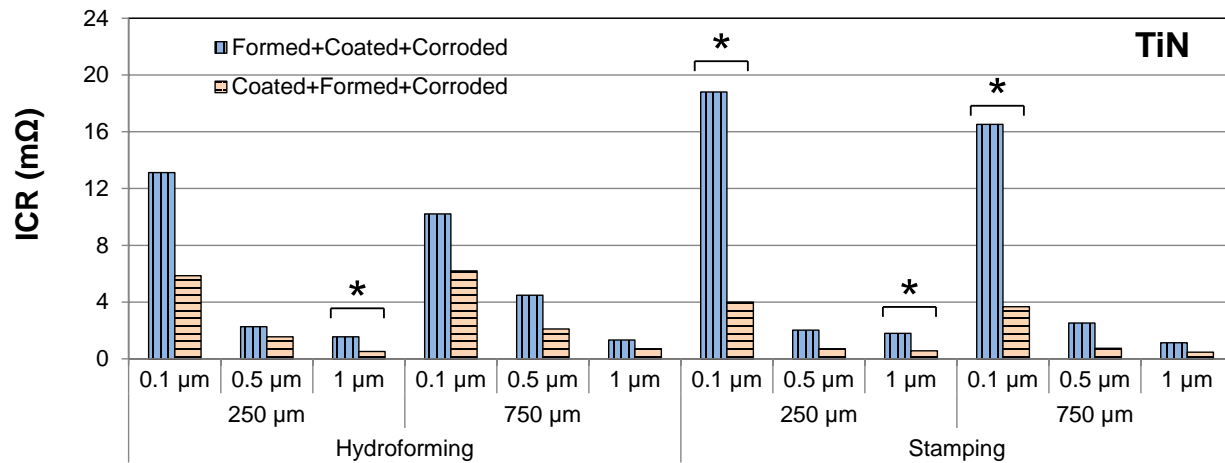
b)
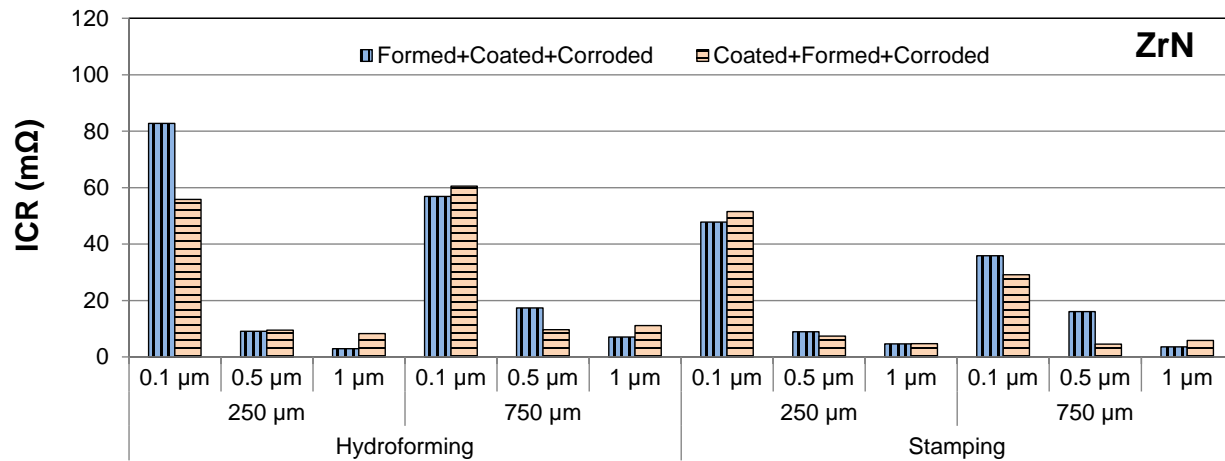
c)

Figure 5-11 ICR values of a) CrN, b) TiN, c) ZrN coated BPP samples manufactured with two different sequences after corrosion test at 2240 N (for hydroforming and stamping; using 250 and 750 µm feature sized dies; and 0.1, 0.5 and 1 µm coating thicknesses).

131

5.4. Conclusion

In this study, effect of process sequence on ICR values measured for CrN, TiN and ZrN coated SS316L BPPs was investigated. Coating application before or after forming process altered the ICR behavior of the metallic bipolar plate samples. In CrN coating case, coating before forming resulted in lower ICR compared to the reverse order, coating after forming. Nevertheless, all the ICR values acquired for the CrN coated samples were extremely higher than required level of BPP materials. TiN coated samples exhibited the best ICR performance in current study meeting DOE targets. Formed-then-coated BPP samples resulted in decreased ICR values than coated-then-formed BPPs. The downside of TiN coated samples was their vulnerability against corrosion exposure. Their ICR values markedly increased after exposure to corrosion. ZrN coated samples showed an improved ICR performance compared to bare SS316L samples as expected from coating applications. Nevertheless, their ICR values were not low enough to meet the DOE target. Process sequence was not significantly effective on ICR behavior of ZrN coated plates for both before and after corrosion test. A vital advantage of ZrN coating was that ZrN coated samples showed similar ICR performance after and before exposure to corrosion conditions. In conclusion, metallic coated-then-formed BPP samples exhibited similar or even better performance than formed-then-coated BPP samples in terms of ICR. Thus, it is concluded that continuous coating of unformed strips prior to forming of BPP samples seemed to be favorable and worth more detailed investigations to realize the cost effective BPP manufacturing for PEMFC applications.

CHAPTER 6: Summary, Scientific Contributions and Suggested Future Study

6.1. Summary of the Findings and Contributions of the Study

The contact resistance of the metallic bipolar plates strongly influences the efficiency and durability of the PEMFCs. Although numerous researchers have studied on contact resistance of bipolar plate metals, this is the only detailed study in open literature dedicated to investigation the effect of manufacturing process on the contact resistance of the metallic BPP. Thus, this study aimed to bring about a broader understanding of manufacturing effects (process, material, coating type, coating thickness, coating and manufacturing process sequence) on the BPP contact resistance. This understanding is expected to help having a complete picture of the performance of the stainless steel bipolar plates manufactured through stamping and hydroforming.

At the first stage of experimental study, stainless steel (SS304 and SS3016L) BPP samples were manufactured under various manufacturing conditions, and then were subjected ICR tests. In general, stamped BPP samples demonstrated higher conductivity (i.e. low ICR) than the hydroformed BPP samples. It can be concluded that manufacturing parameters are effective on ICR performance of metallic BPP. Increasing maximum pressure levels in hydroforming resulted in decreasing ICR values. In addition, BPP samples with larger channel size (750µm) exhibited lower ICR than the BPPs with smaller channel size (250µm). Short term electrochemical corrosion tests decreased ICR values of the BPP samples. Nevertheless, all ICR values recorded during experiments were distinctly higher than acceptable upper limit of DOE target.

133

Upon successful completion of first phase and its findings as well as based on the literature review, coated BPP samples were studied in the second stage. Physical vapor deposition technique was used to coat bipolar plates with CrN, TiN and ZrN coatings at 0.1µm, 0.5µm and 1µm coating thicknesses. Hence, effects of different coatings and coating thickness parameters were studied as manufactured BPPs.

Coating material and thickness were found significant parameters affecting ICR. TiN coated samples revealed the best electrical contact conductivity among the other coating materials. ICR values of TiN coated samples were the only samples group meeting or close to DOE targets. CrN coated samples showed highest ICR. Their values were even higher than uncoated BPP samples. Increasing coating thickness increased ICR values of the CrN coated samples whereas increasing coating thickness decreased ICR of the TiN and ZrN samples. Blank sheets revealed markedly higher ICR values than corresponding formed BPP samples. This result emphasizes the importance of realistic sample geometry to assess BPP materials. Hydroforming process, in comparison to stamping process, delivered slightly lower contact resistant samples. Different die geometries resulted almost same ICR values in hydroforming whereas most of the cases in stamping, smaller channel height dies produced BPP samples with higher ICR. Thus, it can be deduced that manufacturing method and die geometry affected the ICR of the metallic BPP samples although effects of them were not as significant as coating material and coating thickness.

In phase three, effect of process sequence on coated BPPs investigated. When coated metallic materials are preferred for BPP, order of process sequence would be important. Coating of BPPs after forming seems to be reasonable choice since one can expect that forming of coated blanks may deteriorate the surface due to possible deformation of coatings with their brittle

134

characteristics. On the other hand, forming of pre-coated metallic material can increase manufacturing speed of BPPs.

Experiments indicated that applying coating before or after forming process modified ICR behavior of the samples. Contrary to predictions, BPP samples which were coated prior to forming exhibited similar or even better performance than coated after forming samples in terms of ICR. Thus, continuous coating of unformed stripes, then, applying forming process seemed to be favorable and worth further investigation in the quest of making cost effective BPPs for mass production of PEMFC.

6.2. Suggested Future Work

Contributions of present study can be further improved via proposed studies.

Findings of this study can support prospective numerical studies by providing them with necessary experimental data. Thus, more generalized results can help further understanding of relationship between manufacturing process and contact resistance.

A coating found as the best in terms of contact resistance by meeting DOE target in this study were reported with unacceptable corrosion resistance in a connected study. Multi-layer coating has been investigated in PEMFC studies. Effect of manufacturing process on multi-layer coated BPP plates may contribute to bring about proper material and manufacturing method to discover desired performance of metallic BPP with an acceptable cost.

As manufacturing process effective on channel shape and configuration, it not only related with contact resistance but also has impact on mass transportation issues. Proposed works including this multi-physics aspect may contribute to improvement of PEMFC technology.

REFERENCES

[1] Y. Wang, K.S. Chen, J. Mishler, S.C. Cho, X.C. Adroher, A review of polymer electrolyte membrane fuel cells: Technology, applications, and needs on fundamental research, Appl. Energy. 88 (2011) 981-1007.

[2] N. de las Heras, E.P.L. Roberts, R. Langton, D.R. Hodgson, A review of metal separator plate materials suitable for automotive PEM fuel cells, Energy Environ. Sci. 2 (2009) 206-214.

[3] P. Hamilton, B. Pollet, Polymer Electrolyte Membrane Fuel Cell (PEMFC) Flow Field Plate: Design, Materials and Characterisation, Fuel Cells. 10 (2010) 489-509.

[4] H. Wang, J.A. Turner, Reviewing Metallic PEMFC Bipolar Plates, Fuel Cells. 10 (2010) 510-519.

[5] H. Tsuchiya, O. Kobayashi, Mass production cost of PEM fuel cell by learning curve, Int J Hydrogen Energy. 29 (2004) 985-990.

[6] J. Sinha, Y. Yang, Direct Hydrogen PEMFC Manufacturing Cost Estimation for Automotive Applications, 2010 DOE Annual Merit Review. (2010).

[7] X.Z. Yuan, H. Wang, J. Zhang, D.P. Wilkinson, Bipolar Plates for PEM Fuel Cells - From Materials to Processing, J. New. Mat. Electrochem. Systems. 8 (2005) 257-267.

[8] V. Mehta, J.S. Cooper, Review and analysis of PEM fuel cell design and manufacturing, J. Power Sources. 114 (2003) 32-53.

136

[9] J. Wind, R. Späh, W. Kaiser, G. Böhm, Metallic bipolar plates for PEM fuel cells, J. Power Sources. 105 (2002) 256-260.

[10] A.J. Appleby, Fuel cell technology: Status and future prospects, Energy. 21 (1996) 521-653.

[11] A. Hermann, T. Chaudhuri, P. Spagnol, Bipolar plates for PEM fuel cells: A review, Int J Hydrogen Energy. 30 (2005) 1297-1302.

[12] H. Tawfik, Y. Hung, D. Mahajan, Metal bipolar plates for PEM fuel cell: A review, J. Power Sources. 163 (2007) 755-767.

[13] Y. Shao, G. Yin, Z. Wang, Y. Gao, Proton exchange membrane fuel cell from low temperature to high temperature: Material challenges, J. Power Sources. 167 (2007) 235-242.

[14] H. Wang, M.A. Sweikart, J.A. Turner, Stainless steel as bipolar plate material for polymer electrolyte membrane fuel cells, J. Power Sources. 115 (2003) 243-251.

[15] S. Lee, C. Huang, Y. Chen, Investigation of PVD coating on corrosion resistance of metallic bipolar plates in PEM fuel cell, J. Mater. Process. Technol. 140 (2003) 688-693.

[16] S.J. Lee, C.H. Huang, Y.P. Chen, C.T. Hsu, PVD Coated Bipolar Plates for PEM Fuel Cells, Journal of Fuel Cell Science and Technology. 2 (2005) 290-294.

[17] B. Cunningham, D.G. Baird, The development of economical bipolar plates for fuel cells, Journal of Materials Chemistry. 16 (2006) 4385-4388.

[18] H. Wang, J.A. Turner, Anodic behavior of high nitrogen-bearing steels in PEMFC environments, J. Power Sources. 180 (2008) 791-796.

137

[19] R. Tian, J. Sun, J. Wang, Study on behavior of plasma nitrided 316L in PEMFC working conditions, Int J Hydrogen Energy. 33 (2008) 7507-7512.

[20] Y. Wang, D.O. Northwood, Life-Limiting Aspects of the Corrosion of Metallic Bipolar Plates for PEM Fuel Cells, Advanced Materials Research. 41 (2008) 469-475.

[21] J. André, L. Antoni, J.P. Petit, Corrosion resistance of stainless steel bipolar plates in a PEFC environment: A comprehensive study, Int J Hydrogen Energy. 35 (2010) 3684-3697.

[22] J. André, L. Antoni, J. Petit, E. De Vito, A. Montani, Electrical contact resistance between stainless steel bipolar plate and carbon felt in PEFC: A comprehensive study, Int J Hydrogen Energy. 34 (2009) 3125-3133.

[23] R.A. Antunes, M.C.L. Oliveira, G. Ett, V. Ett, Corrosion of metal bipolar plates for PEM fuel cells: A review, Int J Hydrogen Energy. 35 (2010) 3632-3647.

[24] A. Heinzel, F. Mahlendorf, C. Jansen, FUEL CELLS - PROTON-EXCHANGE MEMBRANE FUEL CELLS | Bipolar Plates, in: Jürgen Garche (Ed.), Encyclopedia of Electrochemical Power Sources, Elsevier, Amsterdam, 2009, pp. 810-816.

[25] M.P. Brady, K. Weisbrod, I. Paulauskas, R.A. Buchanan, K.L. More, H. Wang, M. Wilson, F. Garzon, L.R. Walker, Preferential thermal nitridation to form pin-hole free Cr-nitrides to protect proton exchange membrane fuel cell metallic bipolar plates, Scr. Mater. 50 (2004) 1017-1022.

[26] S. Joseph, J. McClure, R. Chianelli, P. Pich, P. Sebastian, Conducting polymer-coated stainless steel bipolar plates for proton exchange membrane fuel cells (PEMFC), Int J Hydrogen Energy. 30 (2005) 1339-1344.

[27] R.C. Makkus, A.H.H. Janssen, F.A. de Bruijn, R.K.A.M. Mallant, Use of stainless steel for cost competitive bipolar plates in the SPFC, J. Power Sources. 86 (2000) 274-282.

[28] E.A. Cho, U.S. Jeon, S.-. Hong, I.H. Oh, S.G. Kang, Performance of a 1 kW-class PEMFC stack using TiN-coated 316 stainless steel bipolar plates, J. Power Sources. 142 (2005) 177-183.

[29] United States Department of Energy, Energy Efficiency and Renewable Energy, Fuel Cell Technologies Program, "2007 Technical Plan – Fuel Cells" web site:, http://www1.eere.energy.gov/hydrogenandfuelcells/mypp/pdfs/fuel_cells.pdf, 2011.

[30] E.J. Carlson, P. Kopf, J. Sinha, S. Sriramulu, Y. Yang, Cost Analysis of PEM Fuel Cells for Transportation, NREL/SR-560-39104 (2005).

[31] J. Wind, A. LaCroix, S. Braeuninger, P. Hedrich, C. Heller, M. Schudy, Metal bipolar plates and coatings, in: W. Vielstich, H.A. Gasteiger, A. Lamm, H. Yokokawa (Eds.), Handbook of Fuel Cells, John Wiley & Sons, Ltd, 2010.

[32] S. Mahabunphachai, Ö.N. Cora, M. Koç, Effect of manufacturing processes on formability and surface topography of proton exchange membrane fuel cell metallic bipolar plates, J. Power Sources. 195 (2010) 5269-5277.

139

[33] S.J. Lee, K.T. Yang, Y.M. Lee, C.Y. Lee, The Resistive Properties of Proton Exchange Membrane Fuel Cells With Stainless Steel Bipolar Plates, Journal of Fuel Cell Science and Technology. 7 (2010) 041004-1-041004-5.

[34] D.J.L. Brett, N.P. Brandon, Review of Materials and Characterization Methods for Polymer Electrolyte Fuel Cell Flow-Field Plates, Journal of Fuel Cell Science and Technology. 4 (2007) 29-44.

[35] M.P. Brady, H. Wang, J. Turner, H.M. Meyer III, K.L. More, P.F. Tortorelli, B.D. McCarthy, Pre-Oxidized and Nitrided Stainless Steel Foil for Proton Exchange Membrane Fuel Cell Bipolar Plates: Part 1 Corrosion, Interfacial Contact Resistance, and Surface Structure, J. Power Sources. 195 (2010) 5610-5618.

[36] L. Freris, D. Infield, Renewable Energy in Power Systems, Wiley, 2008.

[37] International Energy Agency (IEA), Key World Energy Statistics 2010, http://www.iea.org/textbase/nppdf/free/2010/key_stats_2010.pdf, (2010).

[38] F. Barbir, Transition to renewable energy systems with hydrogen as an energy carrier, Energy. 34 (2009) 308-312.

[39] T.N. Veziroglu, 21st century's energy: hydrogen energy system, Energy conversion and management. 49 (2008) 1820-1831.

[40] M.K. Hubbert, Nuclear Energy and the Fossil Fuel, Drilling and production practice. (1956).

[41] C.J. Campbell, J.H. Laherrère, The end of cheap oil, Sci. Am. 278 (1998) 60-65.

140

[42] A. Verbruggen, M. Al Marchohi, Views on peak oil and its relation to climate change policy, Energy Policy. 38 (2010) 5572-5581.

[43] European Commission, Green Paper - Towards a European strategy for the security of energy supply, (2000).

[44] S. Solomon, G. Plattner, R. Knutti, P. Friedlingstein, Irreversible climate change due to carbon dioxide emissions, Proceedings of the National Academy of Sciences. 106 (2009) 1704-1709.

[45] P.M. Cox, R.A. Betts, C.D. Jones, S.A. Spall, I.J. Totterdell, Acceleration of global warming due to carbon-cycle feedbacks in a coupled climate model, Nature. 408 (2000) 184-187.

[46] F. Barbir, PEM Fuel Cells: Theory and Practice. Elsevier Academic Press, New York, 2005.

[47] J. Larminie, A. Dicks, Fuel Cell Systems Explained, John Wiley and Sons Ltd., West Sussex, 2003.

[48] W. Grove, On a New Voltaic Battery, and on Voltaic Combinations and Arrange-ments', Phil.Mag. 15 (1839) 287-293.

[49] C.F. Schönbein, Beobachtungen über chemische Veränderungen, welche Salpetersäure, Weingeist und Aether unter dem gedoppelten Einflusse des Volta'schen Stromes und des Platins erleiden, Annalen der Physik. 123 (1839) 563-583.

[50] Y. Wang, L. Pham, G.P.S.d. Vasconcellos, M. Madou, Fabrication and characterization of micro PEM fuel cells using pyrolyzed carbon current collector plates, J. Power Sources. 195 (2010) 4796-4803.

[51] K. Sopian, W.R. Wan Daud, Challenges and future developments in proton exchange membrane fuel cells, Renewable Energy. 31 (2006) 719-727.

[52] Y. Wang, K.S. Chen, J. Mishler, S.C. Cho, X.C. Adroher, A review of polymer electrolyte membrane fuel cells: Technology, applications, and needs on fundamental research, Appl. Energy. 88 (2011) 981-1007.

[53] List of fuel cell powered automobiles., (http://www.fuelcells.org/info/charts/carchart.pdf), 2011 (2011) 8.

[54] S. Campanari, G. Manzolini, F. Garcia de la Iglesia, Energy analysis of electric vehicles using batteries or fuel cells through well-to-wheel driving cycle simulations, J. Power Sources. 186 (2009) 464-477.

[55] X. Li, J. Li, L. Xu, F. Yang, J. Hua, M. Ouyang, Performance analysis of proton-exchange membrane fuel cell stacks used in Beijing urban-route buses trial project, Int J Hydrogen Energy. 35 (2010) 3841-3847.

[56] J. Gangi, Fuel Cell-Powered Forklifts: Raising the Bar, Industrial Utility Vehicle & Mobile Equipment. May/June (2008).

[57] L.L. Gaines, A. Elgowainy, M.Q. Wang, Full fuel-cycle comparison of forklift propulsion systems. Argonne National Laboratory (ANL). (2008).

142

[58] F. Dundar, E. Dur, S. Mahabunphachai, M. Koç, Corrosion resistance characteristics of stamped and hydroformed proton exchange membrane fuel cell metallic bipolar plates, J. Power Sources. 195 (2010) 3546-3552.

[59] E. Dur, Ö.N. Cora, M. Koç, Effect of manufacturing conditions on the corrosion resistance behavior of metallic bipolar plates in proton exchange membrane fuel cells, J. Power Sources. 196 (2011) 1235-1241.

[60] C. Turan, E. Dur, M.F. Peker, O.N. Cora, M. Koc, Corrosion, Contact Resistance, and Surface Characteristics of Stamped and Hydroformed Metallic Bipolar Plates for PEMFC, in Proceedings of FUELCELL2010, The 8th International Conference on Fuel Cell Science, Engineering and Technology, June 14-16, 2010, Brooklyn, New York, USA, 2010 545-553.

[61] M. Koç, S. Mahabunphachai, Feasibility investigations on a novel micro-manufacturing process for fabrication of fuel cell bipolar plates: Internal pressure-assisted embossing of micro-channels with in-die mechanical bonding, J. Power Sources. 172 (2007) 725-733.

[62] S. Mahabunphachai, M. Koç, Investigation of size effects on material behavior of thin sheet metals using hydraulic bulge testing at micro/meso-scales, Int. J. Mach. Tools Manuf. 48 (2008) 1014-1029.

[63] S. Mahabunphachai, M. Koç, Fabrication of micro-channel arrays on thin metallic sheet using internal fluid pressure: Investigations on size effects and development of design guidelines, J. Power Sources. 175 (2008) 363-371.

143

[64] R. Hornung, G. Kappelt, Bipolar plate materials development using Fe-based alloys for solid polymer fuel cells, J. Power Sources. 72 (1998) 20-21.

[65] D.P. Davies, P.L. Adcock, M. Turpin, S.J. Rowen, Bipolar plate materials for solid polymer fuel cells, Journal of Applied Electrochemistry. 30 (2000) 101-105.

[66] A. Kraytsberg, M. Auinat, Y. Ein-Eli, Reduced contact resistance of PEM fuel cell's bipolar plates via surface texturing, J. Power Sources. 164 (2007) 697-703.

[67] T. Fukutsuka, T. Yamaguchi, S. Miyano, Y. Matsuo, Y. Sugie, Z. Ogumi, Carbon-coated stainless steel as PEFC bipolar plate material, J. Power Sources. 174 (2007) 199-205.

[68] Y. Show, Electrically conductive amorphous carbon coating on metal bipolar plates for PEFC, Surface and Coatings Technology. 202 (2007) 1252-1255.

[69] M. Li, S. Luo, C. Zeng, J. Shen, H. Lin, C. Cao, Corrosion behavior of TiN coated type 316 stainless steel in simulated PEMFC environments, Corros. Sci. 46 (2004) 1369-1380.

[70] Y. Wang, D.O. Northwood, An investigation into TiN-coated 316L stainless steel as a bipolar plate material for PEM fuel cells, J. Power Sources. 165 (2007) 293-298.

[71] Y. Wang, D.O. Northwood, An investigation of the electrochemical properties of PVD TiN-coated SS410 in simulated PEM fuel cell environments, Int J Hydrogen Energy. 32 (2007) 895-902.

[72] R. Tian, J. Sun, L. Wang, Plasma-nitrided austenitic stainless steel 316L as bipolar plate for PEMFC, Int J Hydrogen Energy. 31 (2006) 1874-1878.

144

[73] H. Lee, S. Lee, J. Kim, M. Kim, D. Wee, Thermally nitrided Cu–5.3Cr alloy for application as metallic separators in PEMFCs, Int J Hydrogen Energy. 33 (2008) 4171-4177.

[74] H. Wang, M.P. Brady, G. Teeter, J. Turner, Thermally nitrided stainless steels for polymer electrolyte membrane fuel cell bipolar plates: Part 1: Model Ni-50Cr and austenitic 349 (TM) alloys, J. Power Sources. 138 (2004) 86-93.

[75] Y. Wang, D.O. Northwood, Effects of O_2 and H_2 on the corrosion of SS316L metallic bipolar plate materials in simulated anode and cathode environments of PEM fuel cells, Electrochim. Acta. 52 (2007) 6793-6798.

[76] H. Wang, M.P. Brady, K.L. More, H.M. Meyer III, J.A. Turner, Thermally nitrided stainless steels for polymer electrolyte membrane fuel cell bipolar plates: Part 2: Beneficial modification of passive layer on AISI446, J. Power Sources. 138 (2004) 79-85.

[77] C. Chung, S. Chen, P. Chiu, M. Chang, T. Hung, T. Ko, Carbon film-coated 304 stainless steel as PEMFC bipolar plate, J. Power Sources. 176 (2008) 276-281.

[78] A. Taniguchi, K. Yasuda, Highly water-proof coating of gas flow channels by plasma polymerization for PEM fuel cells, J. Power Sources. 141 (2005) 8-12.

[79] M. Brady, B. Yang, H. Wang, J. Turner, K. More, M. Wilson, F. Garzon, The formation of protective nitride surfaces for PEM fuel cell metallic bipolar plates, JOM. 58 (2006) 50-57.

[80] M.P. Brady, K. Weisbrod, C. Zawodzinski, I. Paulauskas, R.A. Buchanan, L.R. Walker, Assessment of thermal nitridation to protect metal bipolar plates in polymer electrolyte membrane fuel cells, Electrochemical and solid-state letters. 5 (2002) A245-A247.

145

[81] T.J. Toops, M.P. Brady, P.F. Tortorelli, J.A. Pihl, F. Estevez, D. Connors, F. Garzon, T. Rockward, D. Gervasio, W. Mylan, S.H. Kosaraju, Pre-oxidized and nitrided stainless steel alloy foil for proton exchange membrane fuel cell bipolar plates. Part 2: Single-cell fuel cell evaluation of stamped plates, J. Power Sources. 195 (2010) 5619-5627.

[82] L. Ma, S. Warthesen, D. Shores, Evaluation of materials for bipolar plates in PEMFCs, Journal of new Materials for Electrochemical Systems. 3 (2000) 221-228.

[83] P.L. Hentall, J.B. Lakeman, G.O. Mepsted, P.L. Adcock, J.M. Moore, New materials for polymer electrolyte membrane fuel cell current collectors, J. Power Sources. 80 (1999) 235-241.

[84] M. Kumagai, S. Myung, R. Asaishi, Y. Sun, H. Yashiro, Nanosized TiN–SBR hybrid coating of stainless steel as bipolar plates for polymer electrolyte membrane fuel cells, Electrochim. Acta. 54 (2008) 574-581.

[85] I.E. Paulauskas, M.P. Brady, H.M. Meyer III, R.A. Buchanan, L.R. Walker, Corrosion behavior of CrN, Cr2N and π phase surfaces on nitrided Ni–50Cr for proton exchange membrane fuel cell bipolar plates, Corros. Sci. 48 (2006) 3157-3171.

[86] R. Silva, A. Pozio, Corrosion study on different types of metallic bipolar plates for polymer electrolyte membrane fuel cells, Journal of fuel cell science and technology. 4 (2007) 116-122.

[87] R.F. Silva, D. Franchi, A. Leone, L. Pilloni, A. Masci, A. Pozio, Surface conductivity and stability of metallic bipolar plate materials for polymer electrolyte fuel cells, Electrochim. Acta. 51 (2006) 3592-3598.

146

[88] A. Pozio, R.F. Silva, A. Masci, Corrosion study of SS430/Nb as bipolar plate materials for PEMFCs, Int J Hydrogen Energy. 33 (2008) 5697-5702.

[89] N.D. Nam, J.G. Kim, Electrochemical Behavior of CrN Coated on 316L Stainless Steel in Simulated Cathodic Environment of Proton Exchange Membrane Fuel Cell, Japanese journal of applied physics. 47 (2008) 6887-6890.

[90] W. Yoon, X. Huang, P. Fazzino, K.L. Reifsnider, M.A. Akkaoui, Evaluation of coated metallic bipolar plates for polymer electrolyte membrane fuel cells, J. Power Sources. 179 (2008) 265-273.

[91] J. Barranco, F. Barreras, A. Lozano, A.M. Lopez, V. Roda, J. Martin, M. Maza, G.G. Fuentes, E. Almandoz, Cr and Zr/Cr nitride CAE-PVD coated aluminum bipolar plates for polymer electrolyte membrane fuel cells, Int J Hydrogen Energy. 35 (2010) 11489-11498.

[92] B. Avasarala, P. Haldar, Effect of surface roughness of composite bipolar plates on the contact resistance of a proton exchange membrane fuel cell, J. Power Sources. 188 (2009) 225-229.

[93] T. Matsuura, M. Kato, M. Hori, Study on metallic bipolar plate for proton exchange membrane fuel cell, J. Power Sources. 161 (2006) 74-78.

[94] D. Liu, X. Lai, J. Ni, L. Peng, S. Lan, Z. Lin, Robust design of assembly parameters on membrane electrode assembly pressure distribution, J. Power Sources. 172 (2007) 760-767.

[95] D. Liu, L. Peng, X. Lai, Effect of dimensional error of metallic bipolar plate on the GDL pressure distribution in the PEM fuel cell, Int J Hydrogen Energy. 34 (2009) 990-997.

147

[96] C.K. Jin, C.G. Kang, Fabrication process analysis and experimental verification for aluminum bipolar plates in fuel cells by vacuum die-casting, J. Power Sources. 196 (2011) 8241-8249.

[97] J. Shang, L. Wilkerson, S. Hatkevich, G.S. Daehn, Commercialization of Fuel Cell Bipolar Plate Manufacturing by Electromagnetic Forming, 4th International Conference on High Speed Forming. (2010) 47-56.

[98] T. Chen, J. Ye, A micro-stamping process analysis of metallic bipolar plates channel, Nano/Micro Engineered and Molecular Systems (NEMS), 2011 IEEE International Conference on. (2011) 597-602.

[99] D.J. Wheeler, G. Sverdrup, 2007 Status of Manufacturing: Polymer Electrolyte Membrane (PEM) Fuel Cells, National Renewable Energy Laboratory, 2008.

[100] Y. Park, S. Lee, S. Kim, S. Lim, D. Jung, K. Park, S. Choi, J. Kim, D. Peck, Corrosion properties and cell performance of CrN/Cr-coated stainless steel 316L as a metal bipolar plate for a direct methanol fuel cell, Electrochim. Acta. 56 (2011) 7602-7609.

[101] L. Peng, X. Lai, D. Liu, P. Hu, J. Ni, Flow channel shape optimum design for hydroformed metal bipolar plate in PEM fuel cell, J. Power Sources. 178 (2008) 223-230.

[102] L. Peng, P. Hu, X. Lai, D. Mei, J. Ni, Investigation of micro/meso sheet soft punch stamping process – simulation and experiments, Mater Des. 30 (2009) 783-790.

148

[103] L. Peng, D. Liu, P. Hu, X. Lai, J. Ni, Fabrication of Metallic Bipolar Plates for Proton Exchange Membrane Fuel Cell by Flexible Forming Process-Numerical Simulations and Experiments, J. Fuel Cell Sci. Technol. 7 (2010) 031009-9.

[104] L. Peng, X. Lai, P. Yi, J. Mai, J. Ni, Design, Optimization, and Fabrication of Slotted-Interdigitated Thin Metallic Bipolar Plates for PEM Fuel Cells, J. Fuel Cell Sci. Technol. 8 (2011) 011002-8.

[105] W.D. CALLISTER, Fundamentals of Materials Science and Engineering, 5th Ed., Pg.367, John Wiley & Sons, Inc., New York, 2001.

[106] R.E. Hummel, Electronic Properties of Materials, Springer Verlag, 2011.

[107] Y.H. Cheng, B.K. Tay, S.P. Lau, Electrical properties of TiN films deposited by filtered cathodic vacuum arc, J. Vac. Sci. Technol. B. 20 (2002) 2000-2006.

[108] G.Q. Yu, B.K. Tay, S.P. Lau, K. Prasad, L.K. Pan, J.W. Chai, D. Lai, Effects of N ion energy on titanium nitride films deposited by ion assisted filtered cathodic vacuum arc, Chemical Physics Letters. 374 (2003) 264-270.

[109] M. Ohring, Engineering Materials Science, Academic Pr, 1995.

[110] K. Fuchs, The conductivity of thin metallic films according to the electron theory of metals, Mathematical Proceedings of the Cambridge Philosophical Society. 34 (1938) 100.

[111] E.H. Sondheimer, The mean free path of electrons in metals, Adv. Phys. 1 (1952) 1-42.

149

[112] A.F. Mayadas, M. Shatzkes, Electrical-Resistivity Model for Polycrystalline Films: the Case of Arbitrary Reflection at External Surfaces, Phys. Rev. B. 1 (1970) 1382-1389.

[113] A. Bendavid, P.J. Martin, R.P. Netterfield, T.J. Kinder, The properties of TiN films deposited by filtered arc evaporation, Surface and Coatings Technology. 70 (1994) 97-106.

[114] T. Sun, B. Yao, A.P. Warren, K. Barmak, M.F. Toney, R.E. Peale, K.R. Coffey, Dominant role of grain boundary scattering in the resistivity of nanometric Cu films, Phys. Rev. B. 79 (2009) 041402.

[115] S. Kanamori, Investigation of reactively sputtered TiN films for diffusion barriers, Thin Solid Films. 136 (1986) 195-214.

[116] R. Holm, E. Holm, Electric Contacts Handbook, Springer, 1958.

[117] Y.V. Sharvin, A Possible Method for Studying Fermi Surfaces, Soviet Physics Jetp-Ussr. 21 (1965) 655-659.

[118] L. Kogut, K. Komvopoulos, Electrical contact resistance theory for conductive rough surfaces, J. Appl. Phys. 94 (2003) 3153-3162.

[119] Y. Zhou, G. Lin, A.J. Shih, S.J. Hu, A micro-scale model for predicting contact resistance between bipolar plate and gas diffusion layer in PEM fuel cells, J. Power Sources. 163 (2007) 777-783.

150

[120] Z. Wu, Y. Zhou, G. Lin, S. Wang, S.J. Hu, An improved model for predicting electrical contact resistance between bipolar plate and gas diffusion layer in proton exchange membrane fuel cells, J. Power Sources. 182 (2008) 265-269.

[121] P. Zhou, P. Lin, C.W. Wu, Z. Li, Effect of nonuniformity of the contact pressure distribution on the electrical contact resistance in proton exchange membrane fuel cells, Int J Hydrogen Energy. 36 (2011) 6039-6044.

[122] V. Mishra, F. Yang, R. Pitchumani, Measurement and prediction of electrical contact resistance between gas diffusion layers and bipolar plate for applications to PEM fuel cells, Journal of Fuel Cell Science and Technology. 1 (2004) 1-9.

[123] X. Yan, M. Hou, H. Zhang, F. Jing, P. Ming, B. Yi, Performance of PEMFC stack using expanded graphite bipolar plates, J. Power Sources. 160 (2006) 252-257.

[124] E.A. Cho, U.-. Jeon, H.Y. Ha, S.-. Hong, I.-. Oh, Characteristics of composite bipolar plates for polymer electrolyte membrane fuel cells, J. Power Sources. 125 (2004) 178-182.

[125] T. Ferreira, W. Rasband, The ImageJ User Guide-Version 1.43, US National Institutes of Health, Bethesda, Maryland, USA. Available on World Wide Web at http://rsb. info. nih. gov/ij. (2010).

[126] P. Zhou, C.W. Wu, Numerical study on the compression effect of gas diffusion layer on PEMFC performance, J. Power Sources. 170 (2007) 93-100.

[127] S. Miachon, P. Aldebert, Internal hydration H2/O2 100 cm2 polymer electrolyte membrane fuel cell, J. Power Sources. 56 (1995) 31-36.

151

[128] J. Jayaraj, Y.C. Kim, H.K. Seok, K.B. Kim, E. Fleury, Development of metallic glasses for bipolar plate application, Materials Science and Engineering: A. 449-451 (2007) 30-33.

[129] A. Kumar, R.G. Reddy, Effect of channel dimensions and shape in the flow-field distributor on the performance of polymer electrolyte membrane fuel cells, J. Power Sources. 113 (2003) 11-18.

[130] J. Scholta, G. Escher, W. Zhang, L. Küppers, L. Jörissen, W. Lehnert, Investigation on the influence of channel geometries on PEMFC performance, J. Power Sources. 155 (2006) 66-71.

[131] K.T. Cho, M.M. Mench, Coupled effects of flow field geometry and diffusion media material structure on evaporative water removal from polymer electrolyte fuel cells, Int J Hydrogen Energy. 35 (2010) 12329-12340.

[132] J. André, Effect on the contact resistance of the ageing of metallic bipolar plates for PEMFC, (2006).

[133] C. Turan, Ö.N. Cora, M. Koç, Effect of manufacturing processes on contact resistance characteristics of metallic bipolar plates in PEM fuel cells, Int J Hydrogen Energy. 36 (2011) 12370-12380.

[134] E. Dur, Ö.N. Cora, M. Koç, Experimental investigations on the corrosion resistance characteristics of coated metallic bipolar plates for PEMFC, Int J Hydrogen Energy. 36 (2011) 7162-7173.

[135] H.S. Seo, T.Y. Lee, I. Petrov, J.E. Greene, D. Gall, Epitaxial and polycrystalline HfN layers on MgO (001): Film growth and physical properties, J. Appl. Phys. 97 (2005) 083521.

152

[136] H.M. Benia, M. Guemmaz, G. Schmerber, A. Mosser, J.C. Parlebas, Optical and electrical properties of sputtered ZrN compounds, Catalysis Today. 89 (2004) 307-312.

[137] C.S. Chen, C.P. Liu, H.G. Yang, C.Y.A. Tsao, Influence of the preferred orientation and thickness of zirconium nitride films on the diffusion property in copper, Journal of Vacuum Science & Technology B: Microelectronics and Nanometer Structures. 22 (2004) 1075.

[138] B.O. Johansson, J.-. Sundgren, J.E. Greene, A. Rockett, S.A. Barnett, Growth and properties of single crystal TiN films deposited by reactive magnetron sputtering, Journal of Vacuum Science & Technology A: Vacuum, Surfaces, and Films. 3 (1985) 303-307.

[139] P. Patsalas, S. Logothetidis, Optical, electronic, and transport properties of nanocrystalline titanium nitride thin films, J. Appl. Phys. 90 (2001) 4725.

[140] M. Zhang, M. Li, K.H. Kim, F. Pan, Structural and mechanical properties of compositionally gradient CrNx coatings prepared by arc ion plating, Appl. Surf. Sci. 255 (2009) 9200-9205.

[141] K. Chang, S. Chung, S. Lai, H. Shih, The electrochemical behavior of thermally oxidized CrN coatings deposited on steel by cathodic arc plasma deposition, Appl. Surf. Sci. 236 (2004) 406-415.

[142] C. Liu, H. Yang, Deposition temperature and thickness effects on the characteristics of dc-sputtered ZrNx films, Mater. Chem. Phys. 86 (2004) 370-374.

[143] P. Carvalho, J.M. Chappé, L. Cunha, S. Lanceros-Méndez, P. Alpuim, F. Vaz, E. Alves, C. Rousselot, J.P. Espinós, A.R. González-Elipe, Influence of the chemical and electronic structure

153

on the electrical behavior of zirconium oxynitride films, J. Appl. Phys. 103 (2008) 104907-104907-15.

[144] J. Barranco, F. Barreras, A. Lozano, M. Maza, Influence of CrN-coating thickness on the corrosion resistance behaviour of aluminium-based bipolar plates, J. Power Sources. 196 (2011) 4283-4289.

[145] L. Wang, D. Northwood, X. Nie, J. Housden, E. Spain, A. Leyland, A. Matthews, Corrosion properties and contact resistance of TiN, TiAlN and CrN coatings in simulated proton exchange membrane fuel cell environments, J. Power Sources. 195 (2010) 3814-3821.

[146] M. Sachtleber, D. Raabe, H. Weiland, Surface roughening and color changes of coated aluminum sheets during plastic straining, J. Mater. Process. Technol. 148 (2004) 68-76.

[147] A. Tekkaya, M. Trompeter, H.-. Pham, On the reduction of the gloss property of organic coated sheet metal after forming, Production Engineering. 4 (2010) 483-489.

[148] O. Wouters, W.P. Vellinga, R. van Tijum, J.T.M. De Hosson, Effects of crystal structure and grain orientation on the roughness of deformed polycrystalline metals, Acta Materialia. 54 (2006) 2813-2821.

[149] X.H. Zhou, X. Su, Effects of deformation mode on surface roughening of austenitic stainless steels, Materials Science and Technology. 27 (2011) 1040-1044.

[150] R.S. Timsit, Electrical contact resistance: properties of stationary interfaces, Components and Packaging Technologies, IEEE Transactions on. 22 (1999) 85-98.

154

[151] L. Krusin-Elbaum, M. Wittmer, Oxidation kinetics of ZrN thin films, Thin Solid Films. 107 (1983) 111-116.

[152] R. Mientus, K. Ellmer, Reactive DC magnetron sputtering of elemental targets in Ar/N2 mixtures: relation between the discharge characteristics and the heat of formation of the corresponding nitrides, Surface and Coatings Technology. 116-119 (1999) 1093-1101.

[153] G. Reiss, J. Vancea, H. Hoffmann, Grain-Boundary Resistance in Polycrystalline Metals, Phys. Rev. Lett. 56 (1986) 2100.

[154] T. Brat, N. Parikh, N.S. Tsai, A.K. Sinha, J. Poole, C. Wickersham, Characterization of titanium nitride films sputter deposited from a high-purity titanium nitride target, Journal of Vacuum Science & Technology B: Microelectronics and Nanometer Structures. 5 (1987) 1741-1747.

[155] J.H. Kang, K.J. Kim, Structural, optical, and electronic properties of cubic TiNx compounds, J. Appl. Phys. 86 (1999) 346-350.

[156] M. Kawamura, Y. Abe, H. Yanagisawa, K. Sasaki, Characterization of TiN films prepared by a conventional magnetron sputtering system: influence of nitrogen flow percentage and electrical properties, Thin Solid Films. 287 (1996) 115-119.

[157] W. Lengauer, Properties of Bulk delta-TiN sub 1--x Prepared by Nitrogen Diffusion Into Titanium Metal, Journal of Alloys and Compounds(Switzerland). 186 (1992) 293-307.

[158] E. Martinez, R. Sanjinés, O. Banakh, F. Lévy, Electrical, optical and mechanical properties of sputtered CrNy and Cr1−xSixN1.02 thin films, Thin Solid Films. 447-448 (2004) 332-336.

155

[159] O. Lavigne, C. Alemany-Dumont, B. Normand, M.H. Berger, C. Duhamel, P. Delichére, The effect of nitrogen on the passivation mechanisms and electronic properties of chromium oxide layers, Corros. Sci. 53 (2011) 2087-2096.

[160] E. Ando, S. Suzuki, Optical and mechanical properties of Cr and CrNx films by dc magnetron sputtering, J. Non Cryst. Solids. 218 (1997) 68-73.

[161] H.M. Benia, M. Guemmaz, G. Schmerber, A. Mosser, J.-. Parlebas, Investigations on non-stoichiometric zirconium nitrides, Appl. Surf. Sci. 200 (2002) 231-238.

[162] D. Gall, Growth of single-crystal CrN on MgO(001): Effects of low-energy ion-irradiation on surface morphological evolution and physical properties, J. Appl. Phys. 91 (2002) 3589.

[163] A. Herwadkar, W.R.L. Lambrecht, Electronic structure of CrN: A borderline Mott insulator, Phys. Rev. B. 79 (2009) 035125.

[164] P.A. Bhobe, A. Chainani, M. Taguchi, T. Takeuchi, R. Eguchi, M. Matsunami, K. Ishizaka, Y. Takata, M. Oura, Y. Senba, H. Ohashi, Y. Nishino, M. Yabashi, K. Tamasaku, T. Ishikawa, K. Takenaka, H. Takagi, S. Shin, Evidence for a Correlated Insulator to Antiferromagnetic Metal Transition in CrN, Phys. Rev. Lett. 104 (2010) 236404.

[165] D. Nam, H. Lee, Thermal nitridation of chromium electroplated AISI316L stainless steel for polymer electrolyte membrane fuel cell bipolar plate, J. Power Sources. 170 (2007) 268-274.

[166] S. Lee, J. Kim, Y. Lee, D. Wee, Effects of low-temperature nitridation on the electrical conductivity and corrosion resistance of 446M stainless steel as bipolar plates for proton exchange membrane fuel cell, Int J Hydrogen Energy. 35 (2010) 725-730.

156

[167] B. Yang, M.P. Brady, H. Wang, J.A. Turner, K.L. More, D.J. Young, P.F. Tortorelli, E.A. Payzant, L.R. Walker, Protective nitride formation on stainless steel alloys for proton exchange membrane fuel cell bipolar plates, J. Power Sources. 174 (2007) 228-236.

[168] R. Tian, Chromium nitride/Cr coated 316L stainless steel as bipolar plate for proton exchange membrane fuel cell, J. Power Sources. 196 (2011) 1258-1263.

[169] B. Wu, Y. Fu, J. Xu, G. Lin, M. Hou, Chromium nitride films on stainless steel as bipolar plate for proton exchange membrane fuel cell, J. Power Sources. 194 (2009) 976-980.

[170] L. Yang, H. Yu, L. Jiang, L. Zhu, X. Jian, Z. Wang, Improved anticorrosion properties and electrical conductivity of 316L stainless steel as bipolar plate for proton exchange membrane fuel cell by lower temperature chromizing treatment, J. Power Sources. 195 (2010) 2810-2814.

[171] C. Bai, M. Ger, M. Wu, Corrosion behaviors and contact resistances of the low-carbon steel bipolar plate with a chromized coating containing carbides and nitrides, Int J Hydrogen Energy. 34 (2009) 6778-6789.

[172] H.Y. Lee, J.W. Choi, G.H. Hwang, S.G. Kang, Performance Degradation of TiN-and TiC-deposited AISI316 bipolar plates for proton exchange membrane fuel cells, Metals and Materials International. 12 (2006) 147-151.

[173] N.D. Nam, J.H. Han, J.G. Kim, P.H. Tai, D.H. Yoon, Electrochemical properties of TiNCrN-coated bipolar plates in polymer electrolyte membrane fuel cell environment, Thin Solid Films. 518 (2010) 6598-6603.

157

[174] D. Zhang, L. Duan, L. Guo, W. Tuan, Corrosion behavior of TiN-coated stainless steel as bipolar plate for proton exchange membrane fuel cell, Int J Hydrogen Energy. 35 (2010) 3721-3726.

[175] S. Auvinen, T. Tingelof, J.K. Ihonen, J. Siivinen, M. Johansson, Cost Effective In-Situ Characterization of Coatings for PEFC Bipolar Plates Demonstrated with PVD Deposited CrN, J. Electrochem. Soc. 158 (2011) B550-B556.

[176] C.Y. Choi, D.G. Nam, Chromium Nitrided A283-C Steel as Bipolar Plate for PEMFC, Advanced Materials Research. 197 (2011) 753-756.

[177] D.-. Han, W.-. Hong, H.S. Choi, J.J. Lee, Inductively coupled plasma nitriding of chromium electroplated AISI 316L stainless steel for PEMFC bipolar plate, Int J Hydrogen Energy. 34 (2009) 2387-2395.

[178] A. Armigliato, G. Celotti, A. Garulli, S. Guerri, P. Ostoja, R. Rosa, G. Martinelli, Characterization of titanium nitride films deposited onto silicon, Thin Solid Films. 92 (1982) 341-346.

[179] N. Kumar, K. Pourrezaei, M. Fissel, T. Begley, B. Lee, E.C. Douglas, Growth and properties of radio frequency reactively sputtered titanium nitride thin films, Journal of Vacuum Science & Technology A: Vacuum, Surfaces, and Films. 5 (1987) 1778-1782.

[180] L.E. Koutsokeras, G. Abadias, C.E. Lekka, G.M. Matenoglou, D.F. Anagnostopoulos, G.A. Evangelakis, P. Patsalas, Conducting transition metal nitride thin films with tailored cell sizes: The case of δ-Ti$_x$Ta$_{1-x}$N, Appl. Phys. Lett. 93 (2008) 011904-3.

[181] Y. Lin, J. Huang, G. Yu, Effect of nitrogen flow rate on properties of nanostructured TiZrN thin films produced by radio frequency magnetron sputtering, Thin Solid Films. 518 (2010) 7308-7311.

[182] W. Lee, Y. Kuo, H. Huang, C. Lee, Effect of density on the diffusion barrier property of TiNx films between Cu and Si, Mater. Chem. Phys. 85 (2004) 444-449.

[183] Y. Massiani, A. Medjahed, P. Gravier, L. Argème, L. Fedrizzi, Electrochemical study of titanium nitride films obtained by reactive sputtering, Thin Solid Films. 191 (1990) 305-316.

[184] B. Navinšek, P. Panjan, A. Cvelbar, Characterization of low temperature CrN and TiN (PVD) hard coatings, Surface and Coatings Technology. 74-75, Part 1 (1995) 155-161.

[185] K.Y. Ahn, M. Wittmer, C.Y. Ting, Investigation of Tin films reactively sputtered using a sputter gun, Thin Solid Films. 107 (1983) 45-54.

[186] D.S. Williams, F.A. Baiocchi, R.C. Beairsto, J.M. Brown, R.V. Knoell, S.P. Murarka, Nitrogen, oxygen, and argon incorporation during reactive sputter deposition of titanium nitride, Journal of Vacuum Science & Technology B: Microelectronics and Nanometer Structures. 5 (1987) 1723-1729.

[187] M. Wittmer, Electrical characteristics of TiN contacts to N silicon, J. Appl. Phys. 52 (1981) 5722.

[188] H.O. Pierson, Handbook of Refractory Carbides and Nitrides, Pg. 187, William Andrew Publishing/Noyes, 1996.

159

[189] T.S. Oyama, The chemistry of transition metal carbides and nitrides, (1996) 534.

[190] K. Schwarz, Band structure and chemical bonding in transition metal carbides and nitrides, Critical Reviews in Solid State and Materials Sciences. 13 (1987) 211-257.

[191] D. Gall, I. Petrov, J. Greene, Epitaxial ScTiN(001): Optical and electronic transport properties, J. Appl. Phys. 89 (2001) 401.

[192] B.W. Karr, D.G. Cahill, I. Petrov, J.E. Greene, Effects of high-flux low-energy ion bombardment on the low-temperature growth morphology of TiN(001) epitaxial layers, Phys. Rev. B. 61 (2000) 16137.

[193] P. Panjan, B. Navinšek, A. Cvelbar, A. Zalar, J. Vlcek, High-temperature oxidation of TiN/CrN multilayers reactively sputtered at low temperatures, Surface and Coatings Technology. 98 (1998) 1497-1502.

[194] P.A. Anderson, R.J. Kinsey, S.M. Durbin, A. Markwitz, V.J. Kennedy, A. Asadov, W. Gao, R.J. Reeves, Magnetic and optical properties of the InCrN system, J. Appl. Phys. 98 (2005) 043903-5.

[195] R. Sanjinés, O. Banakh, C. Rojas, P.E. Schmid, F. Lévy, Electronic properties of Cr1−xAlxN thin films deposited by reactive magnetron sputtering, Thin Solid Films. 420-421 (2002) 312-317.

[196] X.Y. Zhang, J.S. Chawla, B.M. Howe, D. Gall, Variable-range hopping conduction in epitaxial CrN(001), Phys. Rev. B. 83 (2011) 165205.

160

[197] J. Ruan, D. Lii, J.S. Chen, J. Huang, Investigation of substrate bias effects on the reactively sputtered ZrN diffusion barrier films, Ceram. Int. 35 (2009) 1999-2005.

[198] J.-. Huang, C.-. Hsu, S.-. Chen, G.-. Yu, Effect of substrate bias on the structure and properties of ion-plated ZrN on Si and stainless steel substrates, Mater. Chem. Phys. 77 (2003) 14-21.

[199] M.M. Larijani, M. Kiani, M. Tanhayi, A. Majdabadi, Characterization of ion beam sputtered ZrN coatings prepared at different substrate temperatures, Crystal Research and Technology. 46 (2011) 351-356.

[200] D. Dobosz, K. Golaszewska, Z.R. Zytkiewicz, E. Kaminska, A. Piotrowska, T.T. Piotrowski, A. Barcz, R. Jakiela, Properties of ZrN films as substrate masks in liquid phase epitaxial lateral overgrowth of compound semiconductors, Crystal Research and Technology. 40 (2005) 492-497.

[201] H.N. Al-Shareef, X. Chen, D.J. Lichtenwalner, A.I. Kingon, Analysis of the oxidation kinetics and barrier layer properties of ZrN and Pt/Ru thin films for DRAM applications, Thin Solid Films. 280 (1996) 265-270.

[202] E. Reinhold, J. Richter, U. Seyfert, C. Steuer, Metal strip coating by electron beam PVD—industrial requirements and customized solutions, Surface and Coatings Technology. 188-189 (2004) 708-713.

161

[203] E. Bemporad, M. Sebastiani, C. Pecchio, S. De Rossi, High thickness Ti/TiN multilayer thin coatings for wear resistant applications, Surface and Coatings Technology. 201 (2006) 2155-2165.

[204] T. Ganne, J. Crépin, S. Serror, A. Zaoui, Cracking behaviour of PVD tungsten coatings deposited on steel substrates, Acta Materialia. 50 (2002) 4149-4163.

[205] V. Teixeira, Mechanical integrity in PVD coatings due to the presence of residual stresses, Thin Solid Films. 392 (2001) 276-281.

[206] L. Eriksson, E. Harju, A.S. Korhonen, K. Pischow, Formability and corrosion resistance of TiN-coated stainless steel sheet, Surface and Coatings Technology. 53 (1992) 153-160.

[207] E.B. Alaca, M.T.A. Saif, H. Sehitoglu, On the interface debond at the edge of a thin film on a thick substrate, Acta Materialia. 50 (2002) 1197-1209.

[208] J.R. Bautista, F. Avilés, A.I. Oliva, O. Ceh, J.E. Corona, Correlations between mechanical stress, electrical conductivity and nanostructure in Al films on a polymer substrate, Mater Charact. 61 (2010) 325-329.

APPENDIX 1: ASR of formed then coated BPPs.

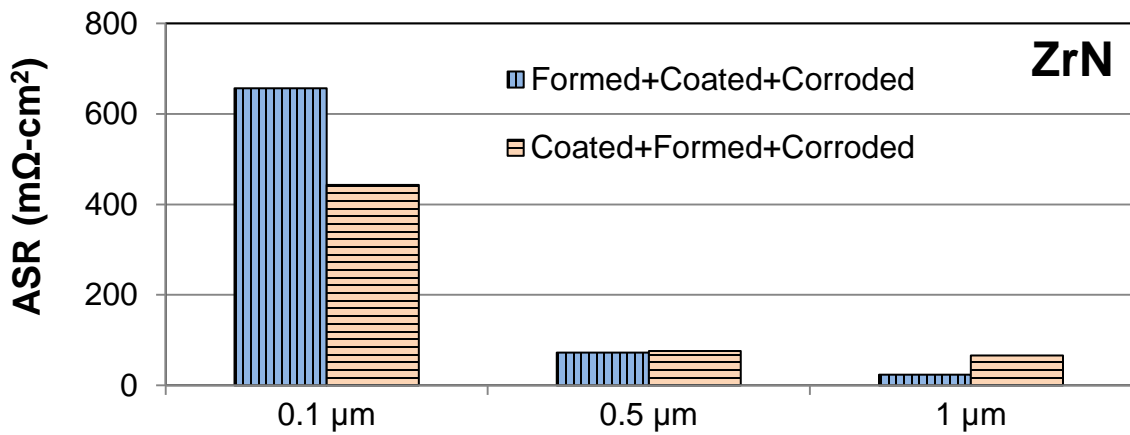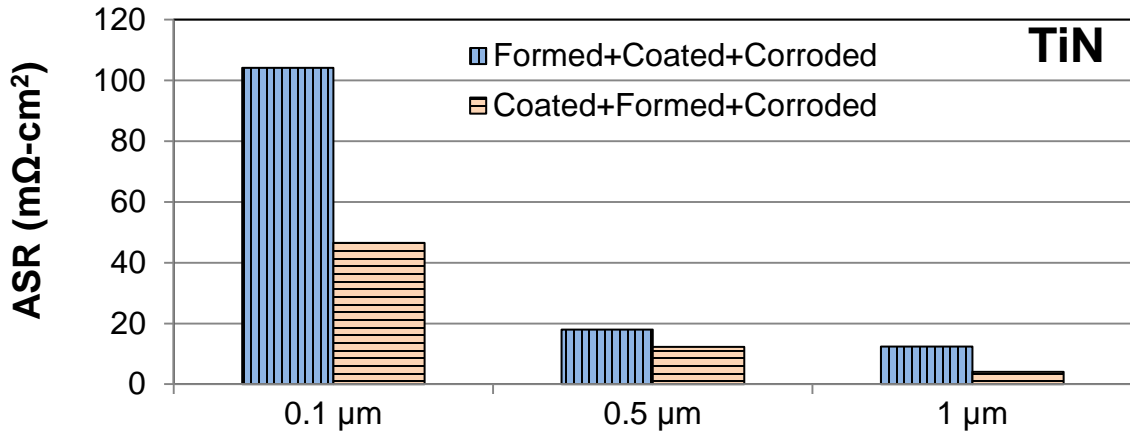| Forming Method	Die Channel Height (μm)	Contact Area (cm^2)	Compaction Pressure (N/cm^2)
Hydroforming	250	7.93	282

Forming Method	Die Channel Height (μm)	Contact Area (cm²)	Compaction Pressure (N/cm²)
Hydroforming	750	7.26	309

Forming Method	Die Channel Height (μm)	Contact Area (cm²)	Compaction Pressure (N/cm²)
Stamping	250	8.8	254

Forming Method	Die Channel Height (µm)	Contact Area (cm²)	Compaction Pressure (N/cm²)
Stamping	750	6.4	350

APPENDIX 2: ASR of BPPs with two different sequences.

Forming Method	Die Channel Height (µm)	Contact Area (cm^2)	Compaction Pressure (N/cm^2)
Hydroforming	250	7.93	282

Forming Method	Die Channel Height (µm)	Contact Area (cm²)	Compaction Pressure (N/cm²)
Hydroforming	750	7.26	309

168

Forming Method	Die Channel Height (µm)	Contact Area (cm^2)	Compaction Pressure (N/cm^2)
Stamping	250	8.8	254

Forming Method	Die Channel Height (μm)	Contact Area (cm^2)	Compaction Pressure (N/cm^2)
Stamping	750	6.4	350

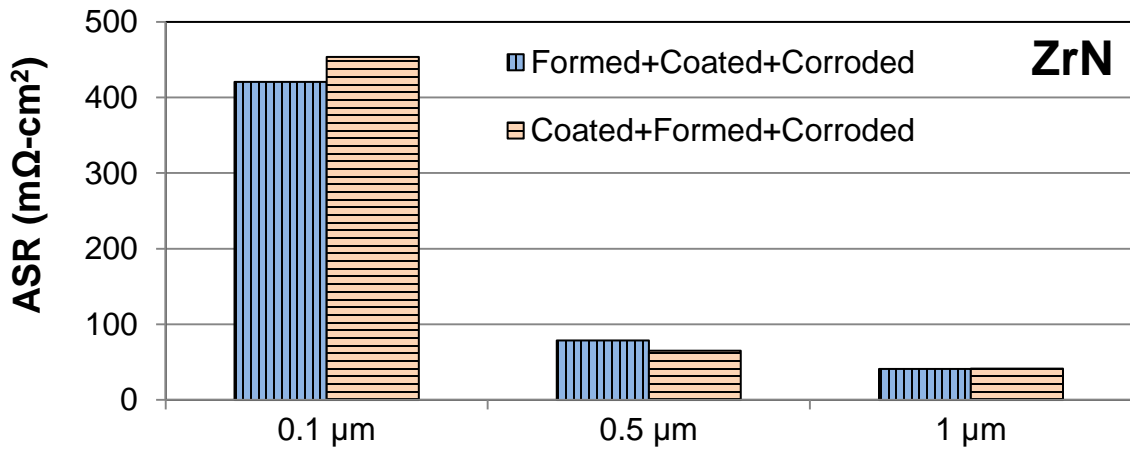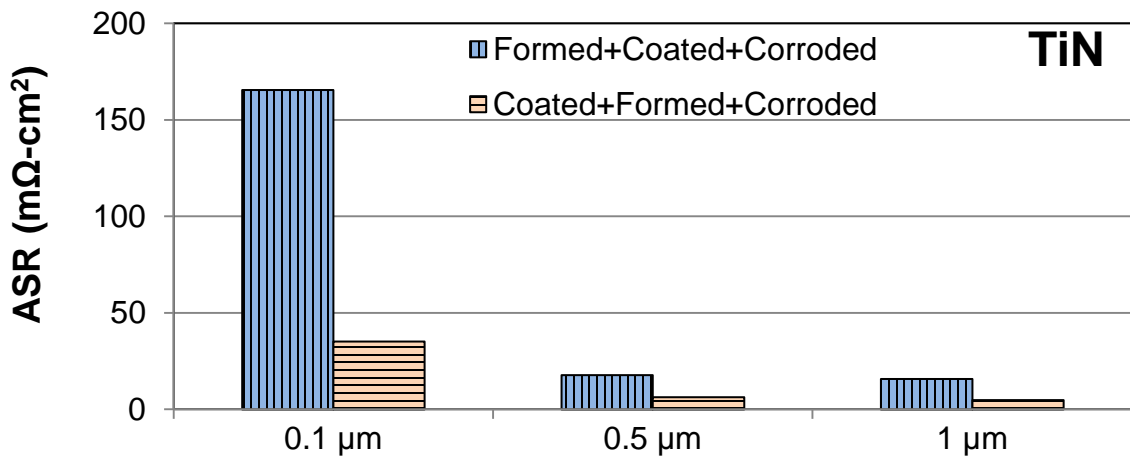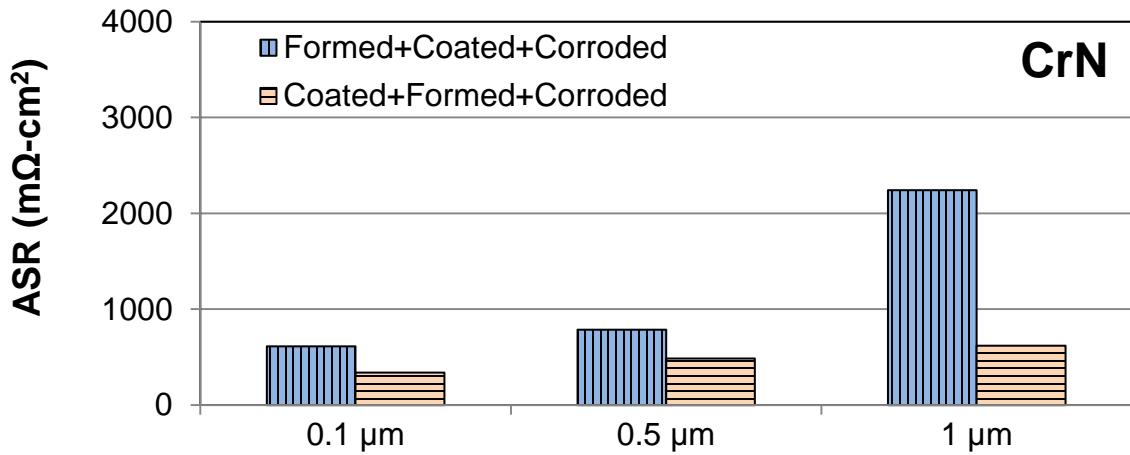# APPENDIX 3: ASR of BPPs with two different sequences after corrosion test.

Forming Method	Die Channel Height (µm)	Contact Area (cm^2)	Compaction Pressure (N/cm^2)
Hydroforming	250	7.93	282

171

Forming Method	Die Channel Height (μm)	Contact Area (cm²)	Compaction Pressure (N/cm²)
Hydroforming	750	7.26	309

Forming Method	Die Channel Height (µm)	Contact Area (cm²)	Compaction Pressure (N/cm²)
Stamping	250	8.8	255

Forming Method	Die Channel Height (μm)	Contact Area (cm²)	Compaction Pressure (N/cm²)
Stamping	750	6.4	350
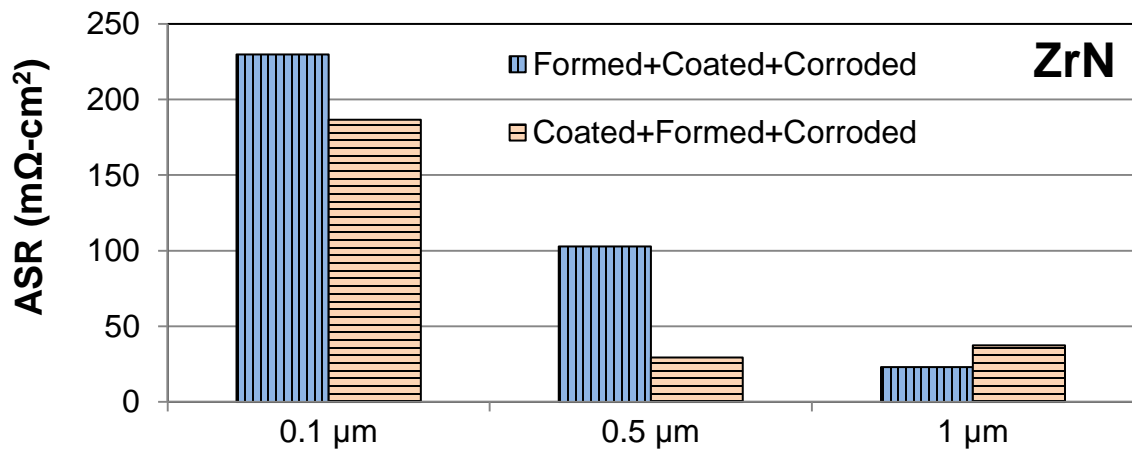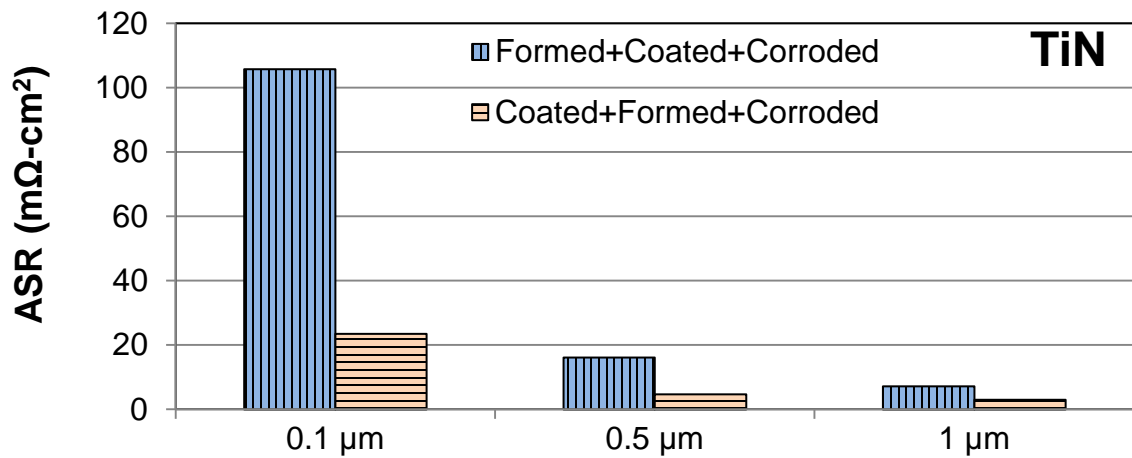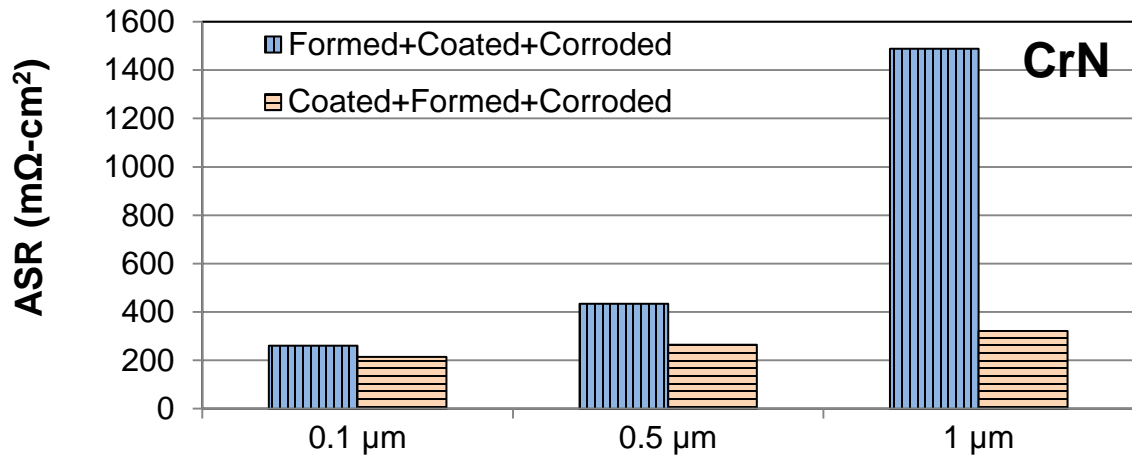
VITA

Name: Cabir Turan

Born: 1974, Sivas, Turkey

Degrees: BSc. in Mechanical Engineering, Istanbul University, Istanbul, Turkey, 1972.

Ph.D. in Mechanical Engineering, VCU, Richmond, USA, 2011.

Experience: Istanbul Gas Distribution Co. Inc. (İGDAŞ), Istanbul, Turkey, since 1996.

PUBLICATIONS

Published Journal Article

Cabir Turan, Ömer Necati Cora, Muammer Koç, "Effect of manufacturing processes on contact resistance characteristics of metallic bipolar plates in PEM fuel cells", International Journal of Hydrogen Energy v36 (2011) pp.12370-12380.

Journal Article under Review

Cabir Turan, Ömer Necati Cora, Muammer Koç, "Contact Resistance Characteristics of Coated Metallic Bipolar Plates for PEM Fuel Cells- Investigations on the Effect of Manufacturing", under review in International Journal of Hydrogen Energy with manuscript number of HE-D-11-03241.

Journal Article to Be Submitted

Cabir Turan, Ömer Necati Cora, Muammer Koç, "Process Sequence Effect on Contact Resistance Characteristics of Coated Metallic Bipolar Plates for PEM Fuel Cells"

Conference Articles

Cabir Turan, Ender Dur, Mevlüt Fatih Peker, Ömer Necati Cora, Muammer Koç, "Corrosion, Contact Resistance, and Surface Characteristics of Stamped And Hydroformed Metallic Bipolar Plates for PEMFC, the ASME 2010 Eighth International Fuel Cell Science, Engineering and Technology Conference FuelCell2010-33347, June 14-16, 2010, Brooklyn, New York, USA.

Ender Dur, **Cabir Turan**, Ömer Necati Cora, Muammer Koç, Experimental Investigations on Corrosion and Contact Resistance Characteristics of Microstamped And Microhydroformed SS316L Bipolar Plates for PEMFC, International Forum on Micro Manufacturing 2010 (IFMM'10), October 20-23, 2010 Gifu, Japan.

Oral Presentation in Conference

Cabir Turan, Ender Dur, Mevlüt Fatih Peker, Ömer Necati Cora, Muammer Koç, "Corrosion, Contact Resistance, and Surface Characteristics of Stamped And Hydroformed Metallic Bipolar Plates for PEMFC, the ASME 2010 Eighth International Fuel Cell Science, Engineering and Technology Conference FuelCell2010-33347, June 14-16, 2010, Brooklyn, New York, USA.

177